UNIVERSITY OF MILANO-BICOCCA

Department of Materials Science

Epitaxy and physical properties of thin films of organic semiconductors

Doctorate School in Materials Science

Thesis

by

Sreejith Embekkat Kaviyil
Matricola 745198

Supervisor: Prof. Alessandro Borghesi

Cycle XXVI
Period 2011 - 2013

Acknowledgments

This work was performed with the support of numerous people I want to acknowledge hereby:

First and foremost, I want to thank my supervisor Prof. Alessandro Borghesi for giving me the opportunity to work under his supervision. I always appreciated his continuous guidance, the helpful discussions as well as the support when things were not working out as expected.

Particular thanks go to Prof. Adele Sassella for guiding me into the world of organic epitaxy and the scientific support throughout the whole time of this work.

I also thank Dr. Marcello Campione and Dr. Luisa Raimondo for all their time and support during these three years.

I also owe a large thank you to Prof. Roberto Lazzaroni, who was my supervisor during my research internship period at University of Mons, Belgium for his great support and encouragement.

A well deserved “thank you!” to Dr. Olivier Douhéret of UMONS for his help and valuable support in the times that I needed it most as well as for all the further support besides the experiments. It was real pleasure being with you Olivier!

My special gratitude goes to my fellow lab mates and friends during these three years, Mohd. Reza Ghaani, Reza.Fathi, Enrico Fugamalli, Silvia Trabattoni, David Moerman, Noham Sebaihi, Ahmadou Ly, Renaud Jonas, Severine Coppée, Pascal Viville, Laurie Letertre, Damien Robert, Charlotte and Eric Khousakoun for the discussions, lab assistance, their support and moreover for the fun time we shared together.

I am also greatly indebted to companionship of a small circle of close friends outside of University who have continuously supported me throughout these years. I thank Jenson and Jickson for many years of true friendship, and for believing in me and encouraging me in this winding road.

Last but not the least, a very special thanks goes to my parents and my lovely wife Nijisha for all the help, support and understanding over the last years, even during times when a normal family life was nearly impossible.

Contents

Chapter 1

1 Introduction

The introduction and flourish of inorganic semiconductor microelectronic industry based on silicon and germanium in the middle of 20th century has changed the world beyond anything that could have been imagined before. However, the growing energy needs of the world are forcing us to think beyond the well established, but expensive inorganic semiconductor industry. Many studies are conducted over the years on various materials in view of substituting inorganic semiconductors. All these studies resulted in the emergence of a new class of materials called 'organic semiconductors' that has the potential to compete with the inorganic electronic industry. A tremendous progress has been made in every aspect of organic electronics in the past two decades. Many new materials are being designed and synthesized, and through the use of these materials many new applications has been conceived and realized. As a result, commercialization of organic devices is now a reality, and the sector is usually termed as plastic electronics. The invention of the first organic photovoltaic (OPV) cell and organic light emitting diode (OLED) by Tang and co-workers from Eastman Kodak, as well as the first organic field-effect-transistors (OFET) by Koezuka and co-workers were the first major leap forward in the growth of organic electronics. Ever since these two inventions, organic materials are finding themselves as active materials in various kinds of electronic, optical and chemical devices like flexible organic light emitting diodes (OLEDs) [1-4], low weight thin film batteries [5, 6], organic photovoltaic cells, bio sensors, thin film super capacitors etc. OLEDs are already deployed in the commercial markets with great success.

Ideally, organic semiconductors are mechanically robust and flexible, light weight, easily processed, and cheap. The possibility to tailor the chemical structure to change the chemical-physical properties is certainly a very attractive and potentially profitable prospect. Owing to the ability to design and synthesize organic materials with desired properties, these materials can be used as active materials in diverse applications in almost all possible streams of science, which is the main motivation for the interest towards these materials.

In organic semiconductors, the carbon p_z orbitals are largely overlapped, resulting in a high delocalization of the π-electrons, forming the so-called π-conjugated system. The π-conjugated materials can be broadly classified into two categories: small molecules (or oligomers) which are usually processed in vacuum by sublimation, and polymers, usually processed by wet chemical techniques. This thesis is mainly focused on small molecules processed in vacuum. For these materials the more controlled environment during the sublimation lead to a greater control over the structure and properties of the deposited layers, while polymer thin films fabricated by solution process show microcrystalline domains embedded in an amorphous matrix. This makes small molecules particularly interesting for the study of fundamental aspects of the material. In this thesis, we mainly discuss our studies on α-quaterthiophene and α-sexithiophene, while a short section is devoted to a solution processed polymer, namely poly (3-hexylthiophene).

The control of molecular orientation in thin solid film phases of organic semiconductors is a basic factor for the exploitation of their physical properties for optoelectronic devices. To improve the solid state properties, highly crystalline organic thin films are necessary, and for the control of the solid state structure organic molecular beam epitaxy (OMBE) represents a suitable choice and is utilized in present work. The aim of the first part of the work described in this thesis has been to gain precise control over the growth of small molecules in the thin film form, by exploiting organic-organic epitaxy with suitable substrates and studying the fundamental properties. In the context of organic epitaxy, the substrate surface quality and its characteristic corrugation, i.e., the surface fluctuations at the atomic/molecular scale are primarily responsible for driving the film orientation [7-9]. In the first part of the thesis, we show how a proper choice of the substrate permits to select not only specific orientations, but also polymorphic and pseudomorphic phases of the overlayer [10-12]. Here we discuss the structural and optical properties of epitaxial thin

films of the organic semiconductor α-quaterthiophene, grown by OMBE on different organic substrates, namely pentaerythritol (PET) single crystals and potassium hydrogen phthalate (KAP) single crystals. With the help of several characterization techniques we were able to show that α-quaterthiophene thin films grown on both substrates are crystalline and, even more important, grow according to a unique epitaxial relationship with the substrate, which in turn leads to a unique crystalline orientation of the film in the growth plane. At room temperature, the KAP single crystal substrate permits to grow crystalline thin films composed by the low temperature polymorph of 4T (4T/LT). On the contrary, the use PET single crystal substrates allow us to successfully grow thin films composed by the high-temperature (4T/HT) polymorph and by a preponderant new pseudomorphic phase with slight structural differences with respect to 4T/HT. Noteworthy, 4T/HT was never observed in thin films, while the usually favored polymorphic phase of 4T is the low temperature one. 4T/HT is predicted to display better transport properties, being therefore more suitable for device applications [13, 14].

The performances of organic devices like OPVs, OLEDs and OFETs have been drastically improved over the years. However, the key constraint for further improving the device performances is charge transport. The mechanism of charge transport is complex, highly dependent on the self organization of the organic material at the nanoscale, π-conjugation, orbital overlap etc. Adding to these constraints the polycrystalline structure deposited organic films generate grain boundaries that affect charge transport. To precisely determine the impact of local nanoscale self-organization of the material electrical properties at the nanoscale, high resolution characterization methods such as conductive atomic force microscopy (C-AFM) can be of great interest. This method enables to correlate a spatial feature on the sample with its local conductivity. As there are many open questions in the working of C-AFM, this part of the thesis focuses on studying the technique itself, as well as the molecule under study. In the second part of the thesis, the material under study are polycrystalline α-sexithiophene thin films deposited on two different substrates (glass and ITO) using OMBE. Various transport mechanisms through the film have been identified and investigated under two different C-AFM configurations to probe

local properties or bulk properties of the material. The effects of different grain packing and grain boundaries on the film electrical response are investigated. Space charge limited current (SCLC) mechanisms and resistive mechanisms are observed depending on the bias polarity and seem to be related to film thickness, injection barrier at the ITO/6T contact, and spreading effect at the nanoscale tip sample contact. The carrier mobility has been extracted in longitudinal direction and vertical direction by modifying Mott-Gurney equation for C-AFM configuration. Finally the results on electrical studies on 6T are compared with polymer P3HT, in order to understand the differences in electrical transport through well organized small molecular thin films and polymers.

Chapter 2 outlines the general overview of the properties of organic semiconductors is presented, along with a general introduction to electrical properties and optical properties of molecular films. An overview to organic epitaxy is also proposed.

Chapter 3 outlines the experimental techniques exploited for the preparation and characterization of the samples studied in this work. An overview of the physical and chemical properties of the materials used in the thesis, of the properties of substrate and on the methods for film growth and characterization techniques is discussed. The growth procedures include organic vapor phase purification, sublimation using OMBE. Atomic force microscopy (AFM) and conductive atomic force microscopy (C-AFM) are used as a tool for characterizing the morphology and electrical properties of the film. A model that explains charge transport mechanisms in organic semiconductors as investigated by scanning probe geometrical configuration is also described in this chapter. Other characterization methods used in this works are specular (θ-2θ) X- ray diffraction scans and polarized optical absorption measurements in transmission mode in the spectral range from 1.5 to 5 eV.

In Chapter 4 the results of the first part of the thesis are presented. Here, the growth as well as the structural/morphological characterization of 4T thin films grown by means of OMBE on KAP single crystals and PET single crystals is discussed. With the help of several characterization techniques it is shown that 4T thin films grown on the (010) surface of KAP single crystals and (001) surface of PET single crystals are crystalline and grow according to a unique epitaxial relationship with the substrate in a peculiar crystalline orientation of the film in the growth plane. Epitaxial relations between the 4T overlayer and the substrates are deduced. It is also shown that,

with the help of suitable substrate, crystalline thin films composed of different polymorphs can be grown by means of organic epitaxy.

Chapter 5 is devoted to the study of local morphological and electrical properties of 6T thin films deposited on different substrates using different C-AFM configurations, which constitutes the second part of this thesis. Here, how the nanoscale orientation of molecules impacts the electrical properties of materials is discussed in detail. The mobility in longitudinal and transversal direction of the film is extracted by employing C-AFM; Along with investigation of the material, charge transport model in different C-AFM configuration is also discussed.

Finally, Chapter 6 outlines a short summary of all the results, together with some of the open perspectives for the prosecution of this work.

1.1 References

1. Tang, C.W. and S.A. VanSlyke, *Organic electroluminescent diodes.* Applied Physics Letters, 1987. **51**(12): p. 913-915.
2. Uoyama, H., et al., *Highly efficient organic light-emitting diodes from delayed fluorescence.* Nature, 2012. **492**(7428): p. 234-238.
3. Wang, Z.B., et al., *Unlocking the full potential of organic light-emitting diodes on flexible plastic.* Nat Photon, 2011. **5**(12): p. 753-757.
4. Li, J., et al., *Highly Efficient Organic Light-Emitting Diode Based on a Hidden Thermally Activated Delayed Fluorescence Channel in a Heptazine Derivative.* Advanced Materials, 2013. **25**(24): p. 3319-3323.
5. Gaikwad, A.M., et al., *A flexible high potential printed battery for powering printed electronics.* Applied Physics Letters, 2013. **102**(23): p. 233302.
6. Kettlgruber, G., et al., *Intrinsically stretchable and rechargeable batteries for self-powered stretchable electronics.* Journal of Materials Chemistry A, 2013. **1**(18): p. 5505-5508.

7. Raimondo, L., et al., *Unique Orientation of Organic Epitaxial Thin Films: The Role of Intermolecular Interactions at the Interface and Surface Symmetry.* The Journal of Physical Chemistry C, 2011. **115**(13): p. 5880-5885.
8. Raimondo, L., et al., *Epitaxial Interfaces in Rubrene Thin Film Heterostructures.* The Journal of Physical Chemistry C, 2013. **117**(27): p. 13981-13988.
9. Moret, M., et al., *Organic-organic heteroepitaxy: facts, concepts and perspectives.* Crystal Research and Technology, 2011. **46**(8): p. 827-832.
10. Sassella, A., et al., *Pseudomorphic growth of organic semiconductor thin films driven by incommensurate epitaxy.* Applied Physics Letters, 2009. **94**(7): p. -.
11. Sassella, A., et al., *Tuning the growth mode in organic molecular-beam epitaxy.* Physical Review B, 2005. **71**(20): p. 201311.
12. Bonafede, S.J. and M.D. Ward, *Selective Nucleation and Growth of an Organic Polymorph by Ledge-Directed Epitaxy on a Molecular Crystal Substrate.* Journal of the American Chemical Society, 1995. **117**(30): p. 7853-7861.
13. Siegrist, T., et al., *Crystal Growth, Structure, and Electronic Band Structure of α-4T Polymorphs.* Advanced Materials, 1998. **10**(5): p. 379-382.
14. Sassella, A., et al., *Probing phase transitions and stability of organic semiconductor single crystals by dielectric investigation.* Journal of Applied Physics, 2011. **109**(1).

Chapter 2

2 Fundamentals

2.1 Introduction to organic semiconductors

In the late 1970s, Shirakawa et al. reported high conductivity in oxidized and iodine-doped polyacetylene [2], demonstrating that polymers could be used as electrically active materials in devices. This resulted in the birth of organic electronics. Since then, tremendous efforts were made to improve the performances of organic semiconductors as active materials in devices. As a result drastic improvements were made in the synthesis and processing of new classes of organic semiconducting materials and have been demonstrated very useful for device applications [3-8]. Even though the performances of organic devices are inferior compared to their inorganic counterparts as of now, the advantages of the former is that they are easily processable, comparatively inexpensive, light weight, in addition, they can be flexible and have chemically tunable opto-electronic properties. Organic light-emitting diodes (OLEDs) have been commercialized already and organic field-effect transistors (OFETs) and organic photovoltaic cells (OPVCs) are expected to get commercialized in the near future.

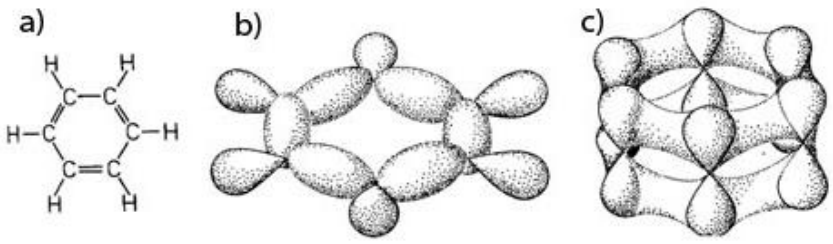

Figure 2-1 (a) Structural formula of a benzene molecule. Schematic representation of (b) σ-orbitals in benzene and (c) π-orbital system with the presence of a delocalized charge density on the entire molecule, with a nodal plane in correspondence of the molecular plane.

Typically, organic semiconductors are π-conjugated systems composed of alternating single and double carbon-carbon bonds. The carbon atom in conjugated molecules is characterized by sp^2 hybridization. When two hybridized carbon atoms come closer, molecular orbitals are formed by

the overlapping of wave function of atomic orbitals of both atoms. These shared orbitals are the so called delta states, formed by *s*, p_x and p_y electrons and the π-orbital, i.e. a π-electron system formed by the overlapping of p_z orbitals of sp^2 hybridized carbon atoms in the molecules, and is above and below the molecular plane. In the π-molecular orbitals, the electrons are delocalized. In Figure 2-1 the structural formula of the simplest model conjugated organic molecule, benzene, is reported. Figure 2-1(b) and (c) presents a schematic of σ molecular orbital and π molecular orbital of the molecule respectively. When compared to overlapping of σ-molecular orbital, that constitutes the backbone of the molecules, π-orbital overlapping is significantly weaker. Since the electrons in π-molecular orbital are weakly bound to the molecule when compared to that in σ-orbitals, the lowest electronic excitations of conjugated molecules are the π–π transitions [9, 10].

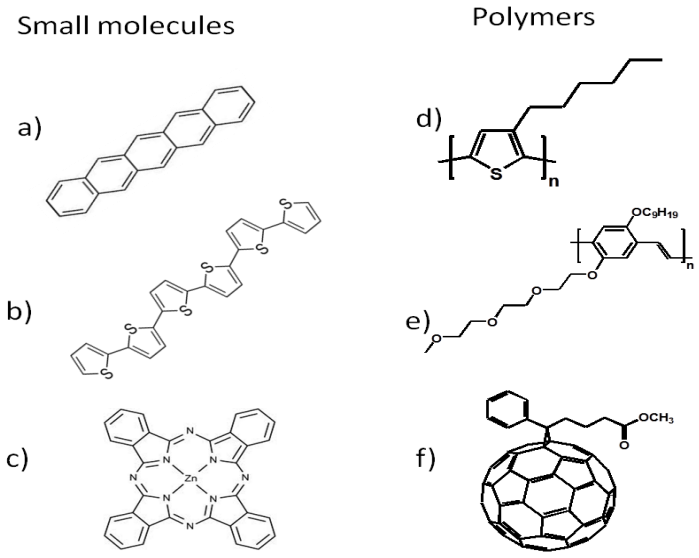

Figure 2-2 Chemical structure of small molecules and polymers: (a) Pentacene (b) sexithiophene (c) Zn-phtalocyanine (d) poly (3-hexylthiophene),(P3HT) (e) Poly[2-methoxy-5-(3′,7′-dimethyloctyloxy)-1,4-phenylenevinylene] (MDMO-PPV) (f) Phenyl-C61-butyric acid methyl ester (PCBM).

It is typical for organic molecules to define the highest occupied molecular orbital (HOMO) level, often considered as the upper limit of the valance band and the lowest unoccupied molecular orbital (LUMO) level as the lower limit of the conduction band of the solid formed by such molecules. As the typical energy band gap between the occupied and empty states (HOMO and LUMO) are typically between 1.5 eV and 3 eV, molecules and the molecular solids absorb and emit light in the visible range. This spectral range makes organic materials very interesting in

terms of devices, like OPVCs and OLEDs. In general, the intrinsic electronic properties of a molecule depends upon the length of the conjugation system or the presence of electron withdrawing or electron donating groups attached to it. This provides a wide range of possibilities to tune the optoelectronic properties of organic material, while the inorganic semiconductors lack such versatility.

Organic semiconductors can be categorized into two main groups: low-molecular weight materials also called small molecules (often they are oligomers, e.g. sexithiophene, pentacene etc) and polymers (P3HT, PCBM etc) [11]. Small molecules are rigid molecules which can be deposited from the gas phase by sublimation, while conjugated polymers can only be processed by solution based techniques, like spin-coating or inkjet printing. Moreover, small molecules can be grown as single crystals by employing different techniques and also as crystalline films, e.g. by organic molecular beam epitaxy, allowing intrinsic electronic properties to be studied on such model systems. Some examples of small molecules and polymers are presented in Figure 2-2. In this thesis two small molecules are introduced, namely α-quaterthiophene and α-sexithiophene along with P3HT, a polymer.

The molecules in organic semiconductors are bonded to each other by means of van der Waals forces, which are significantly weaker intermolecular forces, as compared to covalent bonding typical of inorganic solids. As a result organic crystals have totally different mechanical and thermodynamic properties, such as their reduced hardness and low melting point, to name a few, when compared to inorganic solids. More significantly, such weak intermolecular force leads to a much weaker delocalization of electronic wave functions amongst the nearby molecules. This has direct implications on the opto-electronic properties of the organic semiconductors. This implies, in such materials molecular order plays an important role in electrical properties such as conductivity. That is the reason why organic devices should employ materials where the molecules are designed and packed in the solid for optimum orbital overlap, in order to avoid e.g. the need of very large operating voltages in devices. As the intermolecular bonding is weak, molecules forming molecular crystals retain most of the properties of the single molecule, thus, their optical behavior can be easily adjusted by modifying the molecule chemical structure. In this part of the thesis we will be discussing mainly the physical properties of small molecules.

2.2 Optical properties of organic semiconductors

The optical response of molecular crystals resemble closely to the characteristics of the molecules composing the solid. This happens as a consequence of the weak electronic delocalization within the crystal, leading to only a small perturbation of the electronic orbitals of the molecules when they are packed in the crystal, unlike the case of inorganic solids. Hence, a molecular crystal is sometimes described in the frame of oriented gas model, although there are some differences between the electronic and vibrational spectra of the single molecule and those of the corresponding molecular crystal. First, difference is in molecular crystals the electronic and vibrational spectra are usually shifted towards the lower energies, which is referred as gas-to-crystal shift, as a consequence to the intermolecular force of attraction between the adjacent molecules [12]. Another difference is the existence of Davydov splitting in organic crystals. Here, the resonance interaction between Z translationally inequivalent excited molecules per unit cell leads to a splitting of energy levels into Z states in analogy to Z coupled harmonic oscillators. In case of two molecules per unit cell, as in the case of molecular crystals studied here, this interaction results in an upper and a lower Davydov component [13], with different energy position and also polarization. Furthermore, the interaction between molecules causes the molecular electronic and vibrational states to broaden giving rise to sets of closely spaced states, called excitonic bands. The degeneracy between excited molecular states can be lifted either completely or partially in crystals and selection rules can be violated, when compared to single molecules [14]. This is because in the case of crystals, the selection rules are not only determined by the molecular symmetry, but also by that of the whole crystal.

Davydov developed molecular exciton theory that connects the electronic states of a crystal to those of the constituting molecules, by taking into account the weak van der Waals interactions between the molecules as a weak perturbation [1, 13]. The molecular exciton theory permits to build the eigen-states of a perfect, rigid lattice of $N\sigma$ identical interacting molecules, where N is the total number of unit cells in the crystal and σ the number of molecules per unit cell of that particular crystal. When each molecule is considered as a two level system, with the wave function and energy of the ground and excited states given by $'\phi^0$, e_0, ϕ^* and e^*, respectively the Hamiltonian H of a system of interacting molecules is given by

$$H = \sum_{n\alpha}^{N} H_{n\alpha} + \sum_{n\alpha m\beta}^{'} V_{n\alpha m\beta} \tag{2.1}$$

wherein $H_{n\alpha}$ represents the Hamiltonian of the isolated molecule at the crystal site $n\alpha$, while the second term accounts for the intermolecular interaction, where $V_{n\alpha m\beta}$ accounts for the small perturbation due to van der Waals interaction between molecules $n\alpha$ and $m\beta$. The symbol $\sum'$ indicates it does not contain the term with $n\alpha = m\beta$. The wave function Ψ of the crystal ground state is given by the antisymmetrized product of the ground state wave functions of the single molecules and the corresponding energy at the first order is given by

$$E_0 = Ne_0 + D = Ne_0 + \sum'_{n\alpha m\beta} < \phi^0_{n\alpha}\phi^0_{m\beta} \mid V_{n\alpha m\beta} \mid \phi^0_{n\alpha}\phi^0_{m\beta} > \tag{2.2}$$

Wherein D represents the energy term which accounts for the van der Waals interaction that keep the molecules together in a stabilized manner within the crystal. By considering that, when one molecule is in its excited state, and the excitation being completely shared among all the molecules constituting the crystal, the wave function Ψ^* for the excited state, can be built. Such a collective excited state of the whole crystal is called exciton. In this case, the crystal periodicity has to be taken into account and a wave vector k is introduced, which takes N values in the first Brillouin zone. The corresponding eigen energies, $E(k)$ form the excitonic bands of the crystal and are given by the equation:

$$E(k) = E_0 + e^* - e_0 + \Delta D \pm I(k) \tag{2.3}$$

Here ΔD is the gas-to-crystal shift. It represents the difference between the van der Waals interaction energy D of a single molecule in the ground state with the rest of the molecules in the crystal while D' represents the same, when the same molecule is in its excited state. D and D' are marked in Figure 2-3. $I(k)$ is the exciton shift, which represents the transfer interaction between site $n\alpha$ and the remaining sites of the crystal, and is responsible for the dispersion (i.e. the dependence of E on k) of the exciton band. The equation for solvent shift and exciton shift is given by the following equations.

$$\Delta D = \sum_{m\beta}^{N\sigma'} \{< \phi_{n\alpha}^{*}\phi_{m\beta}^{0} \,|\, V_{n\alpha m\beta} | \phi_{n\alpha}^{*}\phi_{m\beta}^{0} > - < \phi_{n\alpha}^{0}\phi_{m\beta}^{0} | \, V_{n\alpha m\beta} | \phi_{n\alpha}^{0}\phi_{m\beta}^{0} > \quad (2.4)$$

$$I(k) = \sum_{m\beta}^{N\sigma'} \{< \phi_{n\alpha}^{*}\phi_{m\beta}^{0} \,|\, V_{n\alpha m\beta} | \phi_{n\alpha}^{0}\phi_{m\beta}^{*} > exp\,[ik.(r_{n\alpha} - r_{m\beta})]\} \quad (2.5)$$

Where $r_{n\alpha}$ is the position of the molecule in the site α of the n[th] unit cell. From these equations the dielectric behavior of the crystal (*e.g.* the transition probabilities and transition moments between two states, the complete dielectric tensor, the corresponding selection rules, the spectroscopic functions etc.) are detectable under precise experimental conditions, once the ground and excited states of the crystal are known.

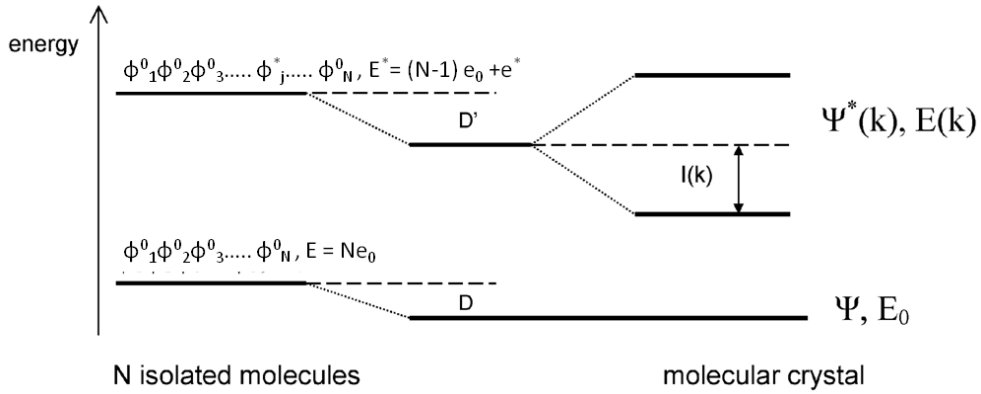

Figure 2-3 Schematic of the electronic energy states of an assembly of N identical non-interacting molecules and of the corresponding molecular crystal. Taken from [1].

2.3 Electrical properties of organic semiconductors

As previously described, the semiconductive properties of organic materials originate from the presence of the delocalized cloud of electrons in the π- molecular orbitals. The parameter that describes charge transport in any material is the mobility μ defined by

$$\mu = E / v \quad (2.6)$$

Wherein v is the speed of the charge and E is the applied electric field. The mobility of charges is a parameter that represents how fast the charge can travel through the material. The mobility in any solids but, in particular, in organic semiconductors is strongly depended on the structural

order. Depending on the degree of molecular order, the transport mechanism in organic materials can be either of two extreme cases: band like transport or transport by charge hopping.

In inorganic semiconductors the atoms are covalently bonded to form rigid structures, where the materials are crystalline, energy levels form where the delocalized carriers can move freely, band with high mobility. A schematic representation of charge transport in bands is presented in Figure 2-4 (a).

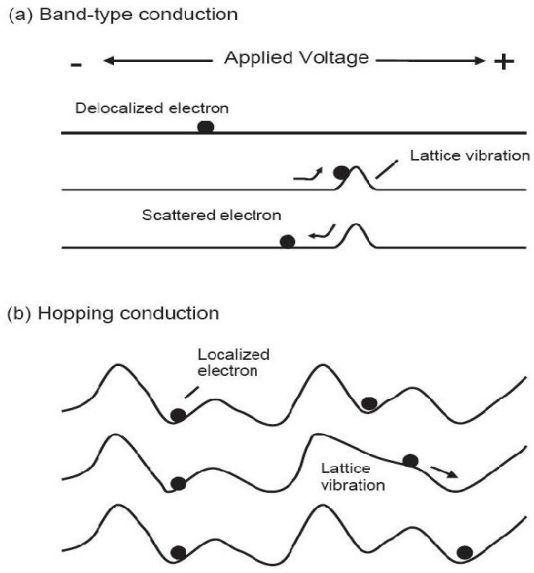

Figure 2-4 Carrier transport mechanisms in materials. (a) Band like conduction. (b) Hopping conduction [15].

In an ideal crystal, depicted as a straight line in Figure 2-4 (a), the delocalized carrier moves as a plane wave without scattering. However in a real crystal the crystal symmetry can be disrupted by lattice vibrations, which scatter the charge carrier and thereby reduce their mobility. With decreasing temperature, the mobility increase [15]. However, in the case of organic semiconductors, due to weak intermolecular forces, instead of a continuous band structure for transport, discrete energy band structure is dominant in the bulk. As a consequence, the freely propagation wave of charge through the energy band, as usually seen in the case of inorganic semiconductor, no longer exists. As a result, charges have to hop through localized states via a phonon assisted hopping process, involving thermionic emission and tunneling of carriers between localized sites (see Figure 2-4 (b)). Here the lattice is irregular and lattice vibrations are

essential for a carrier to move from one site to another. As a result of the high disorder in organic semiconductors, there are no two distinct kinds of transports clearly separated by a band gap just like in the case of inorganic semiconductors like silicon, but instead there are two narrow energy distributions centered on the LUMO and HOMO levels. The shape of the energy distributions (density of states, (DOS)) is assumed to be Gaussian [16].

One of the most accepted hopping models for organic semiconductors was formulated by Bässler and co-workers [16]. Bässler's formalism on organic semiconductor hopping process was based on Miller-Abrahams formalism, was originally used to describe the hopping process among deep traps in inorganic semiconductors [17]. Miller and Abrahams have modeled the transition rate $\nu_{i\to j}$ between an occupied site of energy ε_i and an unoccupied site of energy ε_j separated by a distance *r*.

$$\nu_{i\to j} \quad \alpha \quad exp\left(-2\gamma r_{ij}\right) \begin{cases} exp[-(\varepsilon_j - \varepsilon_i)/k_bT] & \varepsilon_j > \varepsilon_i \\ 1 & \varepsilon_j < \varepsilon_i \end{cases} \tag{2.7}$$

A first factor influencing the transition rate is the tunneling factor $exp\left(-2\gamma r_{ij}\right)$ with γ^{-1} the localization length, the second factor has a Boltzmann form $exp[-\Delta\varepsilon / k_bT]$. Using this expression for the transition rate, Bässler et al. proposed hopping model charge transport in disordered organic semiconductors. His formalism predicts that the mobility in organic semiconductors is proportional to the electric field followed by Poole-Frenkel dependence ($\mu\ \alpha\ exp\ (E/E_0)^{1/2}$). It also implies that the mobility is thermally activated. Furthermore, it has been experimentally proven that the mobility is proportional to the charge carrier concentration *n* in the organic semiconductor. The first injected charges in the organic semiconductor occupy the electronic states in the tail of the Gaussian DOS. When the charge concentration is increased then the charges fill progressively the DOS towards the DOS center where more states are available than in the tail which implies less activation energy is required for hopping. As a result, μ increases with injected charge concentration.

Charge injection and transport

In general, the charge transport models in organic semiconductor device can be classified as either bulk limited or injection limited transport [18, 19]. During the injection of charge carriers from the electrode to the material, the height of barrier at the organic semiconductor metal interface, which controls the carrier injection, plays a pivotal role in determining the nature of transport. The contact between the organic semiconductor and the metal is said to be ohmic, when the barrier for carrier injection at the interface is as small as possible, then the carriers will be injected easily into the material and the transport of charge will be dominated by the bulk. Electrodes in ohmic contact act as an infinite reservoir of charge, which can supply more carriers per unit time than the sample can transport, which can maintain a steady state space charge limited current (SCLC) in the organic device [20-23]. In this case the charges injected will significantly changes the electric field distribution throughout the active layer. As a result, non uniform charge density is found across the active layer and is largest close to the injecting electrode. Space charge limited current (SCLC), when diffusion contributions are neglected can be expressed as

$$J = \frac{9}{8}\pi\varepsilon_0\varepsilon_r\mu\frac{V^2}{L^3} \qquad (2.8)$$

Wherein J is the current density, ε_0 is the permittivity in free space, ε_r is the relative permittivity of the sample, μ is the mobility and L is the thickness of the film. Current voltage characteristics become more complex, when the active material contains traps. In that case, a linear regime where the transport is injection limited is exhibited at first, followed by a steep trap limited transport regime and eventually the V^2 dependent trap-free SCLC regime is reached.

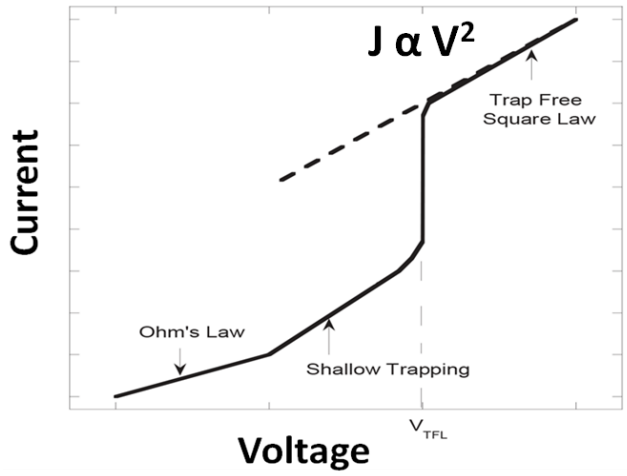

Figure 2-5 Typical SCL current-voltage characteristics in logarithmic scale. Different transport regimes are labeled.

The space charge limited (SCL) I-V characteristics of an organic semiconductor with traps are illustrated in a logarithmic scale in Figure 2-5. At small voltage, Ohm's law dominates the I-V characteristics with the current density proportional to the applied voltage, due to the presence of thermal equilibrium free carriers. With increase of voltage, the SCL current starts to dominate and reaches the shallow trapping field region. With further increase of voltage, the injected electrons fill all the trapping sites in the organic semiconductor. At a particular voltage V_{TFL} all the traps are filled by the injected carriers called the trap-filled-limit (TFL), the current rises very sharply. After the trap-filled-limit, the current-voltage characteristics are characterized by the trap-free square law in equation (2.8).

But, if the injection at the contacts the bottleneck for charge transport, a device is said to be injection or contact limited [24]. The efficiency of injection at the interface between the organic semiconductor and the injecting electrode can be a complex function of many parameters. The interface energetics plays a key role, since the carriers might have to overcome a potential energy barrier to be injected into the active layer. Factors like work function of the injecting electrode, interfacial traps, doping levels, interfacial dipoles etc. influence the interface energetics [25]. Two models are used to describe injection limited mechanisms. The first one is the Richardson-Schottky model for thermionic emission [26], based on the assumption that the electrons/holes can be injected from the metal electrode, once they acquire adequate thermal energy to overcome

the potential barrier at the metal-organic interface. The model is valid at low electric field and at higher temperatures. When the electric field increases, the work function of the metal for thermionic emission decreases, and the Schottky barrier height also decrease.

The second model is the Fowler-Nordheim model [27], which is based on quantum mechanical tunneling injection through the barrier. This type of injection is favorable at very low temperatures or in the cases where the potential barrier height at the interface is relatively large so that the charges can no longer get thermally activated to overcome the barrier and here thermionic emission losses its significance.

2.4 An overview to organic epitaxy

Epitaxy refers to the deposition of a crystalline overlayer with a specific orientation on a crystalline substrate. The orientation is determined by the surface of underlying substrate establishing a specific geometrical relationship between the crystalline lattices of the two materials. The fundamentals of inorganic epitaxy has been well studied and its relevance has been pointed out long before [28, 29].In the case of inorganic epitaxy the important condition is a desirable crystal lattice match between the substrate and the overlayer. As the mismatch gets larger, the over layer film strain to accommodate the lattice structure of the given substrate. So for overlayer films with good crystalline quality, low mismatch value is a necessary parameter and if the mismatch exceeds a critical value, overlayer material will fail to orient epitaxially. The lattice mismatch *f* is given by:

$$f = \frac{|a_f - a_s|}{a_s} \tag{2.9}$$

Where a_f and a_s are the bulk lattice constants along a particular direction of film and substrate, respectively. Moreover, the nature of bonding between the atoms involved in inorganic epitaxy is chemical in nature. Organic-organic epitaxy is ruled by different set of rules, thanks to weak van der Waals force of attraction between the molecules. In the case of organic epitaxy, many instances are reported in the literature which demonstrates that, even when lattice mismatch is of the order of several tens of percent, an orientation effect can be accomplished through a more relaxed epitaxial condition, the so-called coincident epitaxy [30-34]. The interplay between the molecule-molecule and molecule-substrate interactions drives molecular aggregation [35-37]. In

the context of organic epitaxy, the substrate surface quality and its characteristic morphology or, more precisely, its corrugation, i.e., the surface fluctuations at the atomic/molecular scale, is primarily responsible for driving the film orientation. The epitaxial relationships between the substrate and the overlayer can be classified on the basis of geometrical coincidence between lattice or reciprocal lattice points and directions of film and substrate [32]. Line-online is found to be the most common lattice registry observed in the epitaxy of small molecules, i.e. with lattice coincidence only between the non primitive reciprocal lattice points of the substrate and the overlayer.

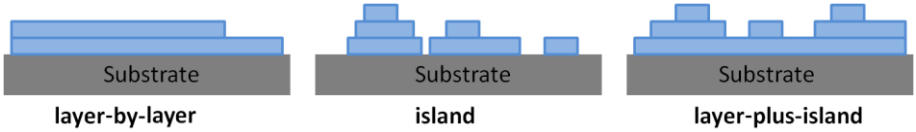

Figure 2-6 Schematic representation of three types of growth modes in OMBE. The substrate is represented by gray color and overlayer by blue color.

Film growth phenomena during organic molecular beam epitaxy (OMBE) is a non equilibrium processes. In Figure 2-6, three typical modes of OMBE growth have been schematically illustrated [1]. The first mode is the Frank-van der Merwe growth mode where the film grows in a layer-by-layer fashion. Here the film growth proceeds by completion of each monolayer before the successive monolayer starts growing. This type of growth is typical when the lattice mismatch between substrate and overlayer is very small. The second one is Volmer-Weber mode which refers to the situation when the film grows by forming 3D islands, which then increase in size until they coalesce. Here, the lattice misfit and the consequent interface strain between substrate surface and the overlayer are high enough such that the second monolayer starts growing on top of first monolayer, before the completion of first monolayer. The third type of growth, which is also the most common one, is Stranski-Krastanov mode, where the film grows in a layer-plus-island fashion. Here the growth is layer-by-layer up to a critical film thickness, after which a transition occurs and islands start growing on top of layers. This type of growth mode refers to those systems where the first few monolayers near to the interface maintain small but significant strain, which is released by the mentioned structural transition, as the film thickness increases.

2.5 References

1. Sassella, A., M. Campione, and A. Borghesi, *Organic epitaxy.* La rivista nuovo cimento, 2008. **31**(8): p. 457 - 490.
2. Shirakawa, H., et al., *Synthesis of electrically conducting organic polymers: halogen derivatives of polyacetylene, (CH).* Journal of the Chemical Society, Chemical Communications, 1977(16): p. 578-580.
3. Sun, Y., et al., *Solution-processed small-molecule solar cells with 6.7% efficiency.* Nat Mater, 2012. **11**(1): p. 44-48.
4. Vandewal, K., et al., *On the origin of the open-circuit voltage of polymer-fullerene solar cells.* Nat Mater, 2009. **8**(11): p. 904-909.
5. Oosterhout, S.D., et al., *The effect of three-dimensional morphology on the efficiency of hybrid polymer solar cells.* Nat Mater, 2009. **8**(10): p. 818-824.
6. Meijer, E.J., et al., *Solution-processed ambipolar organic field-effect transistors and inverters.* Nat Mater, 2003. **2**(10): p. 678-682.
7. Mesta, M., et al., *Molecular-scale simulation of electroluminescence in a multilayer white organic light-emitting diode.* Nat Mater, 2013. **12**(7): p. 652-658.
8. Melzer, C. and H. von Seggern, *Organic electronics: Enlightened organic transistors.* Nat Mater, 2010. **9**(6): p. 470-472.
9. Brutting, W., *Physics of Organic Semiconductors*. 2005, Weinheim: Wiley VCH.
10. Farchioni R., G., G.,, *Organic electronic materials*, 2001, Springer: Heidelberg,.
11. Garnier, F., *Scope and limits of organic-based thin-film transistors,*. Phil. Trans, 1997. **355**: p. 12.
12. Heinemeyer, U., et al., *Exciton-phonon coupling in diindenoperylene thin films.* Physical Review B, 2008. **78**(8): p. 085210.
13. Davydov, A.S., *Theory of molecular excitons*. McGraw-Hill series in advanced chemistry. 1962: McGraw-Hill.
14. Schwoerer, M. and H.C. Wolf, *Organic Semiconductors*, in *Organic Molecular Solids*. 2008, Wiley-VCH Verlag GmbH. p. 217-305.

15. Gutmann, F., Lawrence, E. L., *Organic Semiconductor – Part A.* R.E. Krieger Pub.Co., 1981.
16. Bässler, H., *Charge Transport in Disordered Organic Photoconductors a Monte Carlo Simulation Study.* physica status solidi (b), 1993. **175**(1): p. 15-56.
17. Miller, A. and E. Abrahams, *Impurity Conduction at Low Concentrations.* Physical Review, 1960. **120**(3): p. 745-755.
18. Braun, D., *Electronic injection and conduction processes for polymer devices.* Journal of Polymer Science Part B: Polymer Physics, 2003. **41**(21): p. 2622-2629.
19. Coropceanu, V., et al., *Charge Transport in Organic Semiconductors.* Chemical Reviews, 2007. **107**(4): p. 926-952.
20. Marks, R.N., et al., *Charge injection and transport in poly(p-phenylene vinylene) light emitting diodes.* Synthetic Metals, 1993. **57**(1): p. 4128-4133.
21. Burrows, P.E., et al., *Relationship between electroluminescence and current transport in organic heterojunction light‐emitting devices.* Journal of Applied Physics, 1996. **79**(10): p. 7991-8006.
22. Mark, P. and W. Helfrich, *Space‐Charge‐Limited Currents in Organic Crystals.* Journal of Applied Physics, 1962. **33**(1): p. 205-215.
23. Weisz, S.Z., et al., *Electrode‐Limited and Space‐Charge‐Limited Transient Currents in Insulators.* Journal of Applied Physics, 1968. **39**(5): p. 2296-2302.
24. Arkhipov, V.I., H. Von Seggern, and E.V. Emelianova, *Charge injection versus space-charge-limited current in organic light-emitting diodes.* Applied Physics Letters, 2003. **83**(24): p. 5074-5076.
25. Shen, Y. and G.G. Malliaras, *Charge injection into organic semiconductors.* The Spectrum, 2000. **vol. 13**: pp. 1–4.
26. Chiguvare, Z., J. Parisi, and V. Dyakonov, *Current limiting mechanisms in indium-tin-oxide/poly3-hexylthiophene/aluminum thin film devices.* Journal of Applied Physics, 2003. **94**(4): p. 2440-2448.
27. Forbes, R.G., *On the need for a tunneling pre-factor in Fowler–Nordheim tunneling theory.* Journal of Applied Physics, 2008. **103**(11).

28. M.L., R., Bull. Soc. Fr. Mineral.Cristallogr., 1928. **51**(7).

29. Frank, F.C. and J.H. van der Merwe, *One-Dimensional Dislocations. II. Misfitting Monolayers and Oriented Overgrowth.* Proceedings of the Royal Society of London. Series A. Mathematical and Physical Sciences, 1949. **198**(1053): p. 216-225.

30. Sassella, A., et al., *Epitaxial growth of organic heterostructures: Morphology, structure, and growth mode.* Surface Science, 2007. **601**(13): p. 2571-2575.

31. Mannsfeld, S.C.B. and T. Fritz, *Understanding organic–inorganic heteroepitaxial growth of molecules on crystalline substrates: Experiment and theory.* Physical Review B, 2005. **71**(23): p. 235405.

32. Hooks, D.E., T. Fritz, and M.D. Ward, *Epitaxy and Molecular Organization on Solid Substrates.* Advanced Materials, 2001. **13**(4): p. 227-241.

33. Raimondo, L., et al., *Epitaxial Interfaces in Rubrene Thin Film Heterostructures.* The Journal of Physical Chemistry C, 2013. **117**(27): p. 13981-13988.

34. Campione, M., et al., *Organic–Organic Epitaxy of Incommensurate Systems: Quaterthiophene on Potassium Hydrogen Phthalate Single Crystals.* Journal of the American Chemical Society, 2006. **128**(41): p. 13378-13387.

35. Raimondo, L., et al., *Unique Orientation of Organic Epitaxial Thin Films: The Role of Intermolecular Interactions at the Interface and Surface Symmetry.* The Journal of Physical Chemistry C, 2011. **115**(13): p. 5880-5885.

36. Sassella, A., et al., *Pseudomorphic growth of organic semiconductor thin films driven by incommensurate epitaxy.* Applied Physics Letters, 2009. **94**(7).

37. Campione, M., et al., *Homoepitaxial Growth of α-Hexathiophene.* The Journal of Physical Chemistry C, 2007. **111**(34): p. 12741-12746.

Chapter 3

3 Experiments and methodology

In this chapter, we describe in detail the thin film growth process. This part is then followed by the introduction to some major characterization techniques, like atomic force microscopy, conductive atomic force microscopy, X-ray diffraction and optical spectroscopy, that were employed in the present work. A model that describes the charge transport mechanisms in organic semiconductors with scanning probe geometrical configuration is also introduced. Finally, the organic materials that we worked on are also presented.

3.1 Thin film growth

Organic molecular beam epitaxy (OMBE), a technique based on molecular beam epitaxy [1, 2], is employed to grow high quality crystalline thin films in present work. This technique involves a slow and controlled deposition of sublimated molecules on to a substrate of interest, in an ultra high vacuum atmosphere (~10^{-9} - 10^{-10} Torr); it has the advantage of providing precise control over the thickness of the film deposited, down to a fraction of a single layer. The used technique also provides high control over various growth parameters such as deposition rate, thickness, source temperature and substrate temperature. In addition, the technique provides an atomically clean environment and substrate. In general, it provides altogether a new prospect for understanding many of the fundamental structural, optical and electronic properties of ultrathin organic film systems [2].

In Figure 3-1 a picture of OMBE apparatus is presented with its most important parts labeled. The deposition chamber is maintained in ultra high vacuum condition with the help of three different vacuum pumps operating in successive steps. At first a 20 m^3/h rotary pump is operated to achieve a pressure of 10^{-3} Torr, followed by a 500 ls^{-1} turbomolecular pump which takes the pressure inside the chamber to 10^{-6} Torr and finally a 1500 ls^{-1} cryopump is operated to achieve the maximum vacuum capacity of 10^{-9} Torr inside the deposition chamber (see Figure 3-1) .

Clean substrates are inserted into the system through an introduction chamber, transferred to the deposition chamber through a transfer chamber. The introduction and transfer chambers are separated from each other by means of gate valves.

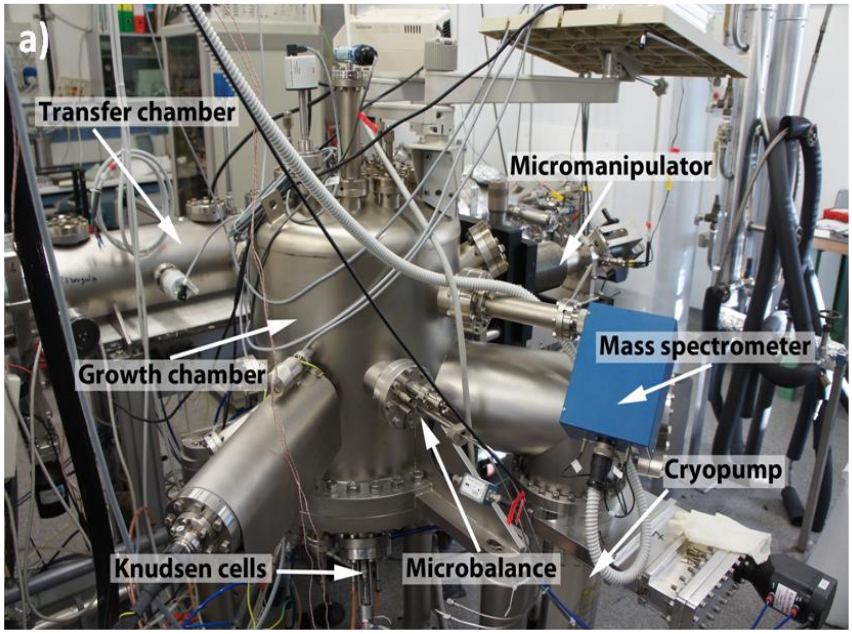

Figure 3-1 Photograph of OMBE apparatus. Main parts of the apparatus, the Knudsen cells, microbalance, mass spectrometer, micromanipulator, transfer chamber, growth/deposition chamber are labeled.

These two chambers help the deposition chamber to stay in high vacuum condition, even while the substrate is introduced or samples are taken out of the deposition chamber. The deposition chamber can host six different sources, all situated at the same distance from the surface of the sample (16 cm in this work). The sample is placed in such a way that its surface faces at the sources. The sources consist of a temperature controlled oven or Knudsen cell. The temperature of the Knudsen cell is controlled by a filament heating system. The shutter that connects the Knudsen cells to the main chamber is opened only after the sublimation temperature of the material is reached. This helps to evaporate out the contaminants (if at all any) with lower sublimation temperature on to the shutter wall, preventing them to reach the sample. Once the shutter is open, the molecular beam is directed towards the sample surface.

With the help of a quartz microbalance, the nominal thickness of the film and the rate of deposition are monitored. With the help of an AC signal the quartz crystal oscillates. Starting from the assumption that addition of material to the quartz surface induces same effect as the addition of same mass of quartz, then the following equation can be used to relate the change in the period of oscillation of the crystal with the thickness of the film [4].

$$T = N_q d_q(\tau - \tau_q)/d_f \qquad (3.1)$$

Wherein, T is the thickness of the film, N_q is a frequency constant, d_q is the quartz density, d_f is the film density, τ_q is the oscillation period of the uncoated crystal and τ is the oscillation period of the loaded crystal. The substrate temperature can be controlled with the help of a heating and cooling mechanism while the quartz microbalance is kept at constant temperature by means of a water cooling system. OMBE also provides the opportunity to measure in situ real time optical characterization of the film by means of reflectance anisotropy spectroscopy (RAS) system and RHEED system [5].

3.2 Overview to scanning probe microscopy

Introduction

One of the most important discoveries of 1980's in the field of material science is the development of a new technique for studying surface structure of a material called Scanning Tunneling Microscopy (STM). Following this invention, a whole family of related techniques was developed. These techniques are now classified in the general category of scanning probe microscopy (SPM). The common feature of all SPM techniques is the usage of a very sharp probe, which is used to scan across the surface of interest. The interactions between the probe and the surface while scanning, is being used to produce a very high resolution digital image of the sample surface. The resolution of the image can be potentially of the order of sub nanometer scale, depending upon the technique and sharpness of the probe tip. Among these techniques, the most important one is atomic force microscopy (AFM), invented in 1986, a versatile instrument which presents a wide range of different operating modes [6, 7] and applications.

3.2.1 AFM

AFM was created to overcome the limitations of the STM, which could image only electrically conductive samples in vacuum. The AFM is designed in such a way that it can be used to probe non conducting samples as well as conductive samples, with or without vacuum. This makes the AFM a particularly useful instrument for the study of organic samples, which are often insulating or poorly conducting [8-11]. As AFM can be used in liquid environments, it has great advantages in the field of biology, as most of the biological samples need to be kept in an aqueous environment [12].

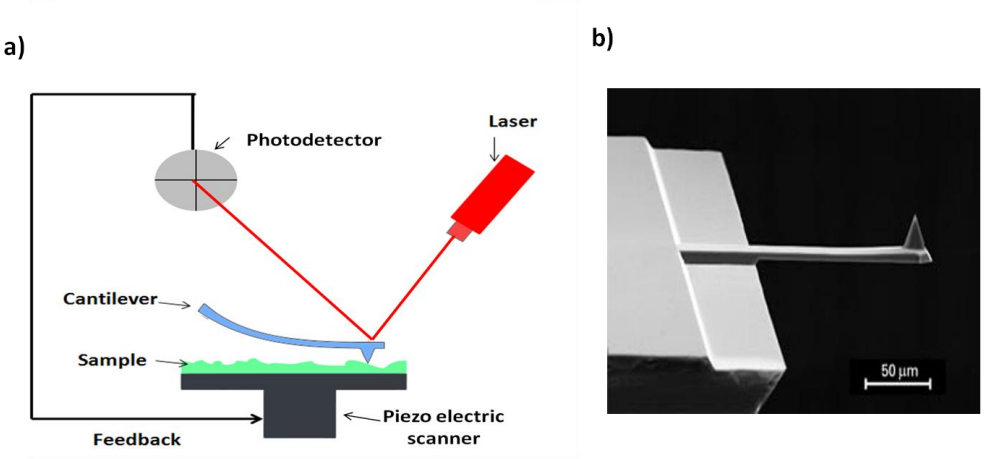

Figure 3-2 (a) Schematic representation of a typical AFM with all its fundamental components. (b) SEM image of a rectangular cantilever with tip mounted on it.

The schematic of basic set-up of a typical AFM is presented in Figure 3-2. AFM contains a flexible cantilever with length of 100 – 400 µm, which is free to bend in vertical and lateral (twist in lateral direction) direction. The free end of cantilever contains a tip, made of silicon or silicon nitride is used for probing the samples (Figure 3-2(b)). Generally the tips are in the form of a square-based pyramid or a cylindrical cone with a curvature radius at the apex generally of the order of tens of nm and a height of the order of tens of microns. The cantilever will deflect or bend at the close proximity of the sample because of the forces between the tip and the sample

surface. A laser beam is directed on the reflective back side of the cantilever which will be reflected on to a photo detector (divided in to four quadrants). Any deflection of the cantilever will create a change in the position of the laser spot on the photodetector, and will be recorded. From the recorded deflection, which is proportional to the tip sample interactions, a digital map of surface topography is generated by the computer. The probe is brought into and out of contact with the sample surface by the help of a piezoelectric scanner, whose motion in the three dimensions can be controlled with nanometric precision by varying the applied bias. A feedback circuit system is also integrated to the system, which will readjust the scanner vertical extension in function of the cantilever deflection, helps to achieve precise control over probing.

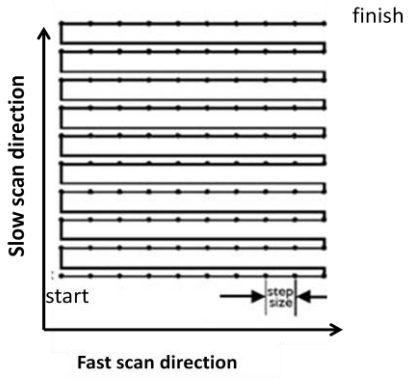

Figure 3-3 Schematic illustration of the scanning process of an AFM. The AFM images constitute of an assembly of the points collected during the scanning in the fast-scan direction.

The scanning process in AFM is illustrated in Figure 3-3. The tip probes along a row in forward and then in the reverse direction (horizontal scanning along the fast scan axis) and then passes to the next line (frame scanning along the slow scan axis). The angle between the fast-scan direction and the long axis of the cantilever can be changed according to the required experimental condition.

The scanner and the dimensions of the tip limit the resolution of AFM. The vertical resolution of AFM is dependent on the precision of vertical movements of the scanner. With the scanner used in present work, the best attainable vertical resolution is approximately 1Å. The lateral resolution is dependent on the tip size and curvature. Considering a tip sample contact radius of the order of less than 10 nm in present work, the lateral resolution is approximately of the same order.

AFM imaging modes:

In general, the forces that contribute to the deflection of an AFM cantilever have contributions from a wide range of different forces like van der Waals force, electrostatic force, chemical force, capillary force and repulsive force. However, the most dominant force associated with AFM is the van der Waals force [7]. To get better insight about the way AFM modes work, it is essential to use so-called force–distance curves. A schematic representation of the force regimes under which different imaging modes occur is presented in Figure 3-4. Here the interaction forces versus the tip sample distance is plotted, with probe-sample distance increasing to the right side of the plot.

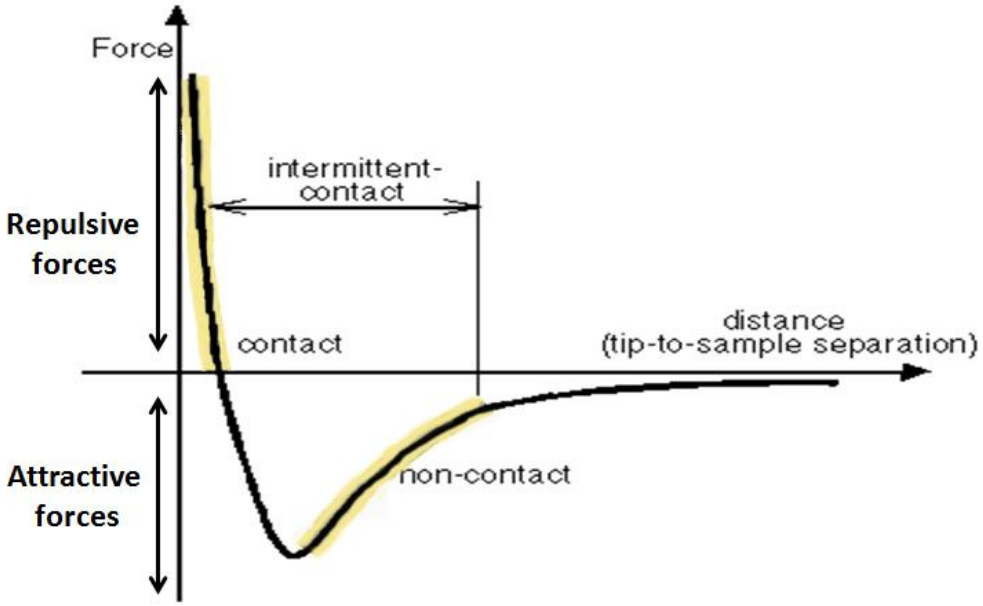

Figure 3-4 Diagram illustrating the tip-sample interaction potential as a function of the tip-sample distance. The force regimes under which each of the three most common AFM imaging modes operate are indicated.

The net forces acting between the probe and the sample surface at large probe sample separation is practically zero. As the probe come close to the sample surface, attractive van der Waals interactions make the probe being towards the surface. Once contact is made, the net interaction becomes repulsive as in this regime a very strong repulsion will be generated either by coulombs

force or Pauli's exclusion principle. Based on the mentioned force regimes the imaging modes in AFM can be broadly classified in to three. They are contact mode, non-contact mode and intermittent contact mode imaging. Depending upon the nature of information required from the sample surface being examined, one among the three modes can be employed.

In contact-AFM mode, the probe sample interaction is in repulsive regime, where the AFM tip makes physical contact with the sample surface (see Figure 3-4). As the scanner traces the tip across the sample, the contact force between the tip-sample causes the cantilever to bend to accommodate the ups and down in the sample topography. Contact AFM can be employed in two different modes. In constant force mode, a feedback mechanism is employed to keep the cantilever deflection a constant. As the cantilever is deflected, a feedback circuit alters the *z*-height according to the topography of the sample, to cause the cantilever to return to the original deflection or set point. The variation in the *z*-position is recorded and this information as a function of the *x*, *y* position is used to create the corresponding topographical image. In variable force imaging, the average distance between the probe and the sample is fixed while scanning and the spatial variation of the cantilever deflection is used directly to create the topographic image of the sample surface. Contact mode AFM is often used for probing hard and relatively flat sample.

In non-contact mode imaging, the cantilever oscillates either in its resonant frequency or just above where the amplitude of oscillation is typically a few nanometers (<10 nm), near the surface of the sample [13]. When the probe come close to the sample surface (1-10 nm above the surface), long-range attractive forces such as van der Waals and electrostatic forces dominates between atoms in the probe and the sample. This leads to a shift in the frequency of oscillation of the cantilever. With the help of feedback loop system, the shift in frequency is detected and the *z*-positioning of the cantilever is adjusted in such a way that a constant oscillation amplitude or frequency is maintained.

Non-contact mode AFM (NC-AFM) does not suffer from tip or sample degradation effects makes it preferable for measuring soft samples, e.g., biology sample and organic thin film. However, performing NC-AFM in air is not preferable as the presence of water layer over the sample surface can make topography for the sample look different.

Intermittent-contact or tapping mode atomic force microscopy(TM- AFM) is similar to NC-AFM, except that for TM-AFM the vibrating cantilever tip is brought closer to the sample surface and the probe will repeatedly engage and disengage with the sample surface, restricting the amplitude of oscillation. While scanning the sample, the oscillatory amplitude of the cantilever will change according to differing topography. With the help of feedback mechanism the *z*-height between the sample and the probe is altered to maintain constant amplitude, an image of the surface topography is digitally constructed in a similar manner as with non-contact mode imaging. The TM-AFM operating region is indicated on the force distance plot in Figure 3-4. TM-AFM is a compromise between contact and non contact AFM as it is unlikely to damage the sample like contact AFM because it eliminates lateral forces (friction or drag) between the tip and the sample. It is also more effective in imaging larger scan sizes that may include greater variation in sample, when compared to NC-AFM.

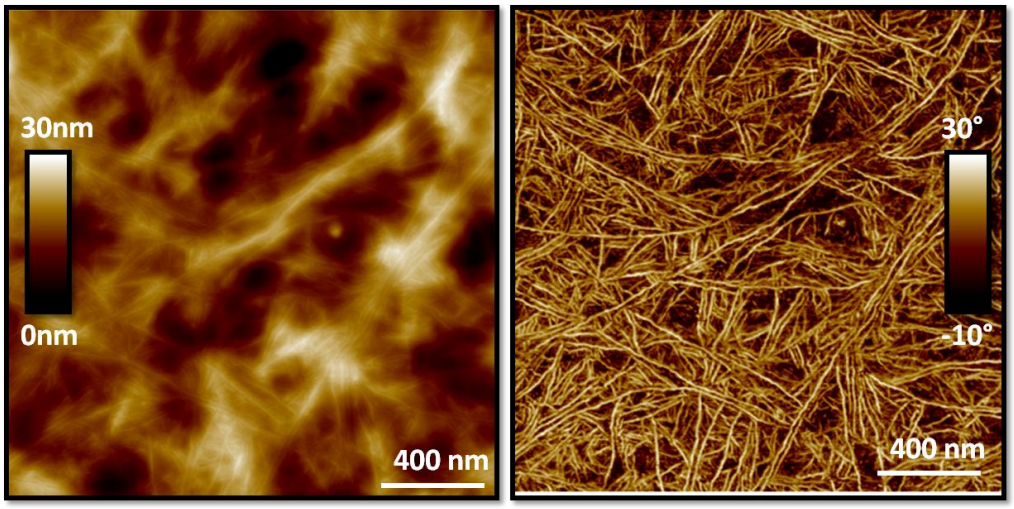

Figure 3-5 (a) Height image of fibrillar P3HT deposited on glass substrate. (b) Phase image of (a). The fibrillar morphology of the film is not very evident from the height image, while the phase image provides superior image detail and higher resolution.

While scanning the sample surface in tapping mode, it is also possible to collect phase-contrast images, in addition to height images. Phase imaging is an extension of TM-AFM that provides nanometer scale information about the surface structure and properties of the sample surface that is not often revealed by the height image. In this mode of imaging, the phase shift of the

oscillating cantilever relative to the driving signal is measured. This phase shift is directly related with specific material properties that effect the tip/sample interaction. As a result phase imaging detects variations in adhesion, composition, friction and viscoelasticity and makes it very useful in identification of contaminants, mapping of different components in composite materials etc. In Figure 3-5, the height and phase image of thin film of P3HT polymer with fibrillar morphology is presented. The fibrils are not very evident from the height image, while the phase image provides superior image detail and higher resolution.

3.2.2 Conductive AFM

Conductive AFM is a current sensing technique based on contact mode AFM, for the electrical characterization of semiconducting and low-conducting samples. C-AFM consists of a metal coated AFM tip, which will act as one of the electrode. The technique allows user to measure the current flowing through the metal coated probe of the microscope and the semiconducting / conducting sample upon dc bias, simultaneously providing two dimensional mapping of the topography and electrical properties. Current sensitivity of commercially available modules yields few hundreds of femto-ampere [14, 15]. The electrical characterization of soft materials such as organic semiconductors is possible with this technique without causing any sample damage, by using soft cantilever. A schematic representation of C-AFM is presented in Figure 3-6

The C-AFM can be operated in the imaging mode and spectroscopic mode. In imaging mode, it is possible to collect two-dimensional conductivity images by performing a scan at a fixed bias and measuring the current for each scanning point, while simultaneously collecting topographical images. In spectroscopic mode, the tip is fixed in a point of the sample and current is measured, while the voltage bias is ramped to get local current-voltage (I-V) curves. Such I-V profiles can be employed to locally study the charge transport mechanisms and to extract the charge carrier mobilities [14, 16]

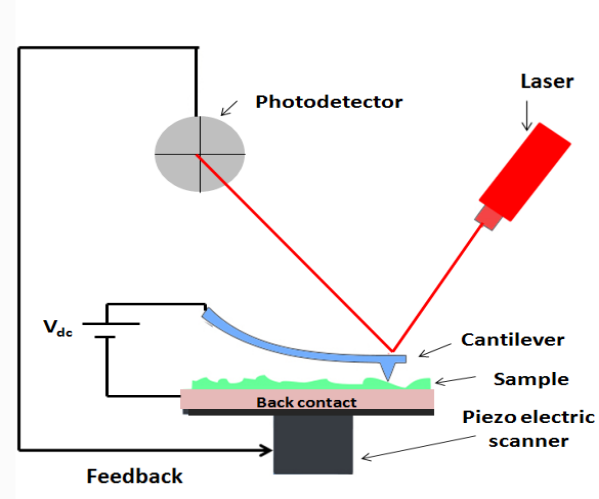

Figure 3-6 A schematic representation of C-AFM set up.

The C-AFM measurements are performed in two different configurations, side configuration and vertical configuration [17]. In both configurations, the C-AFM tip acts as the anode. A schematic display of these two configurations is presented in Figure 3-7 (a and b) and (c and d) for side configuration and vertical configuration, respectively for different bias polarity. In the side configuration, organic sample is deposited on an insulating surface like glass with a patterned back electrode (cathode) at one side of the substrate. Here the tip scans the thin film surface over the substrate with the cathode located microns aside.

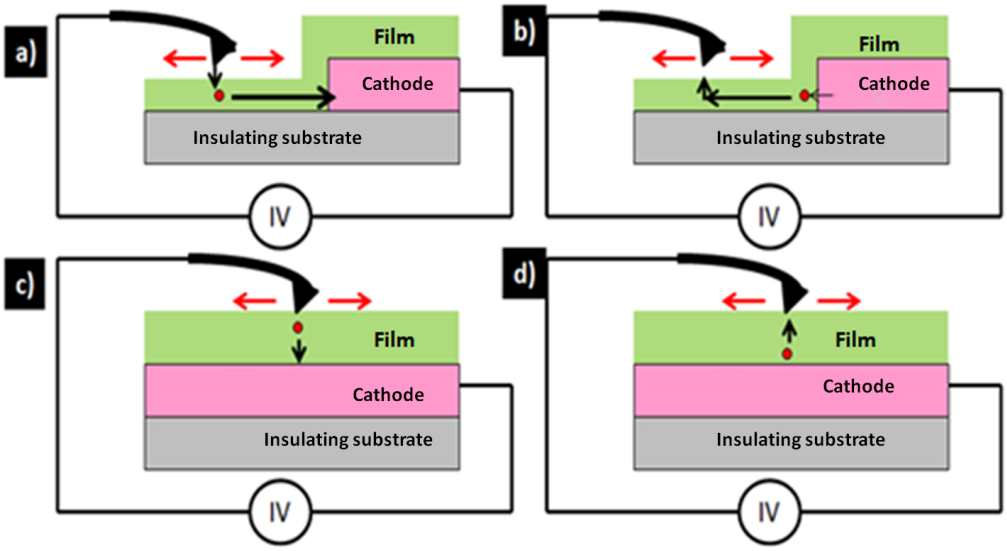

Figure 3-7 (a) Side configuration with negative sample dc bias. Holes are injected from C-AFM tip and travel laterally through the film to cathode. (b) Side configuration with positive sample dc bias. Holes are injected from cathode and travel laterally through the film to tip. (c) Vertical configuration with negative sample dc bias. Holes are injected from tip and travel vertically to cathode through the organic thin film. (d) Vertical configuration with positive sample dc bias. Holes are injected from cathode, travel vertically to the tip through the film.

The probability of perturbation of the measurement emerging from the direct contact between the C-AFM tip with the cathode while probing on the film is avoided this way. Here, the carriers injected have to travel in lateral direction a distance of few hundreds of microns to reach the cathode. In the vertical configuration, the film is deposited directly on a conducting substrate. The injected carriers travel vertically through the thickness of film, which is of the order of few tens of nanometer.

AFM components used for this work

The AFM used for present work is a Veeco Nanoscope Multimode V, equipped with tapping mode and C-AFM extension modules. It is equipped with two different piezoelectric scanners: a J scanner, with maximum scanning area of 140 ×140 μm^2 and an E scanner, with maximum scanning area of 14 × 14 μm^2. In the case of tapping mode AFM, PPP-NCHR manufactured

silicon probes from Nanosensors with a curvature radius less than 10 nm and a cantilever spring constant of ~40 Nm^{-1} have been employed while PPP-contPt coated platinum iridium 5 ($PtIr_5$) tips have been employed in the case of C-AFM. The conductive probes present a curvature radius of about 20 nm and spring constant of ~0.1 Nm^{-1}. The Images were collected with the maximum available number of pixels in each direction (512 or 1024). The collected images have been corrected and analyzed with the Nanoscope software version 7.30.

3.2.3 Charge transport mechanisms in organic semiconductors with scanning probe geometrical configuration.

Schottky diode model is used to explain the behavior of inorganic diodes. However in organic semiconductors, in general, the free carrier density is extremely low compared to inorganic semiconductor. As a result, depletion region in organic thin films is often larger than the thickness of the film (the depletion region extends over a small part of the whole thickness of the inorganic semiconductor). Because of this reason, the working principle of organic diodes is better described by metal-insulator-metal (M-I-M) model than the Schottky diode model [3]. The energy level alignment of the p-type organic diode is

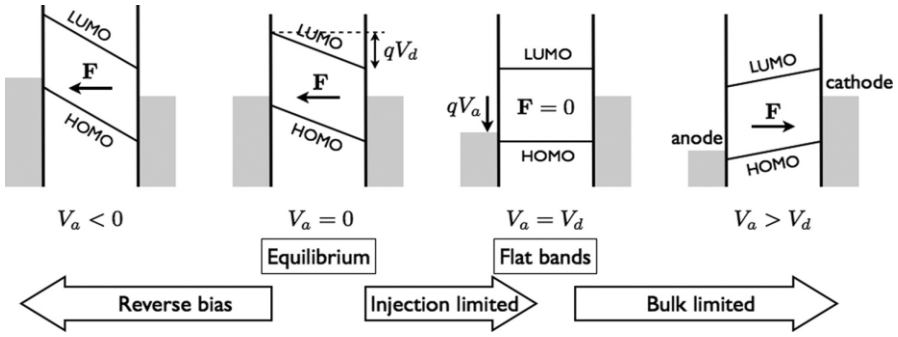

Figure 3-8 Energy diagram of an organic diode described using MIM model [3].

described by M-I-M model is shown in the Figure 3-8. The M-I-M device is characterized by a diffusion potential V_d (built in potential) that corresponds to the difference between work function of anode and cathode. It is worth pointing out that the V_d depends only on the electrodes but not the active organic material. When the electrodes are electrically connected to the active material,

and no voltage is applied, the built in potential induces a bend in the energy level in such a way that, it prevents the hole injection at the anode (the equilibrium condition). If the applied potential applied to the anode (V_a) becomes exactly equal to the diffusion potential, flat band condition is reached and if V_a exceeds V_d ,favorable band bending will happen for the injection of holes from the anode and bulk limited current start flowing through the organic diode.

Organic diode configuration is discussed here using C-AFM tip as one of the electrode. Unlike other macroscopic devices that monitor the charge transport through the sample, C-AFM is operated with asymmetrical electrodes. The influence of geometrical asymmetry of electrodes has to be taken care of, while studying organic semiconducting materials using C-AFM.

Generally in single carrier π- conjugated devices, the analysis of charge carrier transport is based on space-charge-limited current measurements [18-21]. In these measurements usually the devices consist of two planar contacts that efficiently inject either holes or electrons. In trap free space charge limited regime, the current density is described by Mott-Gurney law (see equation (2.8)). However, because of the geometrical asymmetry of electrodes in C-AFM measurements, whether to use Mott-Gurney law in its pure form is still an open question, as many groups have reported discrepancies between the mobility value extracted from point probe configuration in C-AFM and macroscopic measurements [22-24]. Typically the planar electrode law directly applied to C-AFM measurements leads to over estimation of current density. A schematic diagram showing current flow in planar devices and C-AFM configuration is presented in Figure 3-9.

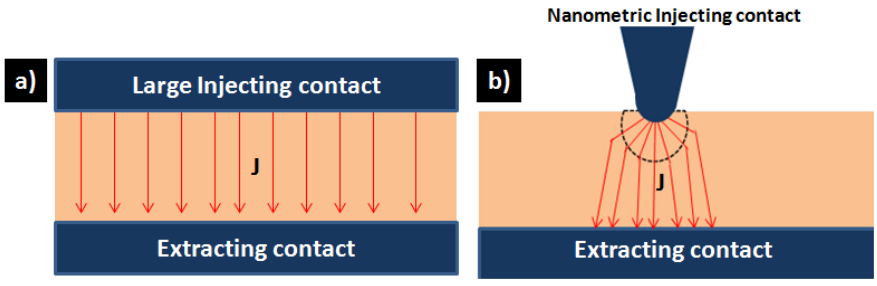

Figure 3-9 Schematics showing the (a) C-AFM (tip plane geometry) and (b) device measurements (plane parallel geometry). The current spread out from the C-AFM tip allowing larger density of space charge limited current under the probe than the plane parallel electrodes.

In order to explain this, the differences between planar electrode configuration and C-AFM configuration have to be explained. The C-AFM configuration has two peculiarities when compared to plane electrode system: a) it has sphere-plane contact system where the C-AFM tip apex is hemispherical and the back contact is planar, b) point probe contact system as the contact area at the tip-sample interface is of the order of few nanometers. In sphere plane contact system charges are injected / collected radially at the probe sample contact. The current is spread out from the C-AFM tip allowing larger density of space charge limited current under the probe than the plane parallel electrodes. Considering the nature of electric field between the contacts in sphere-plane configuration, Lampert et al. [25] has modified the Mott-Gurney law for sphere plane geometry (carriers injected from the tip) in which current is given by the following analytic equation

$$I = \frac{3}{2}\pi\varepsilon_0\varepsilon_r\mu\frac{V^2}{L} \tag{3.2}$$

Wherein I is the current, ε_0 is the permittivity in free space, ε_r is the relative permittivity of the sample, μ is the mobility and L is the distance between two electrodes. From the modified equation, with thickness of the film the current collected between the electrodes in sphere plane configuration should decrease. However, Desbief et al. [26] in their work on polymer films (P3HT) with C-AFM reported that the C-AFM current intensity on the film is independent on the distance between the C-AFM tip and the back electrode. This result contradicts the modified Mott-Gurney equation for sphere plane geometry by Lampert, despite the sphere plane configuration of C-AFM. Desbief et al. argued that this is a direct consequence of the nanometric size of the injecting C-AFM probe, such that the probed current is local in nature. The dominating resistance that limits the value of the current signal in C-AFM configuration is expected to be that of the tip–sample contact, resulting from spreading mechanisms [14]. Considering these two peculiarities of C-AFM configuration, i.e. the sphere plane geometry and point probe geometry, the Mott-Gurney law has to be modified further taking into account the tip radius, applied force on the tip, penetration depth, lateral expansion of the field etc.

In order to better define the operation of C-AFM, a model is introduced by Moerman et al. of University of Mons [27]. Here the total resistance offered by the C-AFM set up while probing the

sample is considered and compared. The electrical equivalent of C-AFM set up is modeled with four resistances connected in series as shown in Figure 3-10(a), where

$$R_{total} = R_{ext} + R_{tip} + R_t + R_{cathode} \quad (3.3)$$

Where R_{total} is the total resistance of the system, R_{ext} is the resistance offered by the external circuit which includes among others the resistances of tip cantilever, the external wires and the amplifier electrical detection module. R_{tip} and $R_{cathode}$ are the contact resistances (R_c) at tip sample interface and cathode sample interface respectively, while R_t is the transport resistance through the organic semiconductor. It has to be noted that the highest resistance in the circuit will limits the current flow.

R_{ext} which includes among others, the resistances of tip cantilever, the external wires and the amplifier electrical detection module is typically of the order of ohms as the components involved in the external circuitry are highly conducting inorganic materials. The transport resistance across the organic semiconductor sample can be expressed as

$$R_t = \frac{L \cdot \rho_{film}}{W.t} \quad (3.4)$$

Where in ρ_{film} is the resistivity of the organic semiconductor film under investigation, L is the distance between the tip and the back electrode (cathode), t is the thickness of the film and W is the width of the back contact as schematically represented in Figure 3-10(b). It has to be noted that the transport resistance of typical organic semiconductors are of the order of several Giga ohms [28, 29].

The contact resistance is generally expressed in terms of the following equation [30]

$$R_c = \frac{\rho}{4r} \quad (3.5)$$

Where r is the radius of the contact area while ρ is the resistivity of the material. Approximating the sample-cathode contact area with the shape of a disc with radius r, the contact resistance at the cathode-sample interface can be estimated using equation (3.5). Usually the cathode-sample contact area in C-AFM configuration has typical contact radius of the order of millimeters, and

the expected R_c is of the order of kilo ohms. But in the case of tip-sample interface the hemispherical apex of the C-AFM tip has radius of the order of few nanometer, and the resulting contact has a nanoscale contact radius. This implies the R_c at tip sample interface will be of the order of Giga ohms. Spreading resistance originates owing to the nanometric area of the tip sample contact, generates a confinement of current flow across the contact (see Figure 3-9 (b)). Assuming no electronic barrier at the tip sample contact and R_c entirely dominated by spreading mechanisms, the hemispherical geometry of the apex of the tip should yield

$$R_c = R_{tip} = \frac{\rho_{local}}{4r_0} \tag{3.6}$$

Here ρ_{local} is the resistivity of the film at the tip sample contact and r_0 is the contact radius at the tip-sample interface.

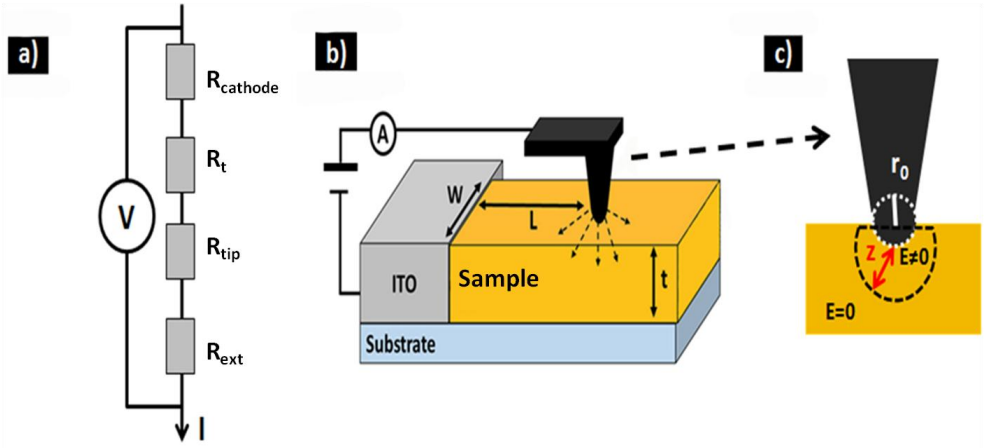

Figure 3-10 (a) Equivalent electrical circuit of C-AFM tip sample system where in R_{ext} represents the resistance of the external circuitry, R_{tip} is the contact resistance between the tip and the sample, R_t is the transport resistance and $R_{cathode}$ is the resistance at the interface between sample and the back electrode. (b) Schematic description of the current injection from the tip into the sample within a sphere-plane geometry (c) with r_0 the contact radius and Z the radius of the electric field expansion under the tip. L is the distance between the tip and the back contact electrode, t is the thickness of the film and W is the width of the back contact.

Comparing the values of four resistances that contribute to the total resistance R_{total} from the paragraph above, it is evident that the, from R_{ext} is negligibly small when compared to that of the two contact resistances $(R_c = R_{tip} + R_{cathode})$ and R_t. Also since $R_{cathode} << R_{tip}$, $R_c \sim R_{tip}$. This implies R_t and R_c are the two resistances which restricts the charge transport, when probed through C-AFM.

A ratio θ between R_t and R_c is defined, in view of finding out the dominant resistance which limits the current flow through the circuit

$$\theta = \frac{R_t}{R_s} = \frac{\rho_{film}}{\rho_{Local}} \frac{4Lr_0}{Wt} \tag{3.7}$$

Assuming that at the voltage range typically applied in C-AFM, the local resistivity of organic semiconductor at the tip sample contact remains close to the resistivity of the film, the variation of θ is solely dependent on geometrical parameters. This implies that according to variation in geometrical parameters two types of current regimes are possible

1. Contact resistance dominating regime corresponding to $\theta < 1$
2. Transport resistance dominating regime corresponding to $\theta > 1$

In our experimental configuration, L is of the order of few microns, thickness of the film is few tens of nanometers and W is of the order of centimeters. This implies that while scanning within a few tens of micrometer distance from the back electrode, $\theta << 1$ and R_t is negligible compared to R_c. This leads to contact resistance dominated regime, justify independent variation of current with L and thereby ensuring a local probing of the electrical properties of the organic film under investigation. The possibility to probe local electrical properties of a thin film in spreading resistance dominated regime makes C-AFM a very powerful tool for electrical characterization of sophisticated organic devices.

In such local resistance dominating regime the Mott-Gurney law for plane parallel electrodes has to be modified to account for local probing of current. This is done by solving the Poisson's equation, by considering contact resistance as a result of the tip-plane geometry. The analytical expression for modified Mott-Gurney equation when carriers are injected from point tip is [27].

$$I = 3\pi\varepsilon_0\varepsilon_r\mu r_0\frac{V^2}{(Z-r_0)^2} \tag{3.8}$$

Wherein μ is the local mobility of organic semiconductor just underneath the tip (in the probed volume), r_0 is the contact radius and Z is the radius of the hemisphere beyond which the voltage drops and the field tends to zero, with assumed value less than 30 nm. It has to be noted that the typical Mott-Gurney law has an inverse L^3 dependence on the J, however the modified Mott-Gurney law there is no dependence of L suggesting local probing of current. By this equation, the quadratic variations of the current with the voltage are used to extract the local mobility value. Hertzian contact model can be used to estimate the contact radius at the tip sample interface, r_0 assuming a perfectly elastic deformation at the contact. The equation for r_0 by Hertzian contact model is the following

$$r_0^3 = \frac{3\ Rtip\ F}{4E} \tag{3.9}$$

Wherein R_{tip} is the tip radius, F is the applied force between the tip and the sample surface and E is the Young's modulus of organic semiconductor.

3.3 X-ray diffraction (XRD)

X-ray diffraction is a powerful technique for the structural characterization of materials. In crystalline materials, all atoms are considered as sets of parallel crystallographic planes which are characterized by Miller indices ($h\ k\ l$). During XRD measurements, X-ray beam with a particular wavelength (λ) is incident on the crystalline sample. As the wavelength of X-ray is comparable to the inter-atomic distances in solids, X-rays will get diffracted by the different crystallographic planes in the sample into many specific directions. This will give rise to specific diffraction patterns due to interference effects between rays scattered by different planes. The necessary condition for certain set of crystallographic planes produce constructive interference to give diffraction maxima is provided by the Bragg law

$$2dsin\theta = n\lambda \tag{3.10}$$

Here *d* is the spacing between diffracting planes, θ is the incident angle, *n* is the order of diffraction, and λ is the wavelength of the beam and θ is the angle between the incident and the diffracted X-ray beams. Typically, X-Ray diffraction patterns are represented as the scattering intensity versus 2θ (in degrees) with each reflection on this pattern corresponds to the set of parallel crystallographic planes (*h k l*). XRD experiments were performed recording specular scans ($\theta/2\theta$ mode) with a Panalytical X'Pert Pro powder diffractometer in Bragg- Brentano parafocusing geometry, using Cu K_α radiation (λ = 1.54 Å) over a 2θ range of 3° to 50°,a step size of 0.02°, an interval of 10 s. Here the sample is stationary in the horizontal position, both the X ray tube and the detector move simultaneously over the angular range θ. During the analysis, the sample surface is always at an angle of θ and the detector is always at an angle of 2θ with respect to the incident X-ray beam. In this XRD configuration, the only detected diffraction peaks will be those corresponding the lattice planes oriented parallel to the sample surface [31].

3.4 Optical spectroscopy

Polarized optical absorption measurements were performed at normal incidence in transmission mode in the spectral range from 1.5 to 5 eV using a UV-Vis-NIR spectrophotometer Perkin-Elmer Lambda 900, equipped with a depolarizer and Glan-Taylor calcite polarizers. It makes use of Beer-Lambert's law, which relates the absorption of light to the number of molecules in the path through which the light is travelling.

$$A = log\ I_0/I = \varepsilon.\ c.\ l \qquad (3.11)$$

Wherein *A* is the absorbance measured, I_0 is the intensity of the incident light, *I* is the transmitted intensity, *l* the path length through the sample, and c the concentration of the absorbing species and ε is the molar extinction coefficient (L mol^{-1} cm^{-1}).

3.5 Materials and samples

Three different organic molecules are introduced in this thesis. First two belongs to the category of low molecular weight small molecules, α-quaterthiophene and α-sexithiophene while the third one belongs to the category of polymers, poly (3-hexylthiophene-2,5-diyl).

3.5.1 α-Quaterthiophene (4T)

4T belongs to the family of oligothiophenes, π-conjugated organic molecules of different chain length, consisting of thiophene rings (C_4H_4S) as subunits. The thiophene subunits are bonded with each other by σ-bonds via its α-carbon atoms to form small chain length oligomers of thiophene termed as α-nT (see Figure 3-11 Thiophene monomer presented with the atomic nomenclature for the carbon atoms. n represents the number of conjugated rings in a given oligothiophene., 4T consists of four thiophene subunits bonded likewise.

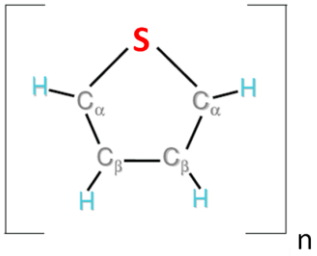

Figure 3-11 Thiophene monomer presented with the atomic nomenclature for the carbon atoms. n represents the number of conjugated rings in a given oligothiophene.

Since 4T has a higher vapor pressure, allowing reduced temperatures for thin-film growth processes at relatively low temperature, together with its solubility, makes it a good candidate for device fabrication, especially organic FETs [32]. Two polymorphs are known for 4T: the low temperature (4T/LT) and the high temperature (4T/HT) polymorphs, both displaying a monoclinic structure characterized by a layered herringbone arrangement of the molecules (Figure 3-12 (a) and (b)) [33]. For the LT polymorph, the unit cell parameters are a = 6.09 Å, b = 7.86 Å, c = 30.48 Å, and β = 91.81◦, and the cell contains four molecules.

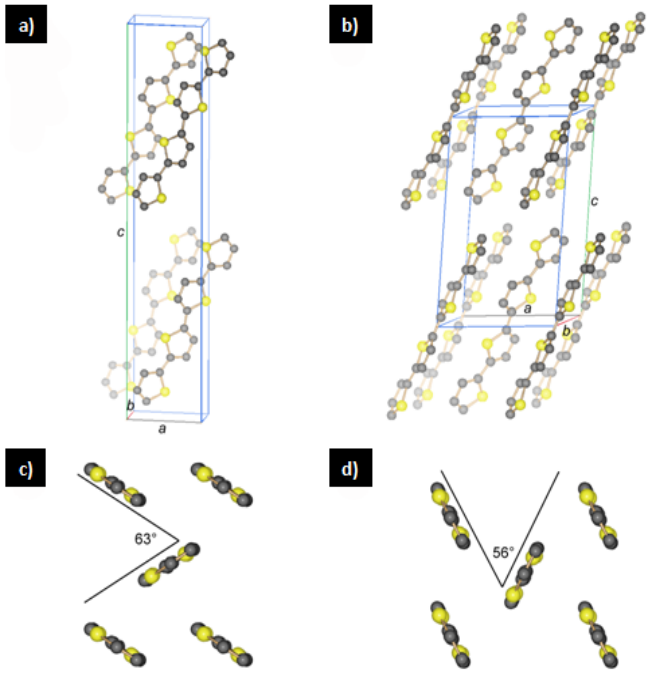

Figure 3-12 (a) Crystal structure of 4T/LT, and (b) 4T/HT (H-atoms omitted). (c) Molecular orientation as viewed along the [52 0 21] direction of 4T/LT and (d) as viewed along the [33 0 42] direction of 4T/HT. The herringbone angle is also reported.

For the HT polymorph, the unit cell parameters are a = 8.94 Å, b = 5.75 Å, c = 14.34 Å, and β = 97.22°, and the cell contains two molecules. The main difference between the two polymorphs is the tilt angle of the long molecular axis with respect to the (001) plane and the herringbone angle (see Figure 3-12). Noteworthy, 4T/HT was never observed in thin films, while the usually favored polymorphic phase of 4T is the low temperature one (4T/LT).

Substrates

The substrates used for the growth of epitaxial thin films of 4T are commercial (010) oriented potassium hydrogen phthalate (KAP) and (001)-oriented pentaerythritol (PET) single crystals.

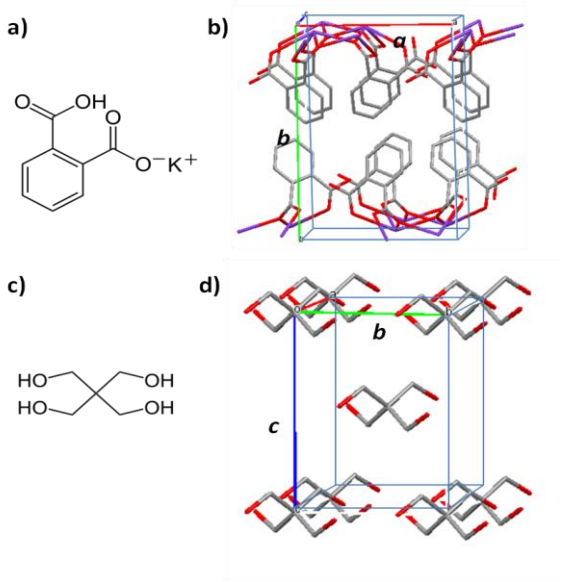

Figure 3-13 (a) KAP molecule (b) Crystal structure of KAP (H-atoms omitted). (c) PET molecule (d) Crystal structure of PET (H-atoms omitted). Purple, red, and grey caps represent K-, O-, and C-atoms, respectively.

Potassium hydrogen phthalate (KAP) single crystals were purchased from Ekspla (Vilnius, Lithuania). KAP crystals belong to the orthorhombic system, with unit cell axes a = 6.48 Å, b = 9.61 Å, and c = 13.33 Å and space group $Pca2_1$ [34]. Figure 3-13 (a) and (b) shows the molecular structure and crystal structure of KAP respectively. The molecularly flat (010) surface of the crystal is prepared by mechanical cleavage in air immediately before the deposition, with cleaving direction parallel to $[101]_{KAP}$ [35]. The cleavage surface is a corrugated one, exposing the phenyl rings which are tilted relative to each other whereas the potassium ions are located in layers beneath.

The pentaerythritol (PET, $C_5H_{12}O_4$) substrates were provided by Fujian Institute of Research on the Structure of Matter, China; they were grown by cooling an aqueous saturated solution of PET, prepared at 75°C using materials with 98% purity. Small clear and transparent slabs, approximately 1 to 2 mm thick and oriented parallel to the (001) plane, were cleaved from the PET crystals grown by spontaneous nucleation and then used as seeds. The seeds were then glued

onto a rod clothed with a plastic pipe and introduced into the saturated solution to grow pure samples [36]. PET crystals belong to the tetragonal system, space group $I\bar{4}$, with $a = b = 6.079$ Å and $c = 8.745$ Å unit cell axes and two molecules per unit cell. Figure 3-13 (a) and (b) shows the molecular structure and crystal structure of PET respectively. Freshly cleaved PET substrates with cleavage plane (001), with a peculiar corrugation interesting in view of epitaxy is used for deposition.

Film growth

In view of deposition, 4T was synthesized by a standard procedure [37] and then purified repeatedly by vacuum evaporation. Thin films of 4T were grown by OMBE at 5×10^{-10} Torr base pressure, with 170°C deposition temperature, while keeping the substrate at room temperature. The sources were Knudsen type effusion cells with double heater and double temperature control. The nominal film thickness was monitored by a quartz microbalance mounted close to the substrate [38, 39]. Films of various thicknesses from 5 nm to 50 nm were deposited with a rate of deposition of 8 Å/min.

3.5.2 α-Sexithiophene (6T)

Sexithiophene ($C_{24}H_{14}S_6$) is also called as α-hexathiophene, α-hexathienyl or α-sexithienyl belongs to the class of p-type organic semiconductors. It is a planar, rod like aromatic organic molecule. It belongs to the family of oligothiophenes and consists of six conjugated thiophene rings. 6T is stable in air, easily vacuum processable, exhibits both high conjugation of π-electrons and high crystallinity in the solid state. There are strong intermolecular π-π interactions between the molecules, which arises due to relatively high molecular weight and conjugation of the molecule. As a result, two-dimensional nucleation and the subsequent layer-by-layer growth of the thin film phase is possible on inert substrates by deposition techniques in vacuum, makes the molecule very interesting for devices like organic FETs [40-43]. 6T crystallizes in a layered structure, stacked in a herringbone fashion with molecules all parallel to one another, and the molecules are tilted to the lamellar plane [44].

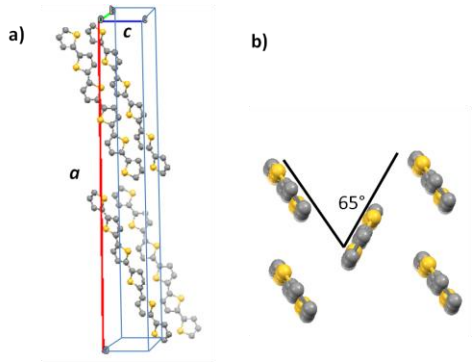

Figure 3-14 (a) Crystal structure of 6T/LT, (H-atoms omitted). (b) Herringbone angle is presented.

In crystals, occurrence of two polymorphs are known: the low temperature (6T/LT) and the high temperature (6T/HT) polymorphs, named after their preparation method[45]. The unit cell structure of both polymorphs is monoclinic in nature with 4 and 2 molecules per unit cell for 6T/LT and 6T/HT, respectively. The 6T/LT phase is well studied and experimentally easier to obtain compared to 6T/HT (unit cell and herringbone angle reported in Figure 3-14). However, Servet et al. have reported the presence of polymorphism [46] in 6T thin films with cell parameters different from those of the single crystal, while Porzio et al. has reported different 6T unit cell parameters from powder [47]. The existence of such thin film phases is dependent on the growth parameters.

Table 3-1 presents the reported unit cell parameters of 6T by XRD studies. On inert surfaces like amorphous glass, silicon oxide or indium tin oxide (ITO), the 6T molecules adsorb in so-called standing orientation with its long molecular axis nearly perpendicular to the surface. However, depending on the type of substrate, the growth conditions and the number of monolayers, the molecular orientation can get quite complex. The highest occupied molecular orbital (HOMO) and the lowest unoccupied molecular orbital (LUMO) was experimentally determined to 5.2 eV and 3.1 eV respectively [49].

Table 3-1 Unit cell parameters, tilt angle of the molecular axis to the lamellar plane normal *(β)*, herringbone angle *(τ)*, and interlayer spacing of the known crystalline structures of 6T [48]

	6T-Porzio	6T/LT	6T/HT	6T-Servet
a (Å)	45.38	44.71	9.14	5.98
b (Å)	7.86	7.85	5.68	7.80
c (Å)	6.03	6.03	20.67	50.28
β(°)	99.0	90.76	98.0	111.3
ϕ(°)	23.8	24.1	33.6	21.3
τ(°)	62	65	55	62
Interlayer spacing (Å)	$d_{(200)} = 22.41$	$d_{(200)} = 22.35$	$d_{(001)} = 20.48$	$d_{(002)} = 23.42$

Substrates

ITO patterned glass substrates are used for depositing 6T using OMBE. 3×3 cm^2 substrates are purchased from 'Naranjo substrates' (see Figure 3-15 (a)). Prior to the OMBE deposition, the substrates are cleaned by a cycle of ultrasonic baths with soap solution, de-ionized water and acetone with each step lasting for 15 min. Afterwards, the substrates are dried by a stream of nitrogen gas. The substrates are then cut in to smaller pieces and used for deposition. AFM phase images of the surface of the ITO and glass substrates are presented in Figure 3-15 (b) and (c) respectively. ITO surface consists of grains of various sizes ranging from 150 to 350 nm in diameter. The r.m.s roughness estimated from 2×1 μm^2 AFM height image (not shown) is 9.1 nm. These ITO grains are expected to play a role on the surface morphology of the organic molecules grown on top of it. The surface of glass is comparatively smooth with respect to ITO, with r.m.s roughness of 1.3 nm.

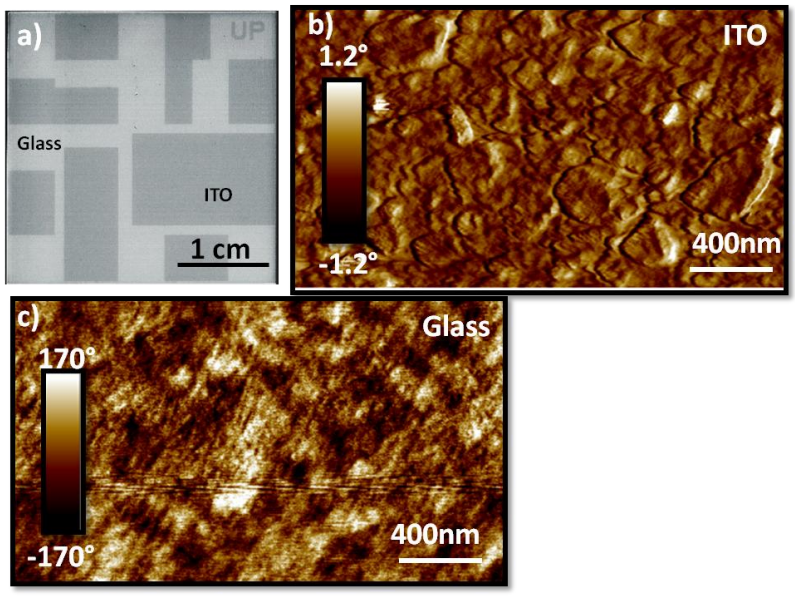

Figure 3-15 (a) Image of 3× 3 cm^2 area of commercially available ITO patterned glass substrate. (b) 2 × 1 µm^2 AFM phase image of ITO surface. (c) 2 × 1 µm^2 AFM phase image of glass surface.

Film growth

Commercially available 6T microcrystalline powder is purified repeatedly using vacuum sublimation prior to OMBE deposition. 6T thin films were then grown on ITO patterned glass substrate by means of OMBE. Thin films of 6T were grown by OMBE at 5×10^{-10} Torr base pressure, with 245°C deposition temperature, while keeping the substrate at room temperature, while the thickness of the film is monitored by a quartz microbalance. Films of thickness varying from 5 nm to 40 nm were deposited with a rate of deposition of 2Å/min.

3.5.3 Poly (3-hexylthiophene-2,5-diyl) (P3HT)

The second category of organic electronic materials is conjugated polymers, lighter, more flexible and less expensive materials. The presence of side alkyl chains, along the chain backbone increases the solubility of the material. This allows easier solution based processing than their small molecule counterparts. This makes polymers a desirable alternative in many device applications like organic solar cells, OLEDS, OFETs etc although they cannot reach a high

degree of structural order. Among conjugated polymers, poly (3-hexylthiophene-2,5-diyl) (P3HT) (see Figure 3-16 (a)) is one of the well studied and most promising polymers for device applications. For example, efficiencies over 6.5% has been reported for organic solar cells that used regioregular P3HTs as the donor material [50].

P3HT can crystallize to form fibrils, depending upon the degree of regioregularity, defined as the percentage of monomers adopting a head-to-tail (HT) configuration rather than head-to-head (HH) [51]. Regioregularity of conjugated polymers is well known to be an important factor to determine their order in the solid state such as crystallinity and molecular orientation [52, 53]. It has also been reported that a higher regioregularity leads to better interchain interactions [54], better morphological order leads to better charge mobility [55]. So in view of devices, higher the regioregularity, better the device performance.

The fibrillar morphology is the signature of crystalline ordering in regioregular P3HT chains while the absence of any such fibrils reveals the lack of self assembling of polymer chains. In each fibrils, the P3HT molecules have extended conjugated backbones with adjacent molecules stacking face to face and the long axis perpendicular to the fibril axis (which is also the π-stacking direction) [56]. Also, the plane of the conjugated backbone is perpendicular to the substrate. A schematic representation of crystallization of P3HT fiber is illustrated in Figure 3-16 (b), and hopping of holes through the π- stacking is also reported in the same figure.

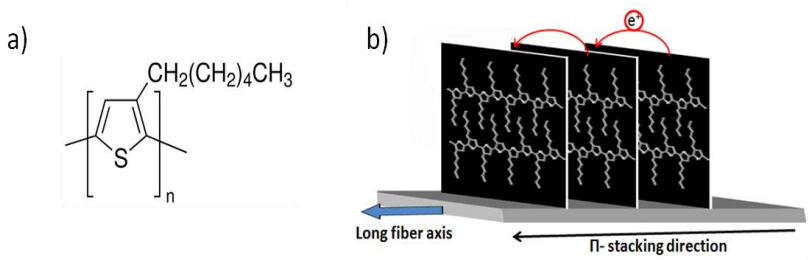

Figure 3-16 (a) Molecular structure of P3HT. (b) Schematic representation of the crystallization of regioregular-P3HT chains into one fibril due to π- stacking of the conjugated backbones. The hopping of holes through the π- stacking is also illustrated.

Substrates

The substrates used for deposition of P3HT thin films are cleaned ITO patterned glass substrate and the details of substrate are explained in the previous sections (see Figure 3-15)

Film growth

P3HT polymer with different degree of regioregularity was prepared in Laboratory for Polymer Synthesis, KU Leuven by Willot et al.[57]. Thin films of the P3HT with different degree of regioregularity (56%, 83%, 89%, 95% and 100%) were deposited on ITO patterned glass substrates by means of solvent assisted drop casting with chlorobenzene as solvent, at a concentration of 0.2 mg mL^{-1}. 25 mL cm^{-2} of the solutions was drop casted on glass substrates and allowed the solvent to evaporate overnight in a solvent-saturated atmosphere. The saturated atmosphere results the solvent to evaporate slowly, in turn generating the film morphologies approaching thermodynamic conditions. However, this process yields films with thickness less than 20 nm.

3.6 References

1. Sassella, A., M. Campione, and A. Borghesi, *Organic epitaxy*. La rivista nuovo cimento, 2008. **31**(8): p. 457 - 490.
2. Forrest, S.R., *Ultrathin Organic Films Grown by Organic Molecular Beam Deposition and Related Techniques.* Chem Rev, 1997. **97**(6): p. 1793-1896.
3. Hyun Kim, C., et al., *Modeling the low-voltage regime of organic diodes: Origin of the ideality factor*. Journal of Applied Physics, 2011. **110**(9): p. -.
4. Campione, M., et al., *Thickness measurements by quartz microbalance during thin-film growth by organic-molecular-beam deposition.* Journal of Vacuum Science & Technology A, 2004. **22**(3): p. 482-486.
5. Goletti, C., et al., *Highly sensitive optical monitoring of molecular film growth by organic molecular beam deposition.* Applied Physics Letters, 2003. **83**(20): p. 4146-4148.
6. Binnig, G., C.F. Quate, and C. Gerber, *Atomic Force Microscope*. Physical Review Letters, 1986. **56**(9): p. 930-933.

7. Giessibl, F.J., *Advances in atomic force microscopy.* Reviews of Modern Physics, 2003. **75**(3): p. 949-983.
8. Sheiko, S.S. and M. Moller, *Atomic Force Microscopy of Polymers: Imaging, Probing and Lithography*, in *Macromolecular Engineering*. 2007, Wiley-VCH Verlag GmbH & Co. KGaA. p. 1515-1574.
9. Raimondo, L., et al., *Epitaxial Interfaces in Rubrene Thin Film Heterostructures.* The Journal of Physical Chemistry C, 2013. **117**(27): p. 13981-13988.
10. Campione, M., et al., *Organic−Organic Heteroepitaxy of Semiconductor Crystals: α-Quaterthiophene on Rubrene.* Chemistry of Materials, 2009. **21**(20): p. 4859-4867.
11. Sassella, A., et al., *Optical properties of highly oriented quaterthiophene thin films grown by organic molecular-beam deposition.* Physical Review B, 2000. **62**(16): p. 11170-11176.
12. Andrea, A. and F. Paolo, *AFM: a versatile tool in biophysics.* Measurement Science and Technology, 2005. **16**(6): p. R65.
13. Gross, L., et al., *The Chemical Structure of a Molecule Resolved by Atomic Force Microscopy.* Science, 2009. **325**(5944): p. 1110-1114.
14. Moerman, D., R. Lazzaroni, and O. Douheret, *Efficient bulk heterojunction photovoltaic cells with a pre-organized poly(3-hexylthiophene) phase.* Applied Physics Letters, 2011. **99**(9): p. 093303.
15. Ionescu-Zanetti, C., et al., *Semiconductive Polymer Blends: Correlating Structure with Transport Properties at the Nanoscale.* Advanced Materials, 2004. **16**(5): p. 385-389.
16. Alexeev, A., J. Loos, and M.M. Koetse, *Nanoscale electrical characterization of semiconducting polymer blends by conductive atomic force microscopy (C-AFM).* Ultramicroscopy, 2006. **106**(3): p. 191-199.
17. Palermo, V., et al., *Exploring nanoscale electrical and electronic properties of organic and polymeric functional materials by atomic force microscopy based approaches.* Chemical Communications, 2007(32): p. 3326-3337.
18. Lenes, M., et al., *Recombination-Limited Photocurrents in Low Bandgap Polymer/Fullerene Solar Cells.* Advanced Functional Materials, 2009. **19**(7): p. 1106-1111.

19. Mihailetchi, V.D., et al., *Compositional Dependence of the Performance of Poly(p-phenylene vinylene):Methanofullerene Bulk-Heterojunction Solar Cells.* Advanced Functional Materials, 2005. **15**(5): p. 795-801.
20. Kuik, M., et al., *The Effect of Ketone Defects on the Charge Transport and Charge Recombination in Polyfluorenes.* Advanced Functional Materials, 2011. **21**(23): p. 4502-4509.
21. Beiley, Z.M., et al., *Morphology-Dependent Trap Formation in High Performance Polymer Bulk Heterojunction Solar Cells.* Advanced Energy Materials, 2011. **1**(5): p. 954-962.
22. Douheret, O., et al., *Nanoscale electrical characterization of organic photovoltaic blends by conductive atomic force microscopy.* Applied physics letters, 2006. **89**(3): p. 032107.
23. Reid, O.G., K. Munechika, and D.S. Ginger, *Space Charge Limited Current Measurements on Conjugated Polymer Films using Conductive Atomic Force Microscopy.* Nano Letters, 2008. **8**(6): p. 1602-1609.
24. Lin, H.-L., et al., *Nanoscale charge transport in an electroluminescent polymer investigated by conducting atomic force microscopy.* Applied physics letters, 2002. **81**(14): p. 2572-2574.
25. Lampert, M.A., A. Many, and P. Mark, *Space-Charge-Limited Currents Injected from a Point Contact.* Physical Review, 1964. **135**(5A): p. A1444-A1453.
26. Desbief, S., et al., *Nanoscale investigation of the electrical properties in semiconductor polymer-carbon nanotube hybrid materials.* Nanoscale, 2012. **4**(8): p. 2705-2712.
27. Moerman, D.L., Ph.; Lazzaroni, R. and Douhéret, O., *Identifying charge transport mechanisms in conductive atomic force microscopy studies of semiconducting polymers.(To be submitted).*
28. Kelley, T.W. and C.D. Frisbie, *Gate Voltage Dependent Resistance of a Single Organic Semiconductor Grain Boundary.* The Journal of Physical Chemistry B, 2001. **105**(20): p. 4538-4540.
29. Hunter, S. and T.D. Anthopoulos, *Observation of Unusual, Highly Conductive Grain Boundaries in High-Mobility Phase Separated Organic Semiconducting Blend Films Probed by Lateral-Transport Conductive-AFM.* Advanced Materials, 2013. **25**(31): p. 4320-4326.

30. Holm, R., *Electrical Contacts: Theory and Application.* New York:Springer-Verlag, 1967.
31. Birkholz, M., *Thin film analysis by x-ray scattering*. 2006, Federal Republic of Germany: Wiley-VCH Verlag GmbH.
32. E. Katz, H., *Organic molecular solids as thin film transistor semiconductors.* Journal of Materials Chemistry, 1997. **7**(3): p. 369-376.
33. Siegrist, T., et al., *Crystal Growth, Structure, and Electronic Band Structure of α-4T Polymorphs.* Advanced Materials, 1998. **10**(5): p. 379-382.
34. Eremina, T.A., Furmanova,N. G., L. F. Malakhova, T. M. Okhrimenko, and and V. A. Kuznetsov, Crystallogr. Rep, 1993. **38**: p. 554.
35. Borc, J. and K. Sangwal, *Study of the orientation and frequency of occurrence of elementary steps on the (0 1 0) cleavage face of potassium acid phthalate single crystals.* Surface Science, 2004. **555**(1–3): p. 1-10.
36. BU Huan-Huan, Z.X.-X., *Rapid Growth of Pentaerythritol Crystal.* Chinese J. Struct. Chem., 2011. **30**(1).
37. Trabattoni, S., et al., *Preparation of highly pure quaterthiophene and role of impurities on its photoluminescence properties.* Journal of Materials Chemistry, 2004. **14**(2): p. 171-178.
38. Sassella, A., et al., *Pseudomorphic growth of organic semiconductor thin films driven by incommensurate epitaxy.* Applied Physics Letters, 2009. **94**(7): p. -.
39. Sassella, A., et al., *Epitaxial growth of organic heterostructures: Morphology, structure, and growth mode.* Surface Science, 2007. **601**(13): p. 2571-2575.
40. Garcia, R., et al., *Size and Shape Controlled Growth of Molecular Nanostructures on Silicon Oxide Templates.* Nano Letters, 2004. **4**(6): p. 1115-1119.
41. Loi, M.A., et al., *Supramolecular organization in ultra-thin films of α-sexithiophene on silicon dioxide.* Nature Materials, 2004. **4**(1): p. 81-85.
42. Dinelli, F., et al., *Spatially Correlated Charge Transport in Organic Thin Film Transistors.* Physical Review Letters, 2004. **92**(11).
43. Horowitz, G., et al., *A field-effect transistor based on conjugated alpha-sexithienyl.* Solid State Communications, 1989. **72**(4): p. 381-384.

44. Fichou, D., *Structural order in conjugated oligothiophenes and its implications on opto-electronic devices.* Journal of Materials Chemistry, 2000. **10**(3): p. 571-588.
45. Kloc, C., et al., *Physical vapor growth of centimeter-sized crystals of α-hexathiophene.* Journal of Crystal Growth, 1997. **182**(3–4): p. 416-427.
46. Servet, B., et al., *Polymorphism and Charge Transport in Vacuum-Evaporated Sexithiophene Films.* Chemistry of Materials, 1994. **6**(10): p. 1809-1815.
47. Tubino, R., et al., *A new apparatus for ultra-high vacuum organic molecular beam deposition.* Optical Materials, 1998. **9**(1–4): p. 437-444.
48. Campione, M., et al., *Structural characterisation of ultra-high vacuum sublimated polycrystalline thin films of hexathiophene.* Thin Solid Films, 2006. **500**(1-2): p. 169-173.
49. Loiacono, M.J., E.L. Granstrom, and C.D. Frisbie, *Investigation of Charge Transport in Thin, Doped Sexithiophene Crystals by Conducting Probe Atomic Force Microscopy.* The Journal of Physical Chemistry B, 1998. **102**(10): p. 1679-1688.
50. Zhao, G., Y. He, and Y. Li, *6.5% Efficiency of Polymer Solar Cells Based on poly(3-hexylthiophene) and Indene-C60 Bisadduct by Device Optimization.* Advanced Materials, 2010. **22**(39): p. 4355-4358.
51. Kim, Y., et al., *A strong regioregularity effect in self-organizing conjugated polymer films and high-efficiency polythiophene:fullerene solar cells.* Nat Mater, 2006. **5**(3): p. 197-203.
52. Sirringhaus, H., et al., *Two-dimensional charge transport in self-organized, high-mobility conjugated polymers.* Nature, 1999. **401**(6754): p. 685-688.
53. Kohn, P., et al., *On the Role of Single Regiodefects and Polydispersity in Regioregular Poly(3-hexylthiophene): Defect Distribution, Synthesis of Defect-Free Chains, and a Simple Model for the Determination of Crystallinity.* Journal of the American Chemical Society, 2012. **134**(10): p. 4790-4805.
54. Jiang, X.M., et al., *Spectroscopic Studies of Photoexcitations in Regioregular and Regiorandom Polythiophene Films.* Advanced Functional Materials, 2002. **12**(9): p. 587-597.
55. Jiang, X., et al., *A transport study of poly(3-hexylthiophene) films with different regioregularities.* Synthetic Metals, 2003. **135–136**(0): p. 351-352.

56. Surin, M., et al., *Regioregular poly(3-hexylthiophene)-poly(ε-caprolactone) block copolymers: Controlled synthesis, microscopic morphology, and charge transport properties.* Organic Electronics, 2010. **11**(5): p. 767-774.
57. Willot, P., et al., *Poly(3-alkylthiophene) with tuneable regioregularity: synthesis and self-assembling properties.* Polymer Chemistry, 2013. **4**(9): p. 2662-2671.

Chapter 4

4 Epitaxy of α-Quaterthiophene

Introduction

Among the organic molecules suitable for electronic applications, α-Oligothiophenes form an important class under the category of small molecules [1]. This is therefore one of our choice. In this section of the thesis we will present the results on the morphological, optical and structural characterization of epitaxial thin films of α-quaterthiophene (4T) grown on two different organic single crystal substrates namely potassium hydrogen phthalate (KAP) and pentaerythritol (PET) using OMBE, and to corroborate the results, the molecular packing within the film, along with its epitaxial relationship with the substrate is determined. KAP (010) is known to induce the growth of crystalline 4T films having the structure of the LT polymorph [2] which is used as a reference to understand the structural and morphological characteristics of 4T on PET. Also, here we show how a proper choice of the substrate permits to select not only specific orientations, but also polymorphic and pseudomorphic phases of the overlayer by comparing the results of the epitaxial films grown on both substrates [3-5]. The possibility of growing crystalline organic thin films on various organic substrates can be of great interest in fundamental studies as well as in the field of novel photovoltaic applications like cascade organic solar cells [6]. In such applications, the donor layer of the cell is made by combining different organic materials with complementary light absorption ranges demonstrating how the control and study of organic-organic interface to be particularly relevant.

4.1 α-Quaterthiophene thin films on potassium acid phthalate (KAP) single crystal substrate

The crystal structure and physical properties of 4T and KAP along with the description of the growth process of 4T epitaxial thin films on KAP single crystals is presented in section 3.5.1. The KAP (010) surface presents peculiar structural features that are very interesting in the context of organic epitaxy, presented in Figure 4-1. The reason for selecting this substrate is, the presence of phthalate conjugated rings surfacing at the cleavage plane, which is believed to induce, a specific orientation of the 4T molecules through the π-π interactions [7]. This section of the thesis is devoted to the structural, optical and morphological characterization of the samples.

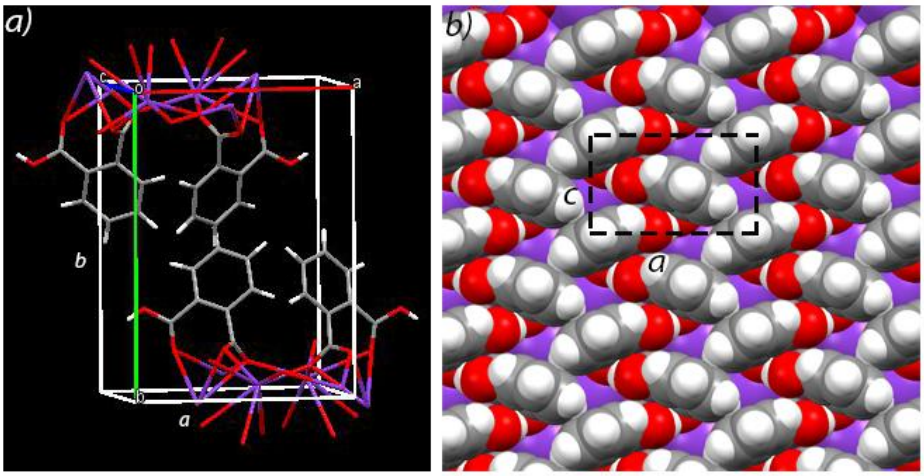

Figure 4-1 (a) Orthorhombic crystal structure of KAP. (b) Caps model of the KAP (010) surface. White, red, purple, and grey caps represent H-, O-, K-, and C-atoms, respectively.

4.1.1 Structural characterization

The structural properties of 15 nm 4T films, grown on KAP (010) by OMBE at room temperature are investigated by XRD in *θ-2θ* configuration and the out-of-plane molecular packing is inferred. The measurements are performed in such a way that only reflections observed are those coming from the families of lattice planes parallel to the substrate surface can be observed. However, in this configuration, most of the diffracted intensity would come from the thick KAP crystalline

substrate (usually the thickness of the cleaved KAP substrate is around 100 μm); as a result the strong diffraction peaks of the crystalline substrate would conceal the weaker peaks originating from the thinner 4T overlayers.

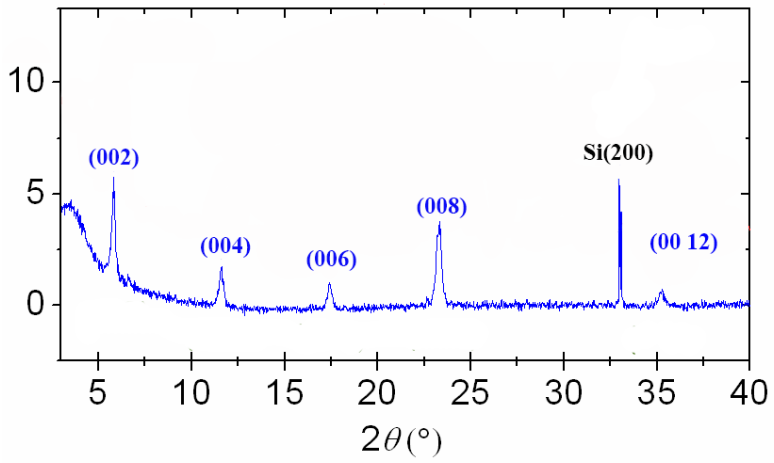

Figure 4-2 X-ray diffractogram collected in *θ-2θ* geometry with a Cu-K_α X-ray source, from a 4T thin film with a nominal thickness of 15nm grown on top of KAP(010) single crystal. The (00*l*) peaks (labeled in blue, where *l* is even) arise from the 4T film, while the silicon (200) (marked in black) originates from the silicon substrate used as a rigid support for the heterostructure.

Therefore, to increase the sensitivity to the film signal and for avoiding the superposition of the intense substrate diffraction peaks, we used a wet transfer technique for substituting the substrate slab (surface area ca. 25 mm^2, thickness ca. 100 μm) with a Si(100) plate, whose diffraction peaks are far from those of the overlayers. For this purpose, we sputtered an amorphous C-film on the 4T film surface; then, we placed the substrate/4T-film/C-film assembly on the surface of distilled water from the substrate side. After an hours, the KAP substrate dissolved and the free insoluble 4T film covered with the C-film (which makes the film easily visible) was found floating on the water surface. We placed the films on a Si (100) plate and let them dry in a nitrogen atmosphere before data collection. The wet-transfer method is a well-established method for organic device assembly, which can be routinely used for fast and cost effective device fabrication [8, 9].The measurements have been carried out using a Cu-K_α X-ray source (λ= 1.54 Å) and the resulting diffractogram after wet transfer is shown in Figure 4-2. From the diffractogram, reflections from the (00*l*) planes up to the sixth order corresponding to a spacing of 15.23 Å were found. This

spacing matches with that of the (002) planes of the LT polymorph of 4T [10], in accordance with the known structure and orientation of these films. The presence of the (00*l)* reflections (reflections shows no odd-*l* planes, which in agreement with the symmetry of the considered system) of the LT polymorph indicate that, the crystalline domains are in contact with the substrate with the (*a b)* crystal plane, parallel to the substrate surface; therefore the molecules orient in almost upright standing position with the long axes of molecules form an angle of 24.8° to the normal of the substrate plane [11] showing herringbone pattern. In the diffractogram, a known peak of Si (200) can also be found, which is originated from the silicon substrate and can be used as a mean to check the calibration of all the observed peaks positions.

4.1.2 Optical characterization

In the case of highly oriented crystalline thin films, polarized optical spectroscopy can give significant hints about the orientation of the film crystal structure with respect to the substrate [3, 12]. In Figure 4-3, the absorption spectra of a 15 nm-thick 4T thin film grown on KAP (010) is reported, as collected at normal incidence under linearly polarized light. A strong anisotropy is observed in the spectra, indicating a preferential orientation of 4T crystalline domains, similar to that reported in reference [7, 11].

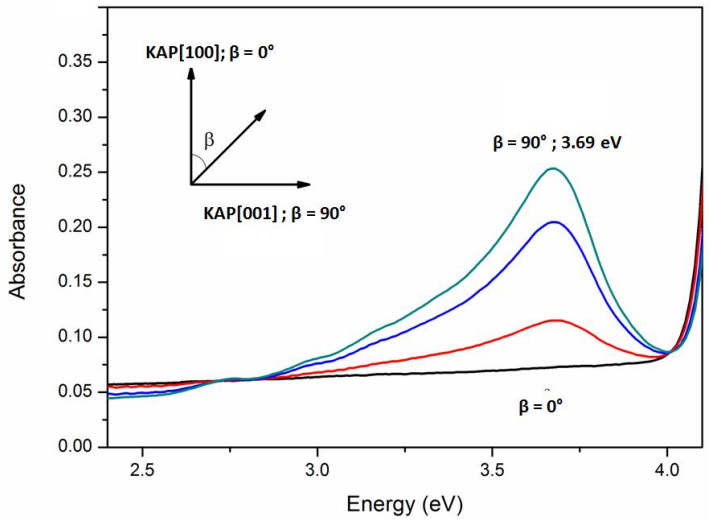

Figure 4-3 Absorbance spectra of a 15 nm-thick 4T thin film grown on KAP (010) taken at normal incidence with light linearly polarized along different directions, labeled by the angle β between the electric field vector and KAP [100].

The maximum peak intensity in Figure 4-3 was found at 3.69 eV for $\beta = 90°$, where β is the angle between the electric field vector of the light and a_{KAP}, as sketched in the inset of Figure 4-3. A similar peak position is reported in the literature as due to the *ac* polarized excitonic transition in 4T/LT, detected when impinging at normal incidence on the (001) crystal plane and is observed in both single crystals as well as thin films [2, 13].However, the spectrum collected with perpendicular polarization, i.e., with $\beta = 0°$, show a complete extinction of the peak. Maximum peak intensity at $\beta = 90°$ and a complete absence of the absorption peak in the spectrum at $\beta = 0°$ in Figure 4-3 reveal a complete film orientation, i.e. almost all the molecules contributing to the absorption spectrum are oriented in such a way that their long molecular axis projection on the substrate lies along the *c*-axis of the KAP (010) substrate.

4.1.3 AFM characterization

Local characterization of the morphology of 4T films on KAP (010) is done by TM-AFM. A typical AFM height image of 8 nm nominal thick 4T thin films on KAP is reported in the Figure 4-4.

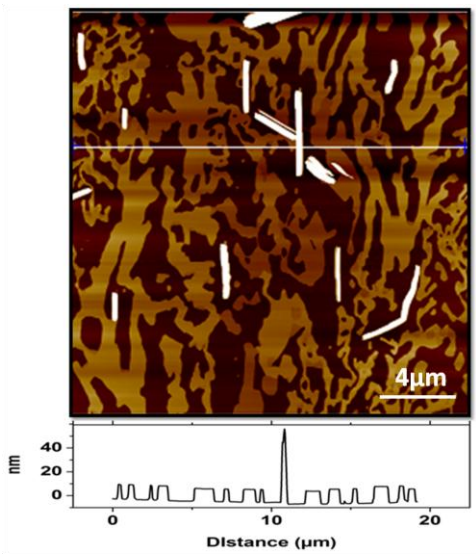

Figure 4-4 20 × 20 µm^2 AFM height image of an 8 nm thick 4T thin film on KAP (010) showing needles and islands. Below is the cross sectional signal along the white line.

The height image reveals the existence of two types of characteristic features on the substrate surface, which are flat terraces and needle like crystallites oriented in four different directions with respect to the c_{KAP}. The flat terraces contain few monolayers of 4T, which show almost the same height, close to the nominal thickness. Since the terraces cover majority of the film, the XRD reflection and the optical spectroscopy predominantly show the response from these terraces. So the results of optical and the structural studies suggest that the molecules in the flat islands stand almost in an upright position which is in agreement with the height of monolayer measured by AFM, which is 1.5 ± 0.2 nm . In the case of 8 nm nominal thick films, the needles height is 60 ± 20 nm, while the width of the needles is less than 50 nm. The typical length of the needles is ranging from 2 µm to 8 µm. The needles are observed to lie along four specific directions, forming angles of ± 5° and± 63° with respect to the c_{KAP}.

4.1.4 Results

In the case of inorganic materials, epitaxial orientation is possible only when the lattice mismatch falls within a few percent. However the situation is different in the case of organic epitaxy. In our case, for example the lattice mismatch between the substrate and the overlayer is found to be very

high. Yet our experimental results suggest that the orientational effect on 4T molecules by KAP (010) substrate is very strong and effective. The reason for this rests on the concept of coincident epitaxy, which is a more relaxed epitaxial condition holding for materials where bonding is weak, as organics [14, 15]. Coincidence between KAP (010) substrate and the 4Toverlayer is classified as line-on- line; in the line-on-line registry, non-primitive reciprocal vectors of the surface lattices of substrate and overlayer coincide. Line-on-line is found to be the most common lattice registry observed in the epitaxy of organic semiconductors [12, 16-18]. This occurs because in molecular crystals surfaces are relatively more corrugated with respect to atomic materials, and corrugations run often along non-primitive crystallographic directions [as in the case of the surface of KAP (010)]. Therefore one can say that a minimum interface energy condition between two surfaces of molecular materials is achieved by matching their directions of main corrugation.

The results of optical characterization are in total agreement with the structural information obtained from XRD measurements. A molecular model of crystalline 4T islands on the substrate is illustrated in Figure 4-5 and it corroborates the results of optical and structural studies. Figure 4-5 (b) presents the surface of KAP (010), which is corrugated in such a way that hydrogen atoms forms grooves along the $[101]_{KAP}$. When the *a* axis of 4T is parallel to the *c* axis of the substrate, the $[101]_{KAP}$ will become parallel to $[110]_{4T}$ and the molecules fit in these grooves giving rise to line-on-line epitaxy. The 4T molecules are adsorbed on these hydrogen grooves on the substrate surface, so as to have a closer contact with the substrate surface. In reference [11] it is reported that in needles, molecules orient in such a way that the *ac* plane of the unit cell is parallel to the surface of the substrate and the axes of needles are parallel to a_{4T}. The surface potential calculations of reference [11], is also in agreement with this structural model as the comparatively large electrostatic interaction between the CH dipoles of the thiophene rings and the oxygen atoms of the carboxylic groups of KAP makes the 4T molecules arrange in the discussed pattern. In other words, the surface corrugation and surface potentials are complimentary to each other, both illustrating the way molecules interact in solid state. This in turn suggests that in the case of non equilibrium processes like the growth by organic molecular beam epitaxy, surface corrugation is the most important parameter that determines the molecular orientation rather than the crystalline periodicity or the possibility to form molecular complexes.

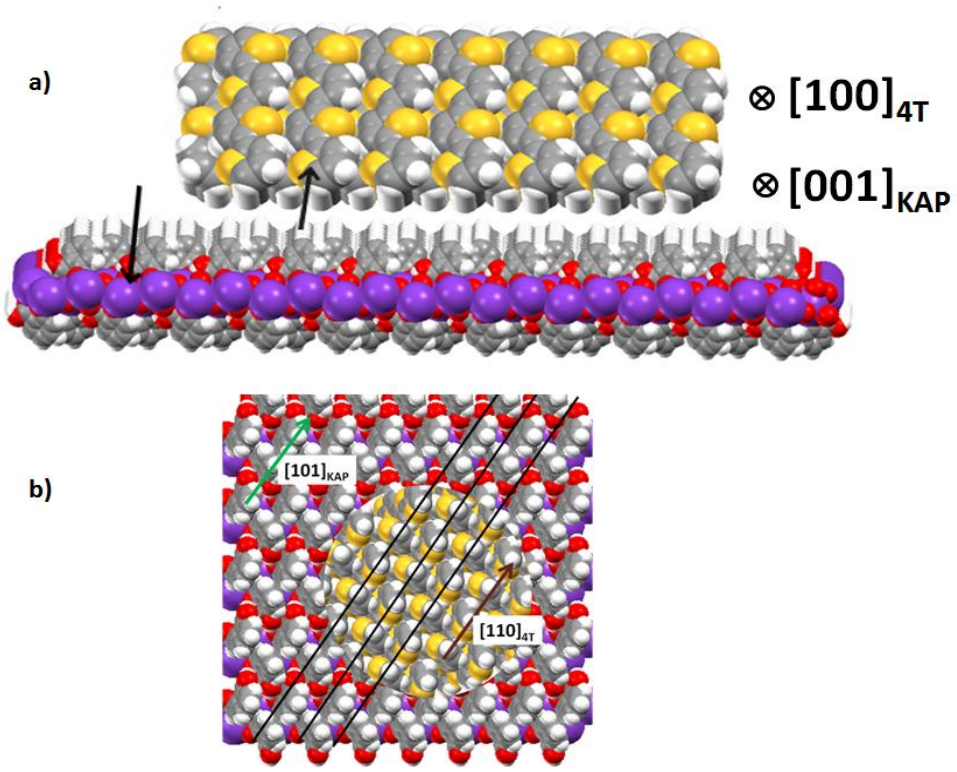

Figure 4-5 Structural model of the epitaxial interface between KAP (010) and 4T/LT (001). (a) (Side view) Under this epitaxial orientation, the main corrugations of 4T/LT and KAP, running along [100] and [001], respectively, are observed to match, giving rise to a stable interface. (b) (Top view) Line on line epitaxy between the main corrugation of KAP (010) along [101] of KAP with the <110> of 4T/LT.

4.2 α-Quaterthiophene thin films on pentaerythritol (PET) single crystal

Just like in the case of KAP (010), the PET (001) surface presents peculiar structural features that are very interesting in the context of organic epitaxy, as shown in Figure 4-6. Notwithstanding the tetragonal symmetry of the crystal, its basal surface is decorated by couples of C-atoms, uniaxially aligned along PET [110] (see Figure 4-6 (b)). This confers the (001) surface a peculiarly strong corrugation, which could in principle drive the orientation and structure of the overlying 4T thin film.

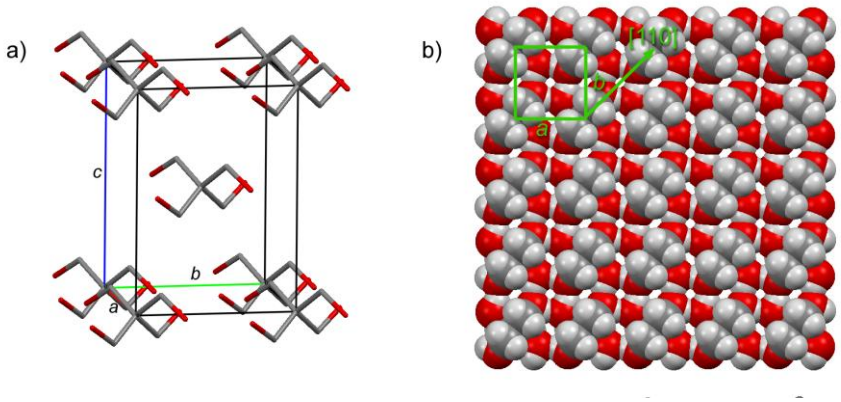

Figure 4-6 (a) Crystal structure of tetragonal PET (H-atoms omitted). (b) Caps model of the PET (001) surface. White, red, and grey caps represent H-, O-, and C-atoms, respectively.

4.2.1 Structural characterization

Figure 4-7 shows the XRD pattern of a 15 nm-thick 4T film grown at room temperature on PET, compared with that of a film grown under the same conditions on KAP. In the case of 4T grown on KAP, only reflections corresponding to (002) planes of the LT polymorph were found, while on the contrary, the peak positions in the pattern of 4T on PET suggest the presence of three polymorphs. One of them is 4T/LT, since all the peaks present in the blue pattern (4T on KAP) appear also in the red pattern (4T on PET) of Figure 4-7(b). Additionally, a series of reflections up to the fourth order, consistent with a 14.23 Å spacing, was found. This spacing matches with that of (001) planes of the HT polymorph [10]. Finally, the most intense film peaks (labeled with a star) correspond to an unknown phase (which we call pseudomorphic phase, 4T/PM), and show a position in-between those of the HT and LT phases (but closer to HT). The interlayer spacing of the corresponding lattice planes in the PM phase is 14.54 Å.

Furthermore, the red pattern shows some intensity at 22.61°, which is attributed to the (020) planes of the LT phase (and a peak at 20.27°, being a remainder of the dissolved substrate). The presence of (00*l*) reflections indicate film domains composed of layers of molecules (length ca. 1.7 nm) all parallel to one another and standing almost upright with respect to the substrate plane. In the LT phase (Figure 3-12 (c)), the molecules form an angle of 65° to the basal plane, which reduces to 58°in the HT phase (Figure 3-12 (d)),). Accordingly, the PM phase would consist of

molecules forming an angle of ca. 60° to the basal plane. On the other hand, the presence of some intensity from (0*k*0) reflections of the LT polymorph is indicative of a phase with molecules lying flat on the substrate i.e. where the *ac* plane of the 4T/LT is lying parallel to PET (001).

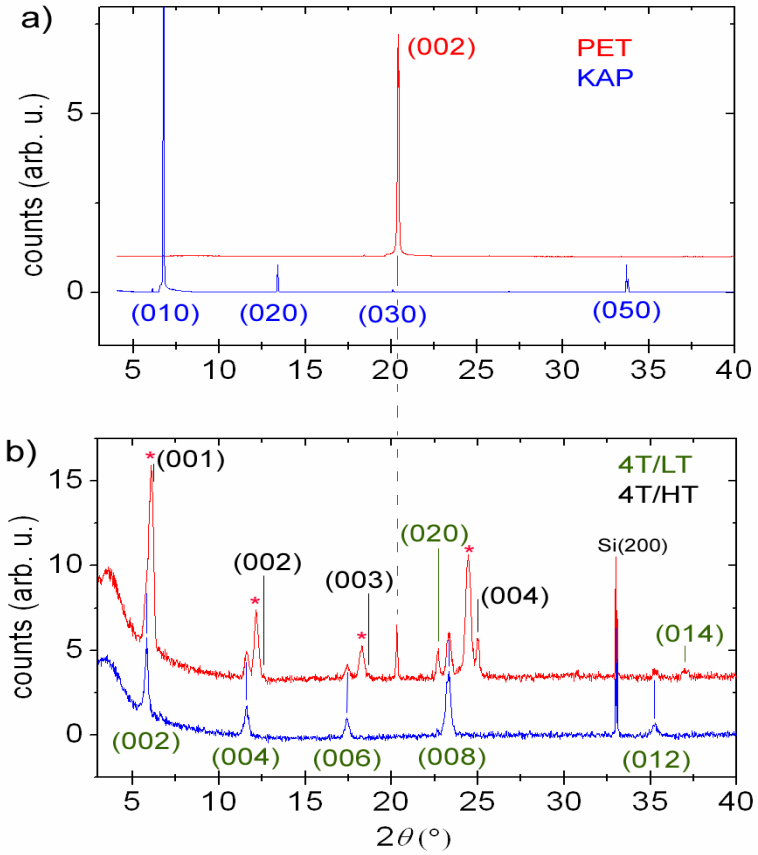

Figure 4-7 (a) XRD patterns (λ = 1.54 Å) collected on 15 nm-thick 4T films (a) XRD patterns (*λ* = 1.54 Å) collected on 15 nm-thick 4T films grown on KAP and on PET (blue and red pattern, respectively). The peak indexes refer to the substrate crystal structure. (b) XRD patterns collected on 4T films grown on KAP and on PET after wet-transfer on Si (100) plates. The peaks are indexed in accordance with the known crystal structures of the LT (green indexes) and HT (black indexes) polymorphs of 4T. The starred peaks belong to the unknown 4T polymorph.

Considering the integrated area of the XRD peaks in Figure 4-7 as proportional to the square modulus of the corresponding structure factors calculated from the single crystal structures of 4T/LT and 4T/HT, one can estimate the relative amounts of LT over HT, resulting 2:3. Assuming structure factors for the PM phase similar as those of the HT one, the ratio among LT, HT, and PM phase (the preponderant phase) can be calculated obtaining 2: 3: 12. From the XRD results,

information about the contact planes of the three polymorphs with respect to the substrate was found, as well as a new 4T phase observed.

4.2.2 Optical characterization

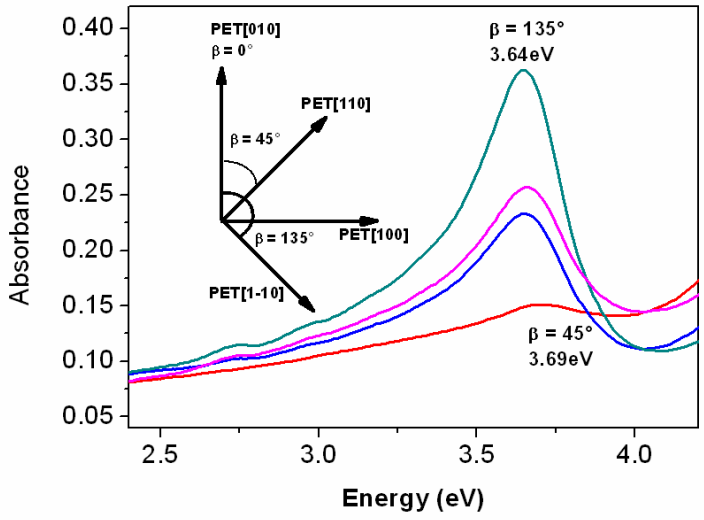

Figure 4-8 Absorbance spectra of a 15 nm-thick 4T thin film grown on PET (001) taken at normal incidence with light linearly polarized along different directions, labeled by the angle β between the electric field vector and PET[010].

For studying the in plane azimuthal orientation of the mentioned polymorphs on a macroscopic scale, polarized optical measurements were performed. Likewise in the case of 4T on KAP (see Figure 4-3), polarized optical spectroscopy gives significant hints about the orientation of the films or the film domains. The maximum peak intensity in Figure 4-8 was found at 3.64 eV for β = 135°, where β is the angle between the electric field vector of the light and b_{PET}, as sketched in the inset of Figure 4-8. The spectrum collected with perpendicular polarization, i.e., with β = 45°, does not show a complete extinction of the peak, so that the structure alignment should be only partial, contrary to Figure 4-3 which shows a complete extinction. In addition, in the 45° spectrum the main peak is shifted towards higher energy, at about 3.69 eV. This peak position perfectly matches the *ac* polarized excitonic transition in 4T/LT, similar to that seen on 4T on KAP.

On the other hand, for 4T/HT the main absorption peak is at about 3.64 eV or slightly above, as deduced from reflectance measurements reported in the literature [13]. Reflectance spectra of a single crystal before and after the phase transition from the LT to the HT polymorph show that the main peak in HT and LT polymorphs is found at 3.76 eV and 3.81 eV, respectively. Considering a shift of 0.12 eV, that has been observed between reflectance and absorption spectra in the LT polymorph [13], we deduced that in the HT crystal the main peak in absorption should be at about 3.64 eV (or slightly above, considering that the shift could be smaller, being the peaks at lower energy). In the absorption spectra in Figure 4-8, the observed position of the main peak when it displays maximum intensity is indeed at 3.64 eV. This is in full agreement with the estimated value for the main peak of the HT polymorph.

4.2.3 AFM characterization

In order to get a microscopic description of the samples along with the macroscopic one deduced from optical spectroscopy, the surface morphology of the 4T films deposited on PET(001) was studied by AFM and the results are summarized in Figure 4-9. The morphology indicates the presence of a wetting phase of flat islands with a regular layered structure (terraces), and some needle-shaped 3D crystals. The island thickness is close to the film nominal thickness (ca. 10 nm), while the needle height is of the order of 100 nm. The measured interlayer spacing in the islands is 1.4 ± 0.17 nm (see Figure 4-9(d)), consistent with (00l)-oriented domains, i.e., with molecules in an upright standing position with (*a b)* plane of 4T/HT parallel to PET (001). This phase is therefore the one responsible for the detection of (00*l*) peaks in Figure 4-7 (as a consequence, (0*k*0) peaks in XRD must be attributed to the needles). As shown in Figure 4-9 (c), the terraces display a lozenge shape, which is typical to the growth of 4T, where the *a*-axis of 4T align orthogonally to PET [110]. The needles are observed to be in four specific directions, forming angles of ± 20° (with an error of 2°) and very few ones forming 0° with respect to the PET *a*-axis.

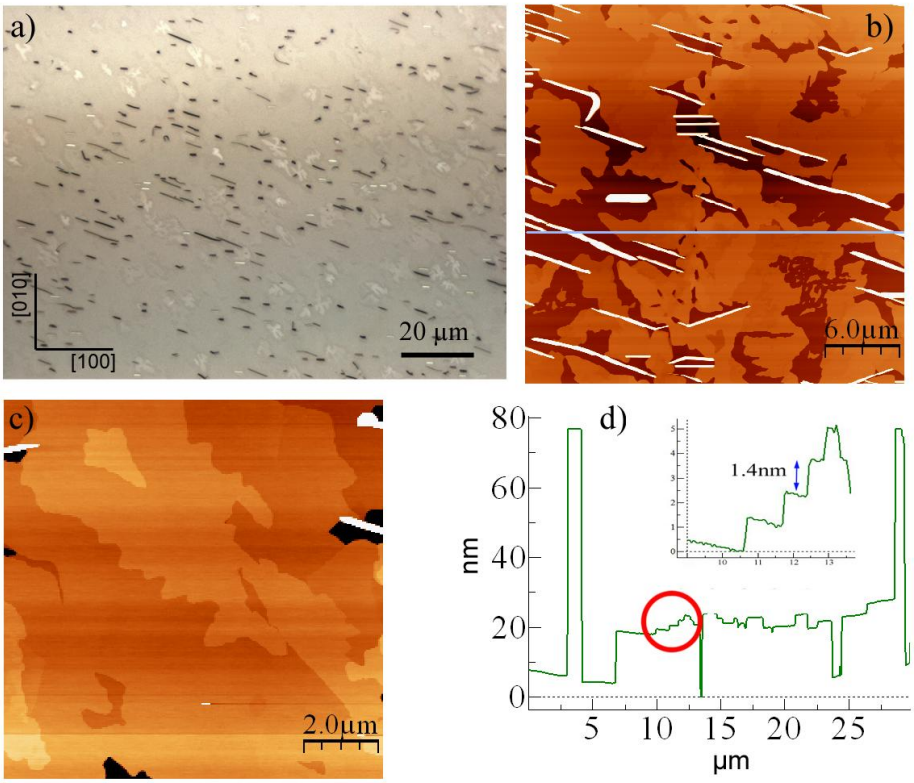

Figure 4-9 (a) Optical micrograph of a 8 nm-thick 4T film deposited on PET(001). (b) The 30 × 30 μm^2 AFM image showing both the flat islands and the needles. (c) The 10 × 10 μm^2 AFM image showing the lozenge shape of fully formed terraces. (d) Cross-sectional profile as taken along the blue horizontal line in (b). Inset: zoomed profile (inside the red circle) showing the layered film structure. The orientation of the PET substrate indicated at the bottom-left corner of panel (a) holds for all panels.

4.2.4 Results

At first structural model of 4T islands is proposed. In absorption spectra, the peaks corresponds to the 4T islands as the light is scattered off from the needles because of their thinner dimensions. In the absorption spectra we did not observe separate peaks for HT and PM phases. Therefore, it has been considered that the preponderant PM phase have almost the same optical response as the HT phase. For discussing the epitaxial relation between 4T and PET, we start by considering the 4T structure as belonging to the HT polymorph, then, we will use the conclusions to get some more information on the new PM phase. When looking at the polarization angle giving maximum intensity in Figure 4-8, a preferential alignment of the 4T film structure with respect to the PET

substrate can be deduced: the [010] direction of the 4T/HT structure align parallel to the [110] direction of PET(001). This configuration corresponds to a unit cell oriented with 4T/HT [100] // PET [110] and the 4T molecules almost standing upright (see Figure 4-10). This preferred orientation is readily explained, since it brings to the alignment of the main corrugation of the PET surface (enclosed between (110) planes) with that of 4T/HT (enclosed between (200) planes. The matching requires a misfit below 4% (d_{110} = 4.31 Å and d_{200} = 4.47 Å, respectively, Figure 4-10). This lattice coincidence between substrate and overlayer is classified as line-on-line, as explained in the case of 4T on KAP (010).

In the 4T/HT (001) // PET (001) interface, the coincident planes that give rise to line-on-line epitaxy are 4T/HT (200) and PET (110) as shown in Figure 4-10 (a). From a combination of XRD data and epitaxial arguments, we can infer some structural features of the new PM phase of 4T, then justifying its selection by the PET (001) substrate. If we compare the two known polymorphs of 4T, we realize that some relevant structural features are common to both of them: (i) all molecules parallel to one another (Figure 3-12), (ii) layered arrangement, (iii) herringbone motif and (iv) same volume per elemental molecular monolayer (730 $Å^3$). Starting from this last condition (iv), we assume it to be characteristic of the mutual interactions between the neighboring 4T molecules and therefore to be valid for the PM phase also. Hence, for an interlayer spacing of 14.54 Å, deduced from XRD as the one of the PM polymorph, a unit cell basal surface of 50.2 $Å^2$ is inferred (to be compared with 51.4 Å for HT and 47.9 Å for LT). Due to the dominance of the new PM phase, we can assume it to have a surface lattice allowing for a total compensation of the residual 4% lattice misfit given by the HT phase with the substrate. As a consequence, we can guess the PM phase to have a spacing of its main corrugation (d_{200}) matching that of PET (001) (d_{110} = 4.31 Å). Following this we can deduce the following surface cell parameters for the new PM polymorph: a = 4.31 Å × 2 = 8.62 Å and b = 5.83 Å.

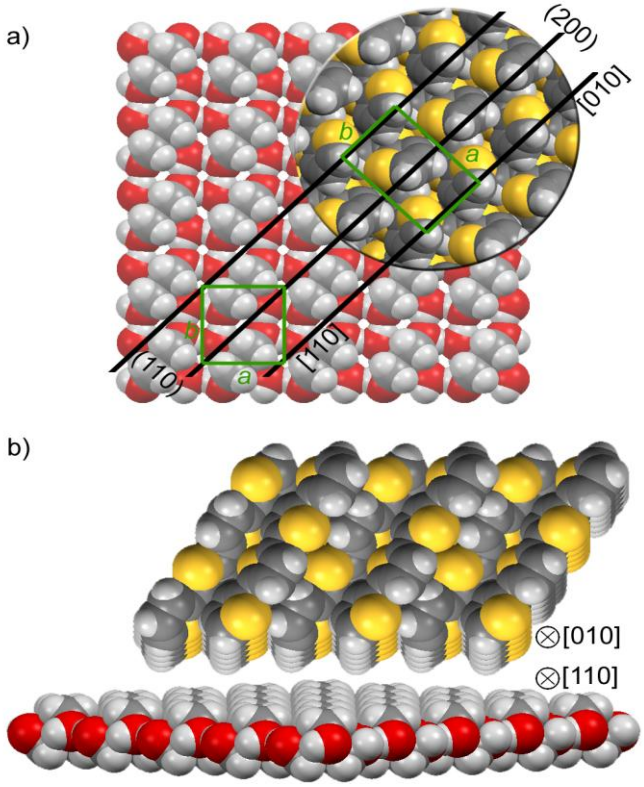

Figure 4-10 Structural model of the epitaxial interface between PET (001) and 4T/HT (001). (a) (Top view) The spacing among (110) planes of PET (bottom left) highlighted by black lines is observed to equal that among (200) planes of 4T/HT (top-right) when the epitaxial relation 4T/HT [010]//PET [110] is fulfilled. (b) (Side view) Under this epitaxial orientation, the main corrugations of 4T/HT and PET, running along [010] and [110], respectively, are observed to match, giving rise to a stable interface.

Back to the optical spectra of Figure 4-8, the non-negligible intensity observed for β = 45° and the spectral shift of the corresponding peak up to 3.69 eV corroborate the existence of a small portion of the 4T/LT polymorph which, in addition, possesses a peculiar, but different alignment with respect to the PET substrate. The *a*-axis of the 4T/LT unit cell is exactly the same as the *a*-axis of PET. This favors the presence of two orthogonal orientations for 4T/LT through the epitaxial coincidences 4T/LT [100] // PET [100] and 4T/LT [100] //PET [010].

The relative amounts of LT and HT+PM phases not distinguishable in films on PET can be deduced approximately also from absorption spectra. To do this, the absorbance of two 4T films grown contemporarily on PET and on KAP, therefore with exactly the same thickness, is compared. Keeping in mind the two orthogonal orientations of the LT polymorph on PET, we can to compare the intensity of the absorption peak of 4T/KAP, when the *a*-axis of 4T makes an angle of 45° with respect to the polarization plane, with the minimum peak intensity at β = 45° of 4T/PET, both consistent with an *ac* polarized transition of the LT phase (β = 45° the absorption peak does not possess the component from HT phase because of its unique orientation with respect to the substrate). In this way, a ratio 1:6 is found between the LT response in the two films, which corresponds approximately to the ratio between LT and HT+PM polymorphs in the film on PET (001). Considering the uncertainty of such evaluation, this ratio very well matches the 1:7.5 ratio between LT and HT+PM calculated from XRD results (see section 4.2.1), demonstrating the full consistency of our structural and optical data.

Finally the epitaxial relation between the needles and the substrate can also be deduced. The needle-like crystallites, observed in Figure 4-9 (a) and Figure 4-9 (b), display a well-defined preferential direction. In the needles, the {020} planes of 4T align parallel to PET (001). Looking at the model for the surface structure of PET (001) (Figure 4-6(b)), and following recent arguments developed for organic epitaxy [11, 12], we heuristically assume that the 4T molecules would find a favorable orientation when aligned parallel to [110]-oriented rows formed by prominent H-atoms of the PET (001) surface (Figure 6(a)).

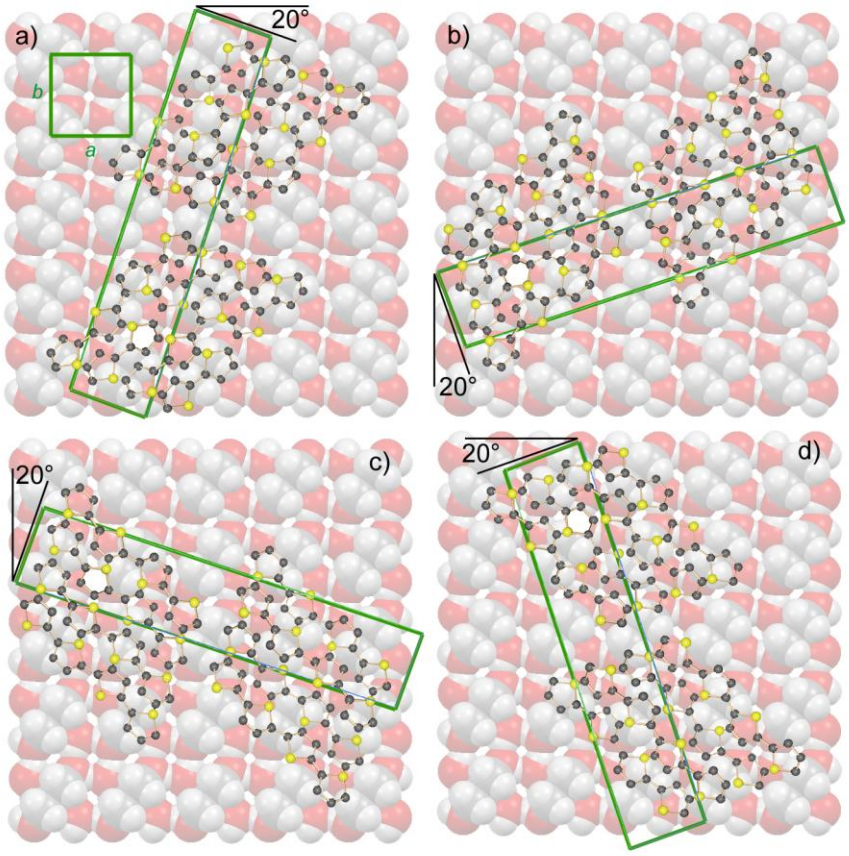

Figure 4-11 Epitaxial orientation of 4T/LT needle-like crystals (elongated parallel to the short axis of the cell) resulting from the alignment of the molecular axes parallel ((a) and (b)) and orthogonal ((c) and (d)) to the H-atoms rows of the PET(001) surface. The 4T contact plane is (0 $\bar{2}$ 0) in (a) and (c) and (0 2 0) in (b) and (d).

In this arrangement, the needles of the 4T/LT phase, elongated parallel to the *a*-axis (short axis), would form an angle of –20° with respect to PET *a*-axis, corresponding to the interface 4T(0 $\bar{2}$ 0)//PET(001) (the same angle would be –13° molecules were to orient as HT phase in needles). The angle between the PET *a*-axis and the needles was experimentally found to be –20 ± 2°. This clearly demonstrates the attribution of the LT polymorph to needle-like crystallites and that their preferential alignment is driven by the collinear arrangement of 4T molecules and rows of H-atoms on the PET surface. However, from optical and AFM images, one can realize the presence of a non-negligible population of needles oriented at +20° with

respect to the PET *a*-axis. In order to give rise to this orientation in needles, the alignment of 4T molecules must be orthogonal to the rows of H-atoms of the PET surface, when contacting the substrate with the (020) plane (Figure 4-11(d)). Surprisingly, the orthogonal alignment of 4T molecules with respect to the hydrogen rows, are not selected when the contact plane is (0$\bar{2}$0) (Figure 4-11(c)). Similarly the orientation of the 4T cell symmetrically equivalent to Figure 4-11 (a) is selected with 4T (0 $\bar{2}$ 0) // PET (001), while (Figure 4-11(b)) is not selected. These findings may be explained by a possible surface reconstruction and kinetics during the film growth of PET (001), giving rise to a reduction of its symmetry. Sporadic needle orientation at 0° to the PET *a*-axis is also observed (Figure 4-9(b)). This may derive from the almost perfect match between the 4T/LT *a*-axis and the surface parameter of PET (001). However, in this case, two orthogonal orientations would be expected, i.e., 4T/LT [100] // PET [100] and 4T/LT [100] // PET [010]. In fact, the selection of only one of these arrangements is observed experimentally, probably due to the same surface reconstruction leading to a dominant orientation of needles at –20°.

4.3 Conclusions

4T thin films were grown by using OMBE on two different substrates, namely KAP and PET. Substrate driven selection of crystal structure in epitaxial thin films of 4T has been studied and discussed. The growth of 4T thin films on various organic single crystal substrates, such as KAP, sexithiophene, tetracene, rubrene, etc., has shown the presence of either the LT phase or pseudomorphic phases very close to the LT one.[3, 16, 19]. This study demonstrates that epitaxial 4T films can be grown also on single crystal PET, where a pseudomorphic phase very close to the HT polymorph is found to be the dominant film phase. The possible epitaxial relations between the lattice of substrate and overlayer are deduced. This is the first time that a polymorph close to the high temperature phase of 4T is found in thin films grown at room temperature. The 4T/HT, due to its better conductivity predicted, is considered as the most promising polymorph of 4T for applications in organic devices [20]. The similarity in the microscopic properties of the PM and the HT phase, as inferred from our results, suggests in principle that the newly formed PM phase can also be exploited for making high quality organic devices. Moreover, the solubility of PET enables the use of cost-effective wet-transfer methods, particularly useful also for device processing. These results clearly show how the mechanisms of organic epitaxy can be exploited

not only to drive the orientation of the overlayer in its thermodynamically stable phase, but also to induce the growth of new and different oriented phases with useful physical properties.

4.4 References

1. Fichou, D., *Structural order in conjugated oligothiophenes and its implications on opto-electronic devices.* Journal of Materials Chemistry, 2000. **10**(3): p. 571-588.
2. Sassella, A., et al., *Crystal structure of polycrystalline films of quaterthiophene grown by organic molecular beam deposition.* Synthetic Metals, 2003. **138**(1–2): p. 125-130.
3. Sassella, A., et al., *Pseudomorphic growth of organic semiconductor thin films driven by incommensurate epitaxy.* Applied Physics Letters, 2009. **94**(7): p. -.
4. Sassella, A., et al., *Tuning the growth mode in organic molecular-beam epitaxy.* Physical Review B, 2005. **71**(20): p. 201311.
5. Bonafede, S.J. and M.D. Ward, *Selective Nucleation and Growth of an Organic Polymorph by Ledge-Directed Epitaxy on a Molecular Crystal Substrate.* Journal of the American Chemical Society, 1995. **117**(30): p. 7853-7861.
6. Schlenker, C.W., et al., *Cascade Organic Solar Cells.* Chemistry of Materials, 2011. **23**(18): p. 4132-4140.
7. Sassella, A., et al., *Optical properties of highly oriented quaterthiophene thin films grown by organic molecular-beam deposition.* Physical Review B, 2000. **62**(16): p. 11170-11176.
8. Noh, Y.Y., et al., *Effect of Molecular Orientation of Epitaxially Grown Platinum(II) Octaethyl Porphyrin Films on the Performance of Field-Effect Transistors.* Advanced Materials, 2003. **15**(9): p. 699-702.
9. Yanagi, H., T. Morikawa, and S. Hotta, *Electroluminescence from low-dimensionally confined crystals of thiophene/p-phenylene co-oligomers.* Applied Physics Letters, 2002. **81**(8): p. 1512-1514.
10. Siegrist, T., et al., *Crystal Growth, Structure, and Electronic Band Structure of α-4T Polymorphs.* Advanced Materials, 1998. **10**(5): p. 379-382.
11. Campione, M., et al., *Organic−Organic Epitaxy of Incommensurate Systems: Quaterthiophene on Potassium Hydrogen Phthalate Single Crystals.* Journal of the American Chemical Society, 2006. **128**(41): p. 13378-13387.
12. Raimondo, L., et al., *Unique Orientation of Organic Epitaxial Thin Films: The Role of Intermolecular Interactions at the Interface and Surface Symmetry.* The Journal of Physical Chemistry C, 2011. **115**(13): p. 5880-5885.
13. Laicini, M., et al., *Microscopic calculation of dielectric tensor of quaterthiophene crystals.* Physical Review B, 2005. **71**(4): p. 045212.
14. Hooks, D.E., T. Fritz, and M.D. Ward, *Epitaxy and Molecular Organization on Solid Substrates.* Advanced Materials, 2001. **13**(4): p. 227-241.
15. Mannsfeld, S.C.B. and T. Fritz, *Understanding organic–inorganic heteroepitaxial growth of molecules on crystalline substrates: Experiment and theory.* Physical Review B, 2005. **71**(23): p. 235405.
16. Campione, M., et al., *Organic−Organic Heteroepitaxy of Semiconductor Crystals: α-Quaterthiophene on Rubrene.* Chemistry of Materials, 2009. **21**(20): p. 4859-4867.

17. Campione, M., *Rubrene Heteroepitaxial Nanostructures With Unique Orientation.* The Journal of Physical Chemistry C, 2008. **112**(42): p. 16178-16181.
18. Campione, M., et al., *Control of π−π Interactions in Epitaxial Films of Platinum(II) Octaethyl Porphyrin†.* Chemistry of Materials, 2010. **23**(3): p. 832-840.
19. Sassella, A., et al., *Epitaxial growth of organic heterostructures: Morphology, structure, and growth mode.* Surface Science, 2007. **601**(13): p. 2571-2575.
20. Sassella, A., et al., *Probing phase transitions and stability of organic semiconductor single crystals by dielectric investigation.* Journal of Applied Physics, 2011. **109**(1).

Chapter 5

5 Nanoscale study of electrical properties of organic thin films by using conductive atomic force microscopy

In this chapter, nanoscale morphological and electrical properties of 6T thin films grown by OMBE are studied by using AFM and C-AFM, respectively. Here, C-AFM is employed in different configurations to investigate the nature of charge transport mechanisms through organic semiconductor thin films. The results on nanoscale electrical properties of 6T thin films are then compared with the electrical properties of a polymer, P3HT.

5.1 Structural and morphological studies of 6T thin films on ITO and glass

X- ray diffraction measurements are performed (*θ/2θ* mode) at room temperature on 40 nm thick 6T films, deposited on glass and ITO substrates using OMBE. The diffraction patterns are reported in Figure 5-1 (a) and (b) respectively for 6T deposited on glass and ITO, respectively. The crystalline phase with standing upright molecules of 6T forming the low temperature polymorph (6T/LT) is discernible through the presence of (*h00*) reflections on both the substrates, consistent with an inter layer spacing (d_{200}) of 22.35 Å [3]. The crystal structure of 6T/LT belongs to the monoclinic space group $P2_1/n$ with unit cell parameters a = 44.708 Å, b = 7.851 Å, c = 6.029 Å, β = 90.76 Å, and four molecules per unit cell. The molecules are stacked nearly parallel to the long axis of the unit cell, leading to a classical herringbone structure with (*b c)* crystal face as the contact plane with the substrate (see Figure 3- 14 (a)) [3-5].

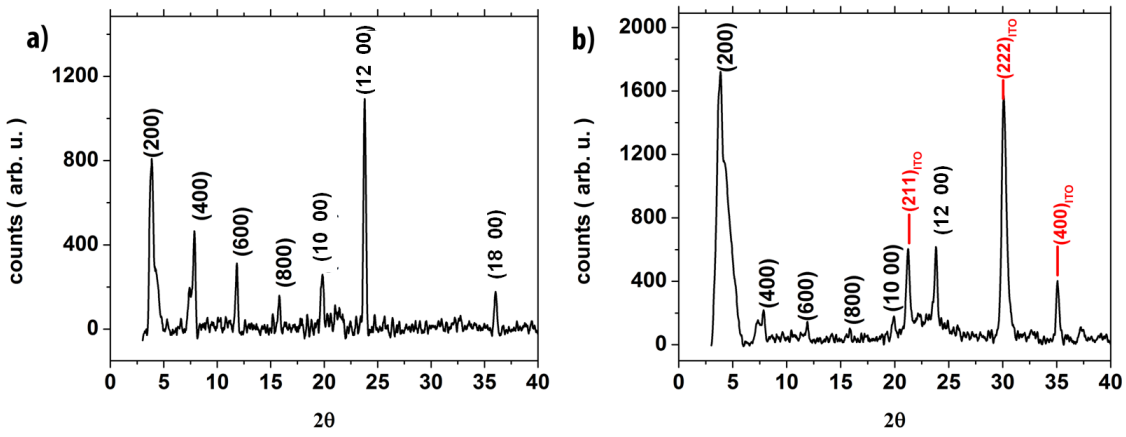

Figure 5-1 X-ray diffractogram collected in *θ-2θ* geometry with a Cu-K_α X-ray source, from vacuum evaporated 6T thin films grown on top of (a) glass and (b) ITO. The (*h00*) peaks of 6T/LT are marked in black in (a) and (b) The peaks marked in red come from ITO [2].

To get some insights about the local organization of 6T films grown on both glass and ITO, optical and AFM images were collected. A 50 × 50 μm^2 optical image and 25 × 25 μm^2 AFM height image of a 15 nm thick 6T film deposited on glass are shown in Figure 5-2, (a) and (b) respectively. From both optical and AFM images, two types of morphologies can be observed; predominantly a background matrix of 6T grains (region 1 in Figure 5-2) and dendritic structured islands (region 2 of Figure 5-2). The dendritic islands grow randomly with different micro scale sizes (ranging from 1μm to 25 μm in length, along the long axis of the dendritic islands). AFM scan on 6T films with different thickness revealed that the dendritic islands are visible on very thin films (less than 20 nm thickness), while they are absent in thicker films; by increasing thickness, the background grains possibly grow on top of the dendritic islands.

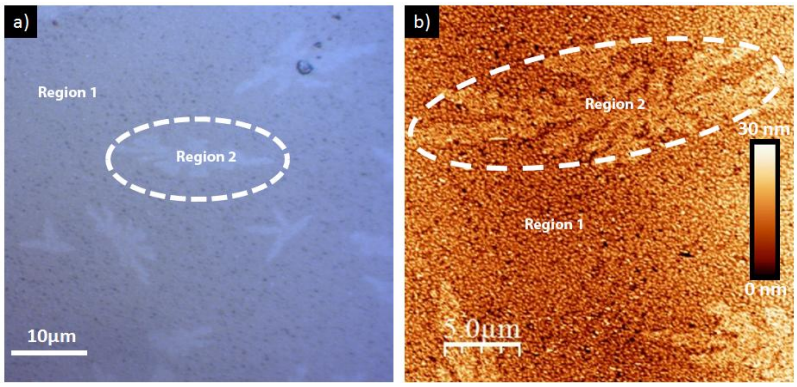

Figure 5-2 (a) 50 × 50 µm^2 optical image of a 15 nm thick 6T film on glass. (b) AFM height image of 25 × 25 µm^2 area of a 15 nm 6T film on glass showing background grains and dendritic islands.

AFM scans over smaller regions are performed by scanning a 2.5 × 2.5 µm^2 area in region 1, finding two types of self organized domains (see Figure 5-3): three dimensional pyramidal domains and elongated needle like crystallites. To better understand how these two self organized domains evolve during early growth stages, AFM scans were performed on samples with different thickness, starting from very thin samples.

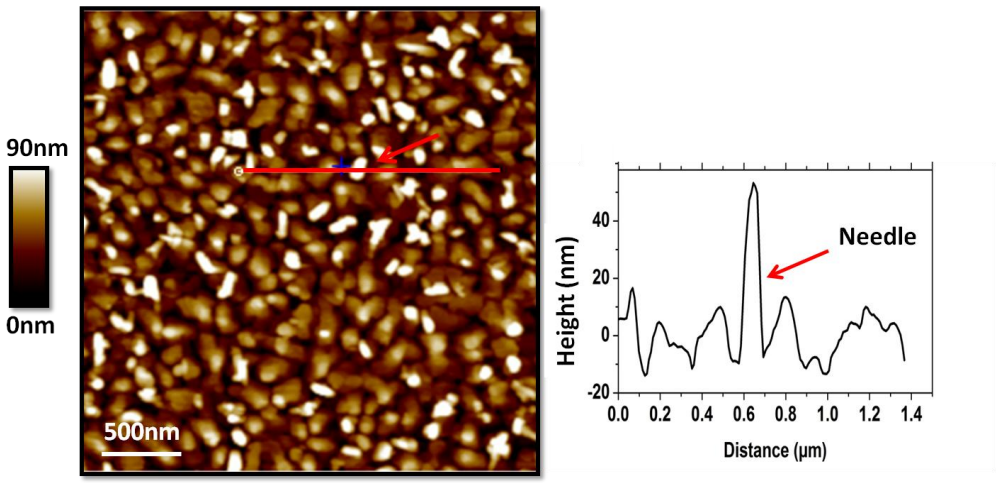

Figure 5-3 (a) 2.5 × 2.5 µm^2 AFM height image of a 15 nm nominal thick 6T thin film on glass in region 1 (comprises of pyramidal islands and needle like crystallites). (b) Cross sectional height signal along the red line on (a).

Figure 5-4 shows a sequence of AFM height images of 6T films on glass with increasing thickness. This type of growth is reported to be diffusion mediated thin film growth [6] described by the following steps. First, monomers diffuse on an almost bare substrate, eventually a stable nucleus is formed when a critical number of monomers join together (Figure 5-4 (a)). In the next step, adsorbates nucleate new islands, and they start to aggregate into existing ones (Figure 5-4 (b). Finally, some small islands coalesce to form large grains (Figure 5-4 (b) & (c)). The process strongly depends on the growth conditions (deposition rate, substrate roughness etc)).The r.ms roughness of the film (R_q) is labeled on the AFM height images in Figure 5-4 and as might be expected, the r.m.s roughness increased with the thickness of the film.

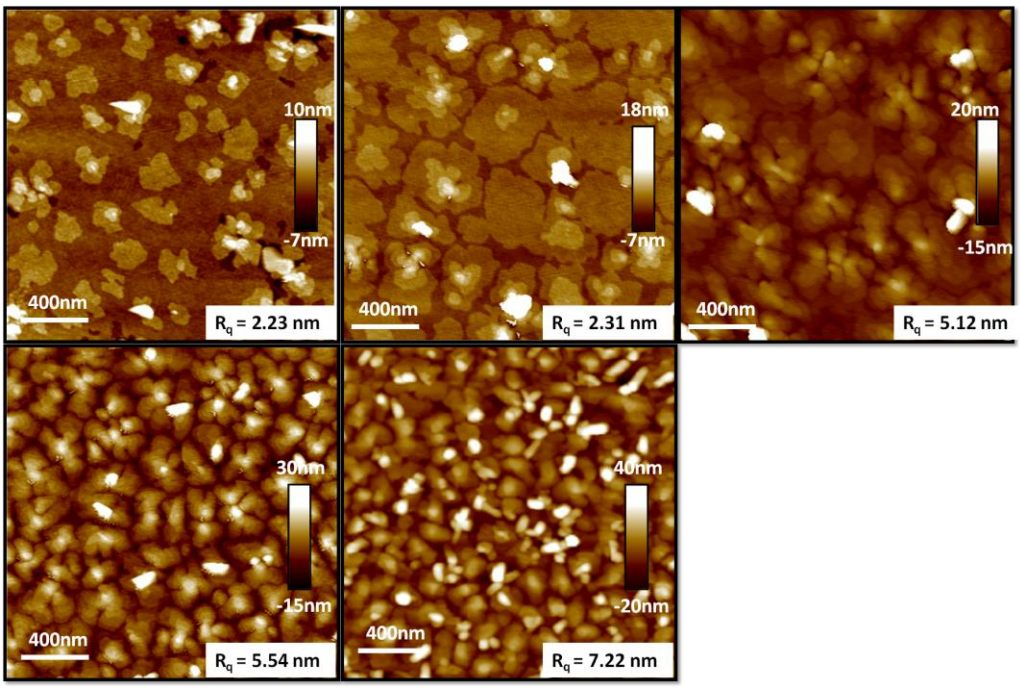

Figure 5-4 Sequence of AFM height image of 6T thin film with increasing nominal thickness on glass substrate (a) 5 nm (b) 8 nm (c) 10 nm (d) 15 nm (e) 25 nm. The r.m.s roughness (R_q) is labeled on the images.

From Figure 5-4, it is possible to identify the manner in which 3D pyramidal islands are grown. Each island is formed of an array of monolayer terraces of 6T nucleated one over another (from here on 'terraced islands'). A typical monolayer at the base of the island has a diameter of

450 ± 30 nm and height of an island is roughly equal to the thickness of the film. A magnified AFM scan on terraced islands is shown in Figure 5-5 (a) over a 1.2 × 1.2 μm^2 region. The cross section signal of Figure 5-5 (b) reveals the step height to be 2.4 ± 0.1 nm, which matches with the $d_{(200)}$ spacing of 6T/LT unit cell (Figure 3-14) [7, 8]. This implies that 6T molecules prevalently

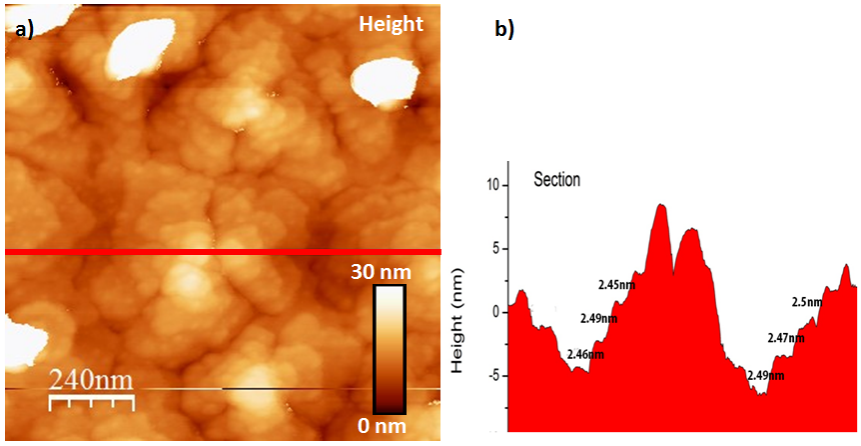

Figure 5-5 (a) 1.2 × 1.2 μm^2 AFM height image showing monolayer terraces of 10 nm thick 6T film on glass. (b) Section along the red line on (a) showing step height of 2.4 ± 0.1 nm.

orient with the long axis nearly perpendicular to the substrate surface and the crystals are grown with their (*b c)* plane parallel to the substrate [4, 9]; this is in agreement with previous observations on 6T thin films grown on relatively inert surfaces, such as SiO_2 or KBr [10, 11]. Loi et al. [7] have extensively studied such monolayer 6T terraces deposited on smooth substrate like SiO_2, reported single crystalline orientation inside the monolayers. However, the amorphous glass substrates offer relatively higher surface roughness when compared Si/SiO_2 substrates (Si/SiO_2 substrate has r.m.s roughness of 0.2-0.3nm [7], while the measured r.m.s roughness of glass is 1.2 nm). The roughness of the substrate is likely to play a role in the self organization of molecules inside the monolayer terraces on glass. From the height image shown in Figure 5-6 (a), the monolayer island appears to be rather flat. In order to investigate the effect of substrate roughness on the self organization of molecules in monolayer terraces, we used AFM in phase imaging mode. Phase imaging (see section 3.2.1) is a powerful tool for mapping small variations in sample properties that may not be evident from height images, at very high resolution. From the phase image Figure 5-6 (b), we observed sub contrast within each monolayer islands.

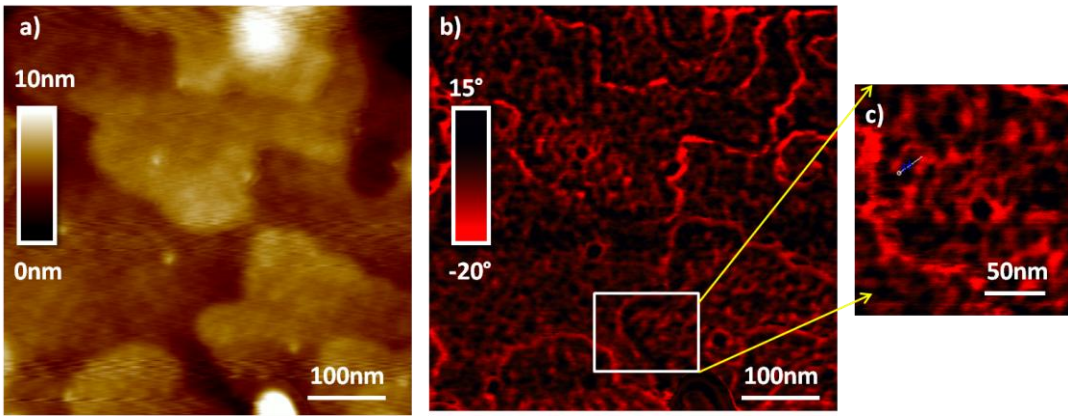

Figure 5-6 (a) AFM height image of an 8 nm thick 6T film showing monolayer terraces. (b) Phase image of (a) showing nano crystalline substructures within the terraces; (c) zoomed phase image.

The sub contrast in phase image is roughly circular, with diameter of 25 ± 5 nm, and indicates the existence of crystalline sub domains (made of standing molecules) within the monolayer islands. This will bring additional grain boundary resistance within each monolayer island, a bad scenario in view of devices. The effect of such grain boundaries on local electrical conductivity will be discussed in the later part of this chapter. Such polycrystallinity can be seen as a direct consequence of the roughness of amorphous substrates, as the molecules could crystallize only over a short range, there by forming nano crystalline domains (such sub domains are not reported on Si/SiO_2).

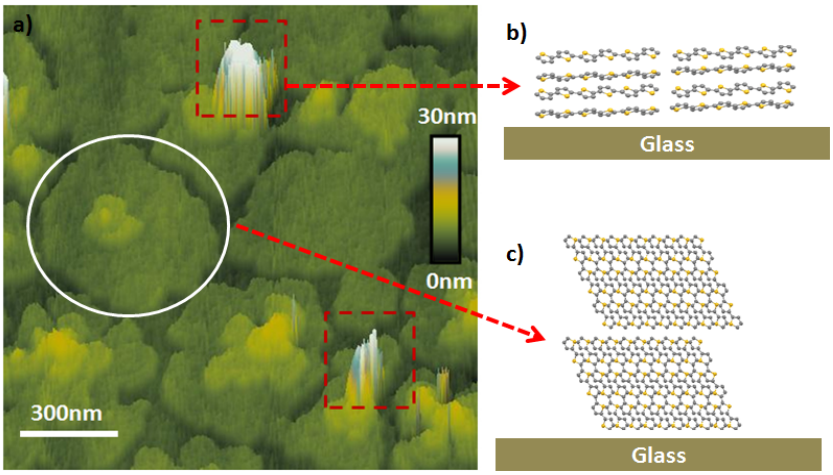

Figure 5-7 (a) Three dimensional AFM height image of an 8 nm thick 6T film on glass. (b) Lying orientation of 6T molecules in needles. (c) Vertically standing terrace orientation of molecules in the three dimensional domains.

The terraced islands can progressively incorporate flat-lying molecules to form needle like crystallites [12] (see Figure 5-7 (a)) during the evolution of the growth process. In needles, (*a c*) plane of the 6T unit cell is parallel with the substrate surface [12] (see Figure 5-7 (b)). Height of the needles are approximately three times that of terraced grains as shown in Figure 5-3 (b) (in 15 nm thick films, typical needle has a height of 50 ± 20 nm), whereas the width is of the order of the tip diameter (typically 20-30 nm). The 6T needles do not exhibit terraces, like in the case of terraced grains. From a large number of AFM height images inspected, the needles seems to grow on top of three dimensional domains, not in direct contact with the bare substrate. The needles nucleate on the step edges of the monolayer terraces (see Figure 5-7 (a) marked in red). As the needles grow on top of the terraced islands, such structures are not favorable for device applications like transistors and diodes, as the connection to the electrode will be limited and the circuit will offer very high resistance due to the presence of added grain boundaries.

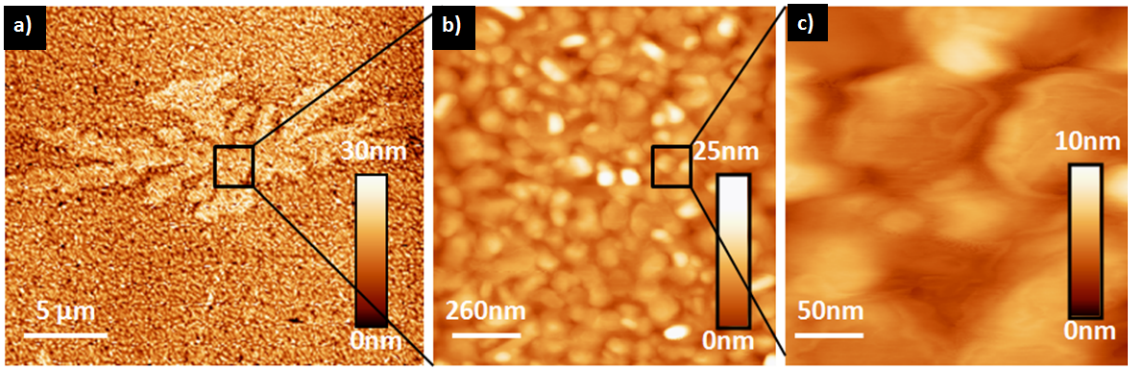

Figure 5-8 (a) 25 × 20 µm^2 AFM height image of 15 nm 6T thin film on glass showing dendritic island, (b) and (c) 1.3 × 1.3 µm^2 and 0.25 × 0.25 µm^2 magnified images of grains in dendritic island area respectively.

Figure 5-8 shows the topographic image of dendritic island of region 2 (see Figure 5-2) on a 15 nm thick 6T film. Generally dendritic islands occur during epitaxial growth in systems where island edge diffusion is restricted [13]. Albonetti et al. [14] reported that the shape of 6T monolayer islands changes from round shape to dendritic with different properties of the substrate. They have reported the presence of dendritic islands when deposited on the native Si/SiO_x substrate with less resistivity, while on native Si/SiO_x substrates with higher resistivity, 6T islands were observed to be round shaped and smaller in size compared to the others [14]. In the present case, the amorphous glass substrate might possess numerous local surface defects when compared to the native Si/SiO_x substrate. The incoming molecules can be immobilized at the local surface defects on the glass surface, resulting in a nucleation governed by surface defects, affects the crystallinity of the film. As a hypothesis, we propose such immobilization of molecules, due to the presence of local defects on the substrate, which can lead the formation of dendritic islands (see Figure 5-8 (a)), while on smooth areas of the substrate round terraced grains (see Figure 5-7 (a)) are observed, similar to that reported in [14]. The granular grains inside the dendritic islands exhibit no terraces (with a diameter of 100 ± 10 nm) indicating amorphous grains. The presence of such islands has been shown to cause transport limitations in device applications [15].

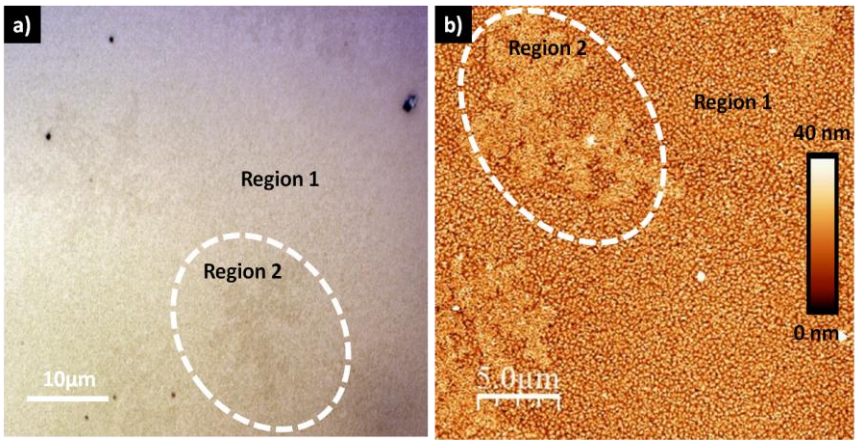

Figure 5-9 (a) 50 × 50 µm^2 optical micrograph of a 15 nm 6T film on ITO. (b) AFM height image of 25 × 25 µm^2 area of 6T thin film on ITO.

Organic semiconductor/ITO interface is of great interest for device applications. ITO surface offers relatively higher roughness compared to glass substrate (see Figure 3-15). 6T thin film deposited on ITO exhibits different types of morphologies. A 50 × 50 µm^2 optical micrograph and 25 × 25µm^2 area AFM height image of a 15 nm nominal thick 6T thin film on ITO are shown in Figure 5-9 (a) and (b), respectively. Both microscopy measurements indicate similar types of morphology as those previously observed; a background matrix of 6T 3D grains (region 1) and dendritic 6T islands (region 2).

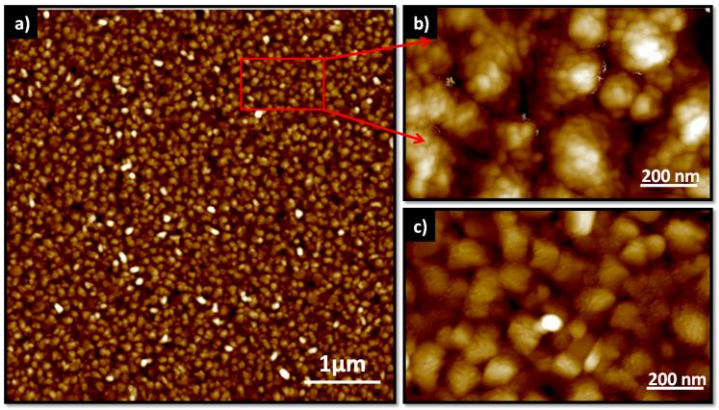

Figure 5-10 (a) 5 × 5 µm^2 AFM height image of 15nm thick 6T film on ITO. (b) Magnified scan of (a) (1 × 0.5 µm^2 area) showing back ground grains and the substructure inside it. (c) 1 × 0.5 µm^2 area AFM height image showing grains in the dendritic island.

To get better insight about the morphology of grains, smaller size AFM scans were performed. The topography of the background 3D grains in region 1 of 15 nm thick film are shown in Figure 5-10 (a). A magnified scan on Figure 5-10 (a) indicates that the self organization of molecules in 3D grains on ITO (see Figure 5-10(b)) is different from that previously observed on glass. While grains on glass substrate exhibit monolayer terraces, grains on ITO do not exhibit such terraced organization, suggests that the relatively higher roughness of the ITO surface (Figure 3-15) hinders the diffusion and aggregation of sexithiophene into terraced grains. The dimension of these 3D grains are 220 ± 20 nm in diameter, as seen in Figure 5-10 (b). The individual grains are made of small granular substructures of 35 ± 5 nm diameter as displayed in Figure 5-10 (b). Such substructures evidenced from the phase image of monolayer terraces (not visible from height image) on glass substrate (Figure 5-6 (b)) are clearly noticeable from the height image of Figure 5-10 (a). Needle like crystallites reported on glass substrate do not grow frequently on ITO substrate like in the case of glass substrate (see Figure 5-3 (a)). The grains in the dendritic islands of 6T on ITO are quite similar to those observed on glass (Figure 5-10 (c)). They are granular, 100 ± 20 nm in diameter. These grains do not show any terraces or substructures within, indicates the amorphous nature of grains.

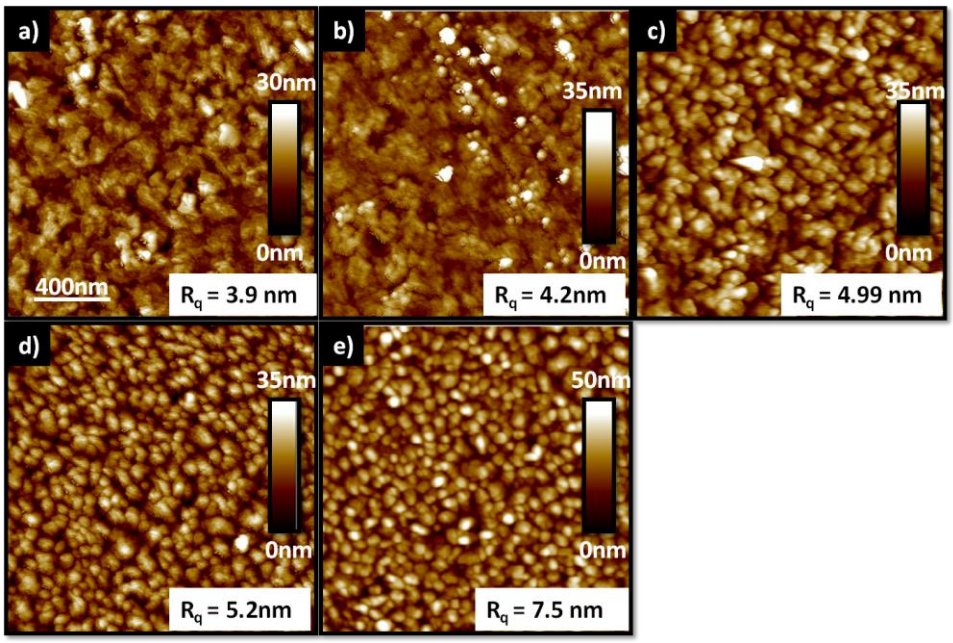

Figure 5-11 Sequence of AFM height images of 6T films with increasing thickness on ITO (a) 5 nm (b) 8 nm (c) 10 nm (d) 15 nm (e) 25 nm. The r.m.s roughness (R_q) is noted on the images.

The evolution of 6T film with thickness on ITO substrate is shown in Figure 5-11. For lower thickness (see Figure 5-11 (a) and (b)), the film follows the surface morphology of the ITO surface. With increasing thickness, 3D grains are formed. The dimensions of 3D grains become smaller for thicker films. To understand the evolution of film morphology, r.m.s roughness of both substrate and films are compiled and compared. The r.m.s roughness of the 2×2 μm^2 ITO substrate is 9.1 nm (Figure 3-15 (b)), with the surface of ITO exhibiting not so flat grains of different sizes (ranging from 250-350 nm in diameter). Each single grain of ITO also exhibits r.m.s roughness of 4.5 ± 0.1nm. The r.m.s roughness of the film shows an increasing trend with film thickness as shown in Figure 5-11, starting from 3.9 nm for 5nm thick film. Comparing the roughness of the substrate and the overlayer, it can be concluded that molecules fill the valleys in between the ITO grains substrate initially, and then 6T 3D islands start to grow on top of the ITO grains, where each 3D island forms by amalgamation of sub structures. The substructures are a direct consequence of roughness on each ITO grain. XRD studies in the earlier part of this chapter indicated standing self organization of 6T on ITO. That means, the molecules join to form

small crystallites, but due to the roughness of the ITO substrate, the crystalline orientation stays short ranged.

5.2 Study of electrical properties of 6T using C-AFM

C-AFM is employed to study the nanoscale electrical properties of 6T. Here, C-AFM tip coated with $PtIr_5$, with work function Φ ~ 5.2 eV [16] is employed as anode while the ITO with work function 4.8 eV is employed as cathode. Fermi level alignment of the 6T film in diode configuration during C-AFM analysis is described in Figure 5-12. Figure 5-12 (a) presents the energetic band diagram, before it is electrically connected. When the electrodes are directly connected to 6T, and no voltage is applied, the Fermi levels align and the built in potential V_d (~ 0.4 V) induces a band bending which prevents the hole injection at the anode tip. This is known as short circuit condition, represented by Figure 5-12 (b). When a positive potential is applied to the cathode (from here on positive dc sample bias), holes are injected at the cathode and move towards the tip anode (see Figure 5-12 (c)). While the band bending is favorable for the transport of holes from cathode to anode in positive dc sample bias, the energy level difference of ~ 0.4 V between the cathode (ITO) and HOMO of 6T constitutes a significant barrier for the holes. When a negative potential is applied to the cathode (from here on negative dc sample bias) exceeding the built in potential V_d, holes injected at the anode move towards the cathode (see Figure 5-12 (d)).

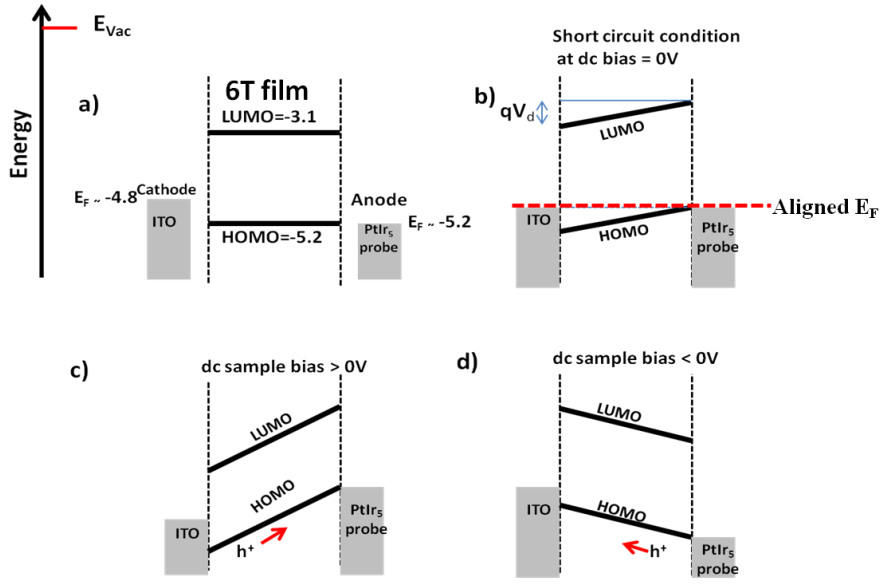

Figure 5-12 Energy band diagram of C-AFM diode configuration when (a) not electrically contacted to (b) in short circuit condition at zero dc sample bias, (c) in positive dc sample bias (d) in negative dc sample bias. The direction of hole transport is indicated by red arrow in (c) and (d). The energy levels are given in eV relative to vacuum level.

The work function of the $PtIr_5$ coated C-AFM tip is the same as the HOMO level of 6T and this ensures a perfect ohmic contact (no barrier) at the tip-film interface on injection of holes from the tip. The work function of both electrodes lie close to HOMO of 6T, hence favor the only transport of holes through the HOMO, whereas electron transport through the LUMO of 6T is practically impossible. The C-AFM tip-sample contact radius in this case can be extracted from the Hertzian equation (3.9), given in chapter 3. Applying the values of Young modulus for small molecules of ~ 15 GPa [17] , tip radius of ~ 20 nm and the applied force between the tip and the sample surface of ~6 nN, leads to a typical contact radius of ~ 2 nm. This low contact radius at low forces strengthens the non-destructive probing of the sample surface with a high lateral resolution (< 10 nm).

5.2.1 6T on glass in side configuration

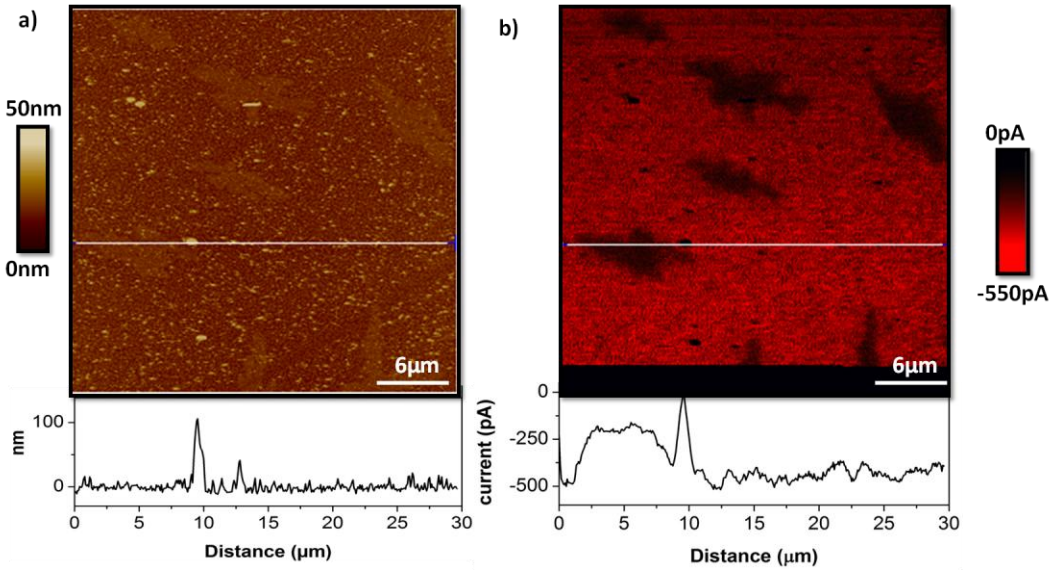

Figure 5-13 (a) 30 × 30 µm^2 C-AFM height image of a 15 nm thick 6T film on glass displaying background grains and dendritic islands. Below is the height profile corresponding to the white line displayed. (b) Simultaneously acquired current image showing different current contrast at the dendritic islands and back ground grains at a dc sample bias of -2 V. Below is the current profile corresponding to the white line displayed. Black color at the bottom of (b) represents zero current when no bias is applied.

In side configuration the local measurement was made close to, yet not directly above the ITO-electrode, in order to force the transport laterally through the 6T film. Typical morphologies of 6T thin films over an area of 30 × 30 µm^2 and their electrical response simultaneously acquired for dc sample bias of -2 V (holes injected from tip) are shown in Figure 5-13 (a) and (b) respectively, for the film deposited on glass with 15 nm nominal thickness. As previously explained, the height image shows two types of morphologies: background grains and dendritic islands. The black color in the bottom of current image in Figure 5-13 (b) corresponds to a zero current signal. It is evident that the two regions, i.e. the background grains and the dendritic islands has different current response for a given dc sample bias. From Figure 5-13 (b), in particular looking at the current profile, the dendritic islands are observed to conduct less, when compared to the background matrix. For a bias of -2 V in Figure 5-13 (b) the dendritic islands show C-AFM current of 220 ± 20 pA, while the back ground grains shows current value of

550 ± 20 pA. This lower current contrast at dendritic islands ought to arise from a combination of three possible causes: a) unfavorable injection to the grains from tip due to a possible barrier induced by the modification of HOMO level of 6T, b) difficulty in transport in the amorphous grains where the π-stacking may be altered c) difficulty for charge carriers in crossing the interface between the dendritic island and the background to reach the ITO electrode by lateral transport due to high grain boundary resistances.

In order to better understand how the background grains conduct, scans over smaller areas were investigated over the background matrix. Figure 5-14 displays the topography and corresponding current image for dc sample bias of -2 V over an area of $1 \times 1\mu m^2$ in the background matrix. As previously explained, two types of crystallites are observed on background grains, the terraced grains and needle like crystallites. A needle is marked in yellow and a grain marked in white in Figure 5-14 (a). The current and height profile signal corresponding to the blue line drawn on (a) and (b) is presented in Figure 5-14 (c). It is observed from the Figure 5-14, that the current response in two types of crystallites in the background matrix differs. The needle like crystallites conducts much less compared to the top of the grains (see Figure 5-14 (c)), within the voltage limit applied. For a sample bias of -2V, the top of island exhibits a current of -550 ± 20 pA, while a needle exhibits current of –100 ± 30 pA.

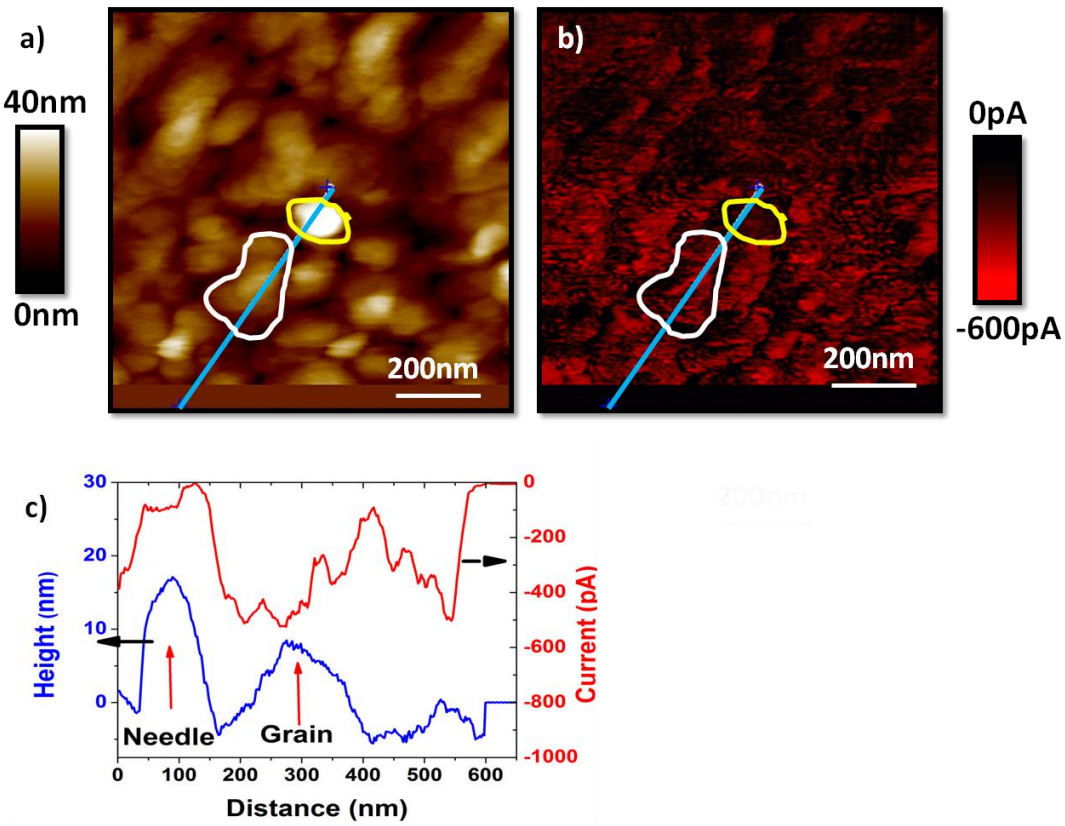

Figure 5-14 (a) 1 × 1 µm^{2}AFM height image of a 15 nm thick 6T film over the background matrix displaying terraced grains (marked in white) and needles (marked in yellow). (b) Corresponding current image at dc bias of -2 V, showing the specific current input of both the grains and needles (Black region at the bottom of (b) represents the current signal at 0V dc sample bias). (c) Section signal comparing the height and current corresponding to the blue line displayed on (a) and (b).

Possible reasons for the lower conduction trough the needles are: a) unfavorable injection to the grains from tip due to a possible barrier induced by the modification of HOMO level of 6T, b) needles grow over the terraced grains with a height three times higher than the grain itself. Given the fact that the orientation of molecules in needles are different from that in the terraced grains, the transport of holes from needles to the background can be hampered, owing to the highly resistive grain boundaries, resulting in low current signature in needles.

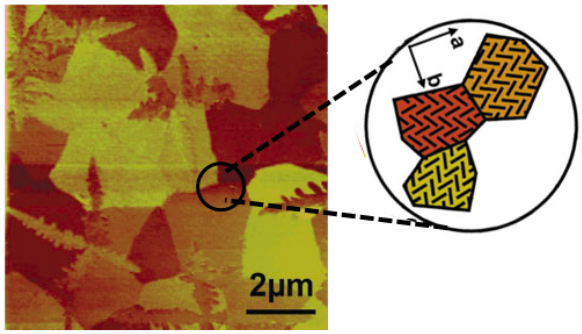

Figure 5-15 Transverse shear microscopy image of pentacene deposited on SiO_2, showing well defined faceted grains in the first monolayer. In this image the contrast corresponds to grain orientation. Inset presents the schematic of herringbone packing motif of pentacene molecule in nearby islands forming grain boundaries. Adapted from [1].

Also, the conductivity is high at the top of the grain, while less at the grain boundaries. This is illustrated by taking the example of pentacene monolayer reported in the literature [1]. Figure 5-15 presents transverse shear microscopy image of a small molecule, pentacene deposited on SiO_2 showing well defined faceted grains in the first monolayer [1]. In this image the contrast corresponds to grain orientation and the formation of grain boundaries are schematically represented in the inset of the same image. In the case of polycrystalline thin films of 6T, the in-plane orientation of molecules in different islands are in random direction just like in the case of pentacene (see Figure 5-15), causing disorder at the grain boundaries, which will affect the π-stacking and hampers conductivity at the grain boundaries. This is evidence to the fact that C-AFM, in this specific geometrical configuration and bias, probes the local current over a nanometric volume, just under the tip.

The origin of C-AFM current contrast is discussed in section 3.2.3 of chapter 3. According to that, in this very C-AFM geometry and bias, we expect local probing of current. In order to prove the local probing, we monitored the dependence of C-AFM current with respect the distance from the back electrode ITO, on a 15 nm thick 6T film at a dc sample bias of -2 V. Figure 5-16 (a) presents the C-AFM height image with ITO at one side, (b) presents the current image and (c) presents the average current profile over the line scan in the dashed square in (b). The profile shows that the current (see Figure 5-16 (c)) is almost a constant over a distance of 50 μm. The uniform current is expected for the particular distance, where contact resistance dominates over

the transport resistance ($\theta < 1$) according to the model discussed in chapter 3. As a consequence, the current probed is local and hence no significant variation with distance from the cathode is observed.

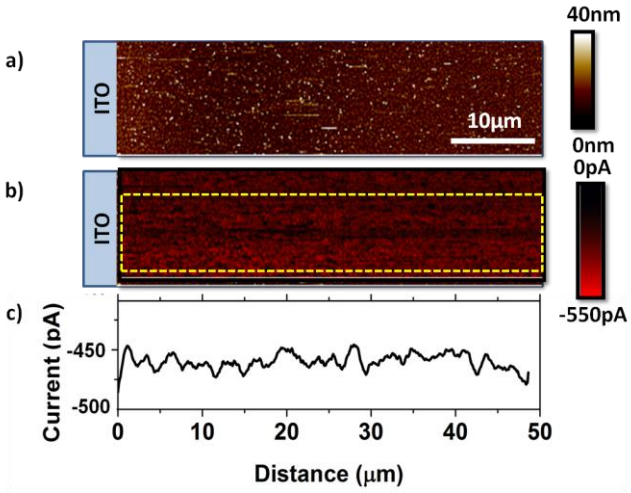

Figure 5-16 (a) C-AFM height image of a 15 nm 6T thin film in side configuration, cathode ITO is at one end. (b) Simultaneously obtained current image for dc sample bias of -2 V. (c) Average current profile over the line scan in the dashed square in (b).

Figure 5-17 presents the C-AFM current image 15 nm thick of 6T thin film obtained by ranging the dc sample bias from 0 V to -3 V along the slow scan axis, i.e., the vertical direction. The current progressively increases with the applied bias, as expected. The current-voltage characteristic constructed from the line-averaging of the current image vertically is shown in Figure 5-17 (b) and exhibits a quadratic dependence of current over voltage, indicating dominating space charge limited current in the measurements. In this configuration and bias, the contact resistance dominates ($\theta < 1$) and the C-AFM current probing is highly local, effective over a small volume under the tip with a radius *Z*. From the current voltage characteristic of Figure 5-17 (b), it is possible to extract the value of mobility from the equation (3.8) (the modified Mott-Gurney equation). The contact radius $r_{0,}$ calculated from equation (3.9) is ~ 2 nm; *Z* is ~ 30 nm. The value of Young modulus is ~ 15 GPa for small molecules [17] and ε_r = 3, a typical value for organic materials. The local mobility extracted using these values in equation (3.8), is 0.52 $\times 10^{-2}$ $cm^2/V.s$.

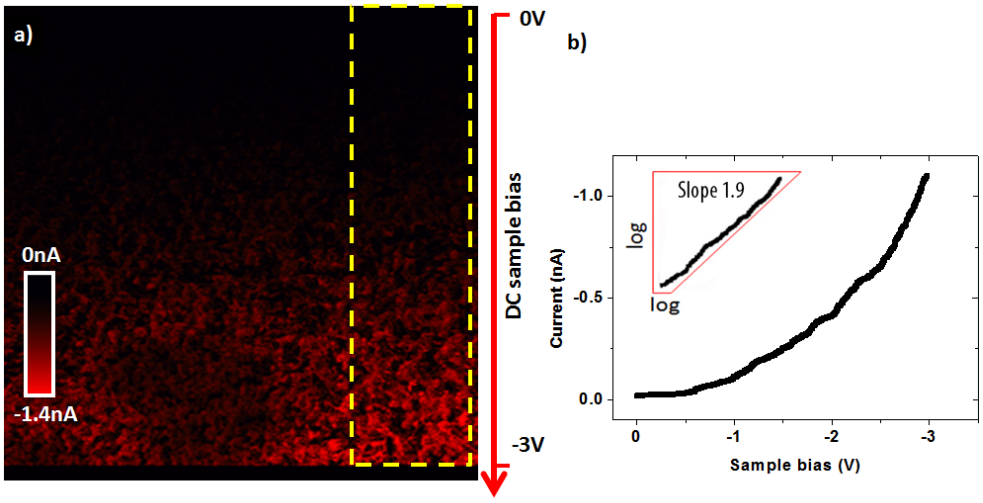

Figure 5-17 (a) C-AFM current image of a 5 × 5 μm^2 area of 15 nm 6T thin film on ITO substrate obtained by varying the dc sample bias from 0V (top of the image) to -3V(bottom of the image). (b) I-V characteristics derived from line averaging of the current image. Inset shows the I-V curve in log-log scale.

Charge transport in side configuration is comparable to that in a transistor, where molecules are oriented in upright standing position and charge transport occurs through the favorable π-stacking direction. Therefore, the mobility extracted using C-AFM configuration is compared with FET mobility. The highest reported FET mobility of 6T is (2 – 3) ×10^{-2} cm^2/Vs [18, 19], while in our case is approximately 5 times lower than the highest mobility reported. This difference in the mobility is expected and is attributed to the fact that we used amorphous glass as substrate (r.m.s roughness 1.3 nm), while highest mobilities are often reported on transistors with 6T deposited on smooth SiO_2 (r.m.s roughness < 0.3 nm [7]) substrates. As a result, the molecules orient better on SiO_2, results in better overlap of nearest neighbor molecular orbitals and hence provides better carrier mobility. Also the current contribution due to low conducting needles and grain boundaries include, while line averaging the C-AFM current image, decreases the intensity of current measured, there by decreases the mobility. However the significance of this result rests on the fact that the modified Mott-Gurney equation provides a non destructive way to extract local mobility of sophisticated organic devices.

As local current is probed in C-AFM at this configuration and bias, it is possible to extract the local mobilities offered by a specific area in a polycrystalline film. As the top of the grain and the

grain boundaries conduct differently, and thanks to the high resolution of C-AFM, it is possible to compare the mobility at the grain boundaries with respect to grains present in the 6T film. In Figure 5-18 (a) current voltage curves are constructed for these two specific areas, on top of the grain and at a point on grain boundary by scanning same area with a sample bias starting from 0V to -3 V, in 0.5V increment steps.

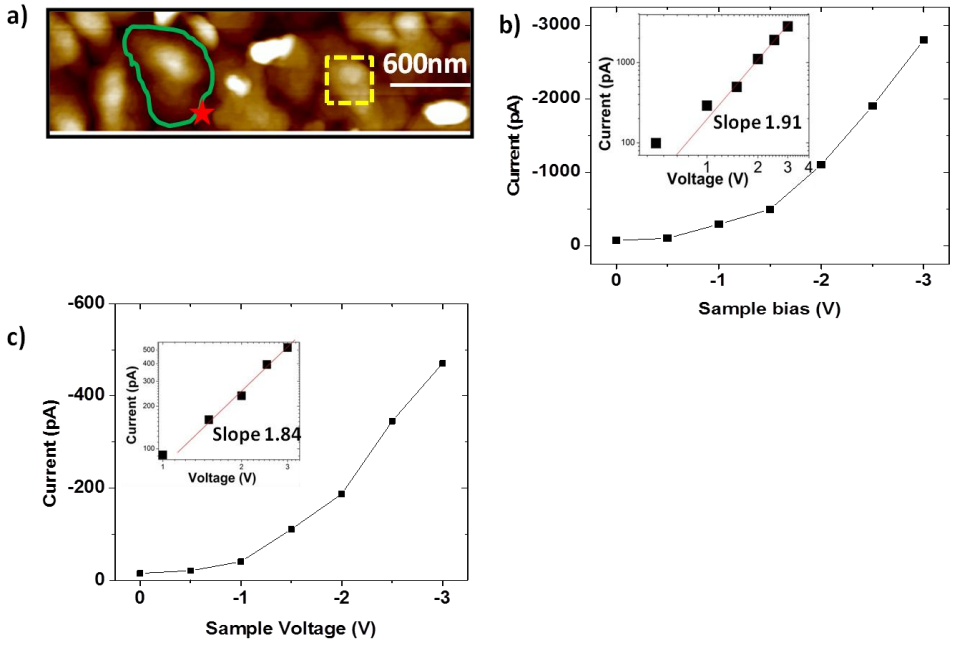

Figure 5-18 (a) 3 × 0.75 µm^2 height image of 15 nm thick 6T film, in which a grain boundary is marked in green and top of the grain is marked with yellow box. Different sample bias is applied on the scan area starting from 0 to -3 V with an increment of 0.5 V. (b) I-V curve constructed by taking average current on the marked grain for different voltages (c) I-V curve constructed by taking current for different voltages on at the star marked point on the grain boundary.

The I-V curve thus constructed on the top of the grain, marked in yellow in Figure 5-18(a), is shown in Figure 5-18(b), it shows a quadratic dependence of current over voltage indicating SCLC mechanisms is acting. The fit of the SCLC behavior yields the local mobility values over a well oriented terraced grain by substituting the values of r_0, Z and ε defined in the previous paragraph in equation (3.8). The local mobility extracted is 1.4 $\times 10^{-2}$ cm^2/Vs, very close to the highest reported mobility for 6T transistors. Similarly I-V profile constructed from grain

boundary (see Figure 5-18(c)) yields a value of 0.22×10^{-2} cm^2/Vs. It indicates a decrease of about one order of magnitude in the mobility values at the grain boundaries when compared to highly oriented grains.

It is observed that the 6T grains cover the substrate surface completely after a critical nominal thickness of ~ 10 nm. All films with nominal thickness above 10 nm provide same electrical response as that described above. Films with nominal thickness below 10 nm are partially covered on the glass substrate. The investigation on the first few layers of 6T thin films, demonstrated to be the only ones responsible for charge transport, in the case of orderly grown layered 6T transistors [20]. In order to study such partially covered films, we deposited films with 8nm nominal thickness at a very low deposition rate of 0.5 Å/min. Figure 5-19 (a) is a schematic representation of film structure observed in these samples, while Figure 5-19 (b), presents the C-AFM height image of partially covered film showing a critical degree of coalescence between the islands. The scan was performed at a distance 200 μm away from the ITO cathode. The film shows predominantly monolayer islands of 6T connected to each other with a critical degree of coalescence. Some of them show up to 3 monolayer terraces one on top of another. The white features in Figure 5-19 (b), represents the second and third monolayer terraces. The current image is presented in Figure 5-19 (c). However the current image does not show expected correlation with the height image. Some grains showed higher conductivity while some others are less conductive, even though the height images presents homogeneous distribution of 6T islands. To better understand this unexpected behavior we made I-V curves on specific grains in three different regions. At first we took I-V curves on the grains well connected to ITO and at a very close distance L (within 5μm) (on region 1, marked with a red star in Figure 5-19 (a)). Here, as in the case of thick films, the grains exhibit a quadratic dependence of current with respect to the on voltage i.e. a slope 2 in log-log scale (see blue curve of Figure 5-20). As in this current regime the distance *L* between the probe and the ITO is small, the current is contact resistance dominated ($\theta < 1$) and follows space charge limited mechanisms, as explained in chapter 3.2.3.

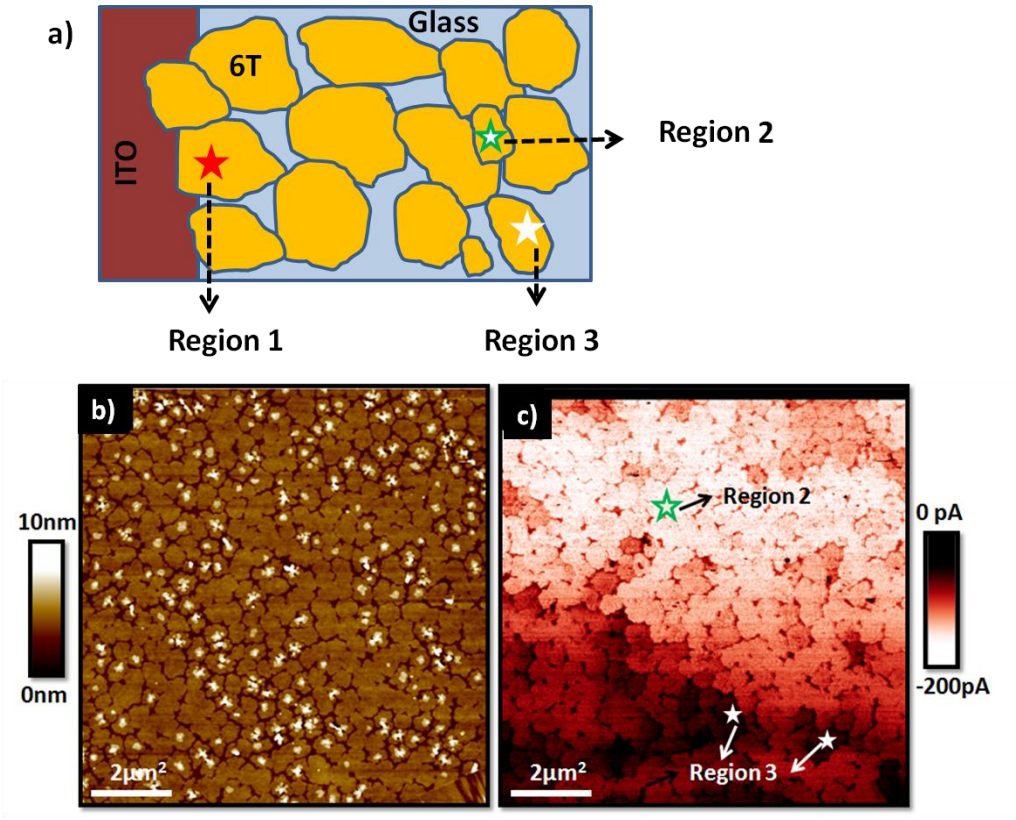

Figure 5-19 (a) Schematic diagram of partially covered 6T thin film showing region 1, region 2 and region 3. (b) 10 × 10 µm^2 C-AFM height image at a distance 200 µm away from the ITO. (c) Current image of (b) showing region 2 and 3 at a dc bias of -2 V. The stars indicate the areas in which I-V profiles (point and shoot) has been recorded. Red star represents region 1, green star represent region 2 and white star represent region 3.

However it is found that when the distance between the probe and the ITO (L) increases to nearly 200 µm, the current starts decreasing with distance and does no longer provide a contact resistance dominated current. It has to be noted that for this probe-ITO distance in well connected thicker films, the dominating current was space charge limited. We performed I-V curves on grains showing different current response in current image (Figure 5-19 (b)), which is scanned at a distance L ~ 200 µm. In Figure 5-19 (b)), there are grains showing higher conductivity (from here on called as region 2, marked with green star in Figure 5-19 (a) and (c)) and grains showing lower conductivity (region 3, marked by white star in Figure 5-19 (a) and (c)).

The local I-V curve recorded in region 2 and reported in Figure 5-19, exhibits a linear dependence of the current with the voltage (slope~1 on the log-log scale I-V characteristic) (see black curve of Figure 5-20).This can be explained on the basis of transport resistance dominated current mechanisms explained in section 3.2.3. It has to be noted that since the film is not fully covered, the holes injected from the probe have to travel very large pathways effectively to reach the ITO, even though *L* is 200 µm. Since effective distance to be travelled by the holes increases significantly for partially covered films, transport resistance dominates over contact resistance and results in transport resistance dominating regime here i.e. $\theta > 1$. The large distance to the ITO back electrode also explains the smaller current values in region 2, as compared to I-V characteristics recorded with the same dc sample bias in region 1. Such linear dependence of C-AFM current on voltage has been observed previously by Bolsee et al [21] where current decreases with distance. The resistance of the film calculated from the linear I-V curve in transport dominated regime is $(4.7 \pm 1) \times 10^9\ \Omega$ which is close to the value reported in the literature [21].

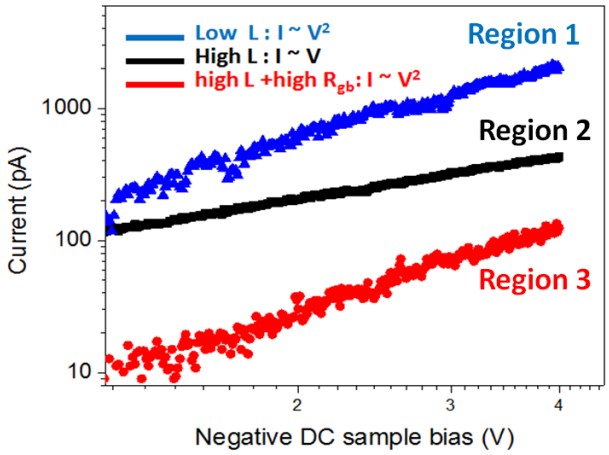

Figure 5-20 Local I-V characteristics recorded on region 1 (blue), region 2 (black) and region 3 (red) in log-log scale showing quadratic variation of current with voltage for region 1 and 3 while a linear current voltage relation is displayed in region 2

The grains with lower conductivity in region 3 of Figure 5-19 (c) are poorly electrically connected to other grains, i.e. they are connected to other grains at very few points only, and displaying a lower conductivity when compared to region 1 and 2, represents another electrical

regime. Interestingly the I-V curve recorded here shows a quadratic variation of current with respect to the voltage (slope nearly 2 in log-log scale), with the current intensity lower than that in region 1 and region 2 for any bias (see red curve of Figure 5-20). A hypothesis to explain this behavior can be proposed. In these not very well connected grains, grain boundary resistance (R_{gr}) becomes predominant relative to the transport and contact resistances and greatly limits the charge transport from one grain to another. The quadratic variation of current with respect to voltage is typically a signature of space charge limited current. However whether the observed quadratic behavior is related to space charge mechanism is still an open question.

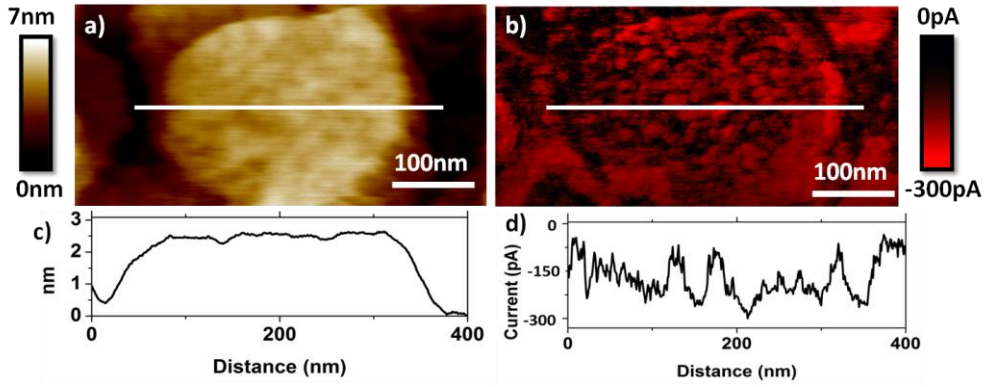

Figure 5-21 (a) Height image of a 500 × 250 nm^2 area of 6T monolayer deposit on glass substrate and its height profile below. (b) C-AFM current image of (a) at -1.5 V dc sample bias. (c) & (d) Cross sectional height and current profile along white lines on (a) and (b) respectively.

In view of understanding the local electrical properties in a single terraced grain, when they are contact resistance dominated (region 1), magnified C-AFM scans were performed. As explained before, the phase images (see Figure 5-6 (b)) obtained using AFM displayed mosaics like nano crystallites in magnified scans. Using C-AFM, the local electrical properties of these nano crystallites are investigated. Figure 5-21(a) displays the topographical image of a monolayer grain. Looking closely at the corresponding current image at a dc sample bias of -1.5 V (Figure 5-21 (b), it is observed that the monolayer island does not conduct uniformly, but it comprises highly conducting spots surrounded by lesser conducting boundaries. The local conductivity of conductive spots is about two times higher than that at the boundaries. This result suggests that even though the molecules stand up with respect to the substrate inside these grains (which is confirmed by the height of the monolayer), molecules agglomerate to form nano crystalline

mosaics of diameter 30 ± 10 nm. This is in agreement with the phase images reported in Figure 5-6 (b)). Figure 5-22 (a) shows the topography of two monolayer terraces, one on the top of another. The simultaneously attained current image for a sample bias of -2 V presented in Figure 5-22 (b) displays spots with high local conductivity, as explained before. A magnified current image of the marked region in (b) presents a part of bottom terrace and top terrace is presented in (c). The current line profile (c) is shown in (d) of the same Figure 5-22.

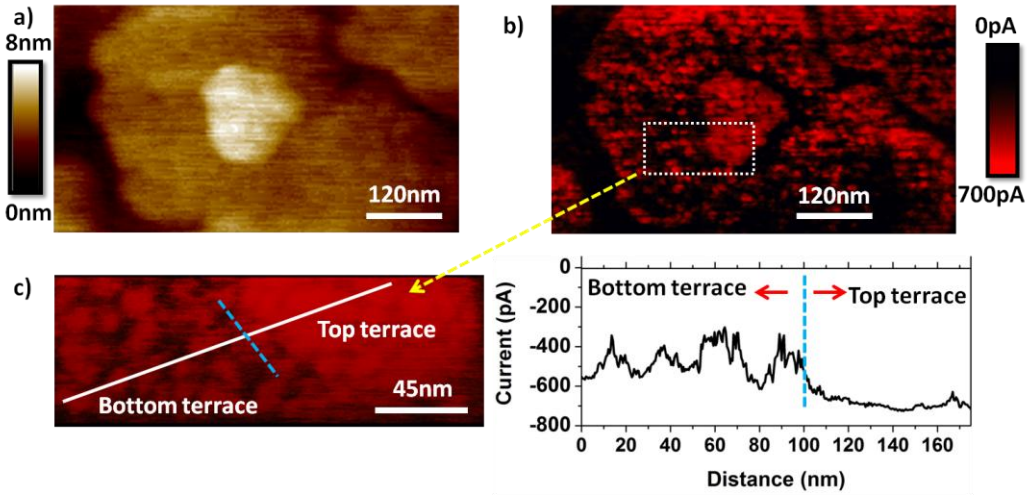

Figure 5-22 (a) Height image two 6T monolayers one on top of another on glass substrate (b) C-AFM current image of (a) at -2 V dc sample bias. (c) Zoomed image of the marked region of (b) & (d). Cross sectional current profile along white lines on (b). The line profile shows the difference in the current conduction in bottom grain and top grain.

If the bottom terrace is taken into account in Figure 5-22 (b) and (c), individual nano crystallites appear to be separated by broader grain boundaries more than that on the top terrace. In the top terrace the nano crystallites seem to have packed more tightly compared to that in the first island. This scenario is visible on the zoomed current image which comprises of a part of top and bottom terraces (Figure 5-22 (c)). The current profile (d), displays the current response along the white line drawn in Figure 5-22 (c). The current profile on the bottom terrace shows higher current on the nano crystallites while lower current is observed at the boundaries separating individual nano crystallites. In the case of current profile on the top grain, owing to the tight packing of nano crystallites the negative current seems to be uniform and higher than that in the bottom terrace. This result indicates that the self organization of molecules in terraced islands progressively get

better with thickness. Since the terrace like morphology is clearly observed in height image, with constant height in a given plateau of single terraces, we can conclude that the difference in C-AFM current image might originate from the different injection barrier between the probe and the sub grains or resistance between individual grains due to grain boundaries. However the grain boundary resistance is a more likely explanation for decrease of current in between the grains. This explains why thin film transistors provide lower mobility values of the order of magnitude of two, compared to single crystalline transistors, as the delocalized holes find a slight disruption in molecular packing every 35 ± 10 nm (size of sub crystalline domains). From the point of view of the C-AFM technique, this result proves that its resolution in the current images is very high, when compared to that of the usual height image.

Side configuration in positive sample bias

In side configuration with a positive sample dc bias, holes are injected from the broad ITO electrode to the point C-AFM tip-sample back contact. The typical electrical pathway of holes for two polarities is entirely different. For negative dc sample bias, holes are locally injected from a point probe and might find a favorable pathway to ITO. On the contrary, in positive dc sample bias, the charges are injected along the macroscopic ITO contact, so that their pathways to the probe definitely differ from the case of negative dc sample bias and leads to an averaged electrical signature. Hence, there is no local probing in this case. When holes are injected from back electrode which is of the order of millimeters in width (w), to a point electrode at a few microns apart, the effective pathways for the carriers is of the order of millimeters. This is sketched in Figure 5-23 (a) where w is the width of the injecting ITO electrode, *L* is the perpendicular distance from tip to ITO (few tens of microns). The effective pathway for holes from back electrode to ITO will be approximately equal to the width of the ITO electrode. For such large pathways (few mm), the transport resistance limits ($\theta > 1$) the current behavior, given the contact resistance at the ITO-sample interface is negligibly small compared to transport resistance offered by the film as explained in section 3.2.3 and the expected behavior of current I-V characteristics is linear.

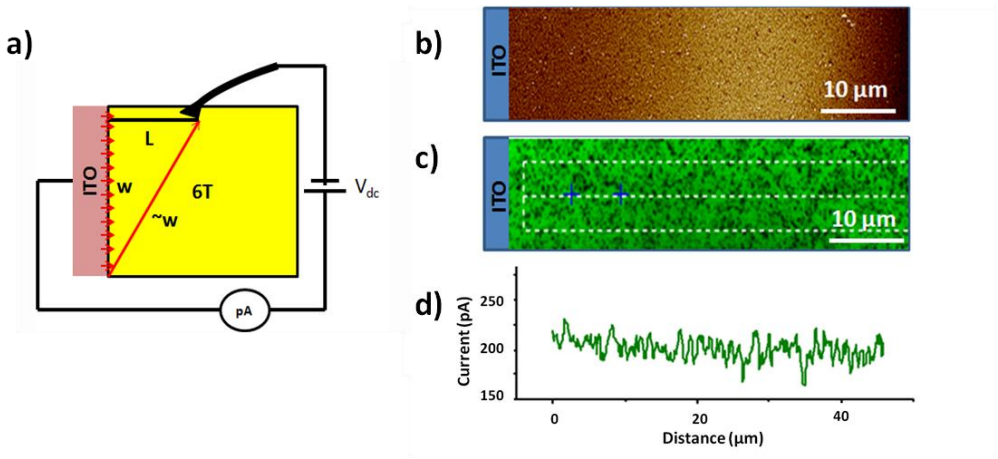

Figure 5-23 (a) Schematic diagram showing injection of holes from macroscopic ITO electrode to the point probe. The width (w) of the injecting ITO electrode is of the order of millimeters and the distance between the electrodes L is in the order of tens of microns. (b) C-AFM height image of 15 nm 6T thin film in side configuration, back electrode ITO is at one end (c) simultaneously obtained current image for positive dc sample bias of 2V (d) line averaged current profile of (c).

In Figure 5-23 (b) C-AFM height image of a 15 nm 6T thin film in side configuration, with the ITO cathode illustrated on the left. The corresponding current image at a dc sample bias of 2V and the line averaged current profile signal is presented in Figure 5-23 (c) and (d) respectively. Figure 5-23 (d) shows that the current is uniform with respect to the distance from the back electrode for a distance of 50µm. However, if we were probing current in transport dominated regime, the current ought to decrease with distance. The absence of such decrease is probably due to the following reason. As explained in the paragraph before, the average effective electrical pathways for holes is of the order of few millimeters, and as long as *L* is much lower than the width of the injecting ITO contact (here, $L/w \sim 10^{-2}$), we will get uniform current in C-AFM configuration, irrespective of *L*.

In Figure 5-24 the typical height and current images in side configuration as shown for a sample of 15 nm under bias of 2 V. Black color in Figure 5-24 (b) represents zero current. As in the case of dc negative bias, the dendritic islands conducts negligibly, in the case of negative sample bias in side configuration discussed in the same section. In Figure 5-24 (b), the background region exhibits some low conducting spots, representing the needles.

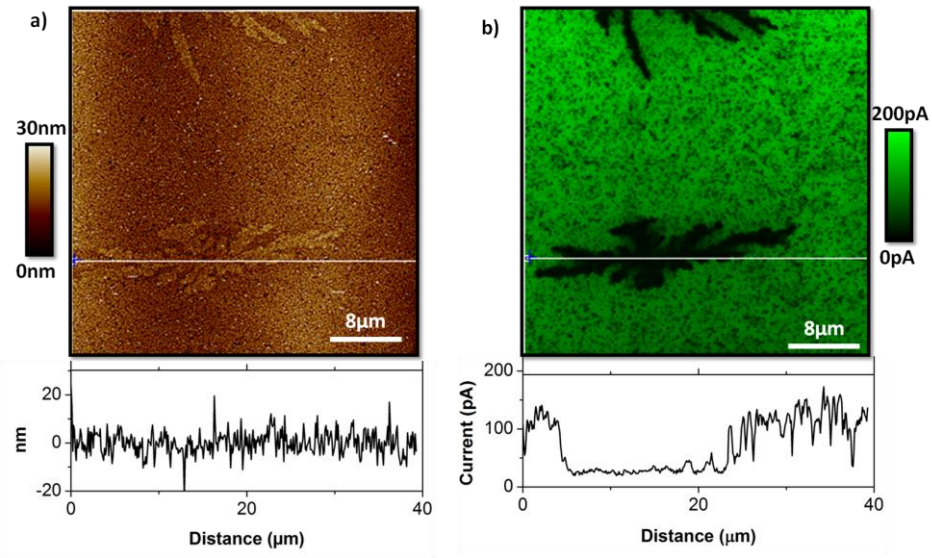

Figure 5-24 (a) Height image of a 40 × 40 µm^2 area of 15 nm 6T thin film on glass substrate showing background grains and dendritic islands in side configuration (b) C-AFM current image of (a) at 2V dc sample bias. Below (a) and (b) is the cross sectional signal along the white line drawn on (a) and (b) respectively.

Magnified current image of the background grains reveals how the regular terraced grains and needles respond to positive dc sample bias (Figure 5-25). The former conduct uniformly all over the surface while the latter conduct much less. The profile shows how the current decreases drastically at the needles. Needles have different molecular organization compared to the terraced grains likely to result in high resistive grain boundaries offers the ITO injected holes an additional resistance to overcome reach to the tip. This explains the decrease in current conductivity through the needles. In Figure 5-25 (b) for a sample bias of 2 volt, the needles provide current around 25 pA while the terraces shows a current of more than 125 pA.

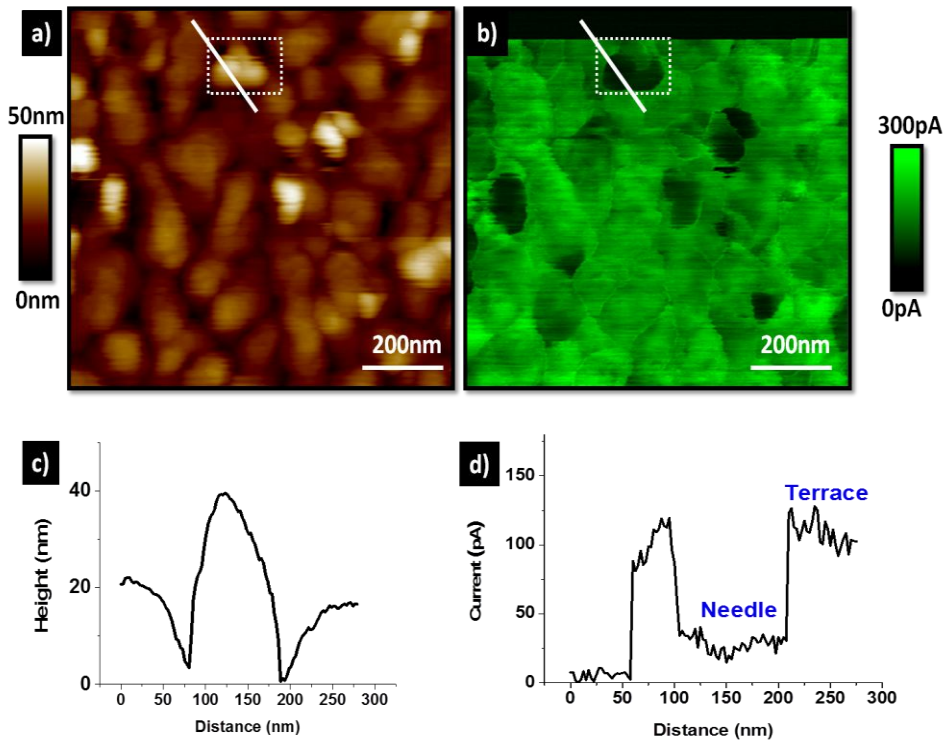

Figure 5-25 (a) C-AFM height image of a 1 × 0.75 μm^2 area of 15 nm 6T thin film on glass substrate showing background grains in side configuration (b) C-AFM current image of (a) at 2V dc sample bias. (c) & (d) Cross sectional height and current profile along the white lines on (a) and (b). Local conductivity on needles is found to be very less. Black color at the top of (b) represents zero current signal at 0V dc sample bias, kept as a reference.

In order to understand the current mechanisms through the film when positive sample bias is applied, average current voltage curves are taken and are shown in Figure 5-26. Figure 5-26 (a) presents C-AFM height image of a 10 × 10 μm^2 area of 15 nm 6T thin film on glass substrate showing background grains, (b) presents the current image corresponding to Figure 5-26 (a) obtained by varying the dc sample bias from 0V (top of the image) to +3V (bottom of the image), while (c) presents the current voltage characteristic derived from vertical line averaging of the current image (b). The I-V profiles on positive sample bias shows a linear behavior [22].

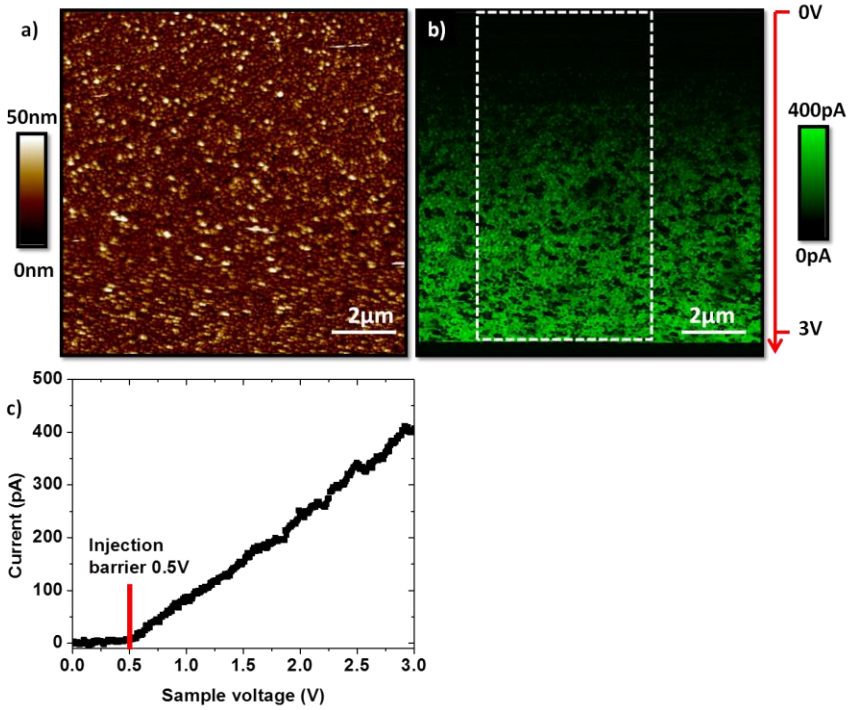

Figure 5-26 (a) Height image of a 10 × 10 µm^2 area of 15 nm 6T thin film on glass substrate showing background grains in side configuration (b) C-AFM current image of a 10 × 10 µm^2 area of 15 nm 6T thin film on glass substrate obtained by varying the dc sample bias from 0V (top of the image) to +3V (bottom of the image). (c) I-V characteristic derived from vertical line averaging of the current image (b) showing linear behavior.

The intensity of current for a given bias is lower than that in the case of the same .negative sample bias (see Figure 5-17). From Figure 5-26 (c) an injection barrier of 0.5 V is observed, which is very close to the energy level difference between the anode and the cathode. The resistance of the film is calculated using the Ohm's law and is (6.8 ± 1) × 10^9 Ω which is very close to the resistance value extracted from the transport dominated regime in negative sample bias.

5.2.2 6T on ITO in vertical configuration

Electrical properties of 6T deposits on ITO were also studied with C-AFM. Here the vertical conduction of holes in the film is probed. Note that, in vertical configuration the injected charges

have to travel trough the thickness of the film which in our case is less than 50 nm where as in side configuration the distance between the probe and the ITO is of the order of few microns.

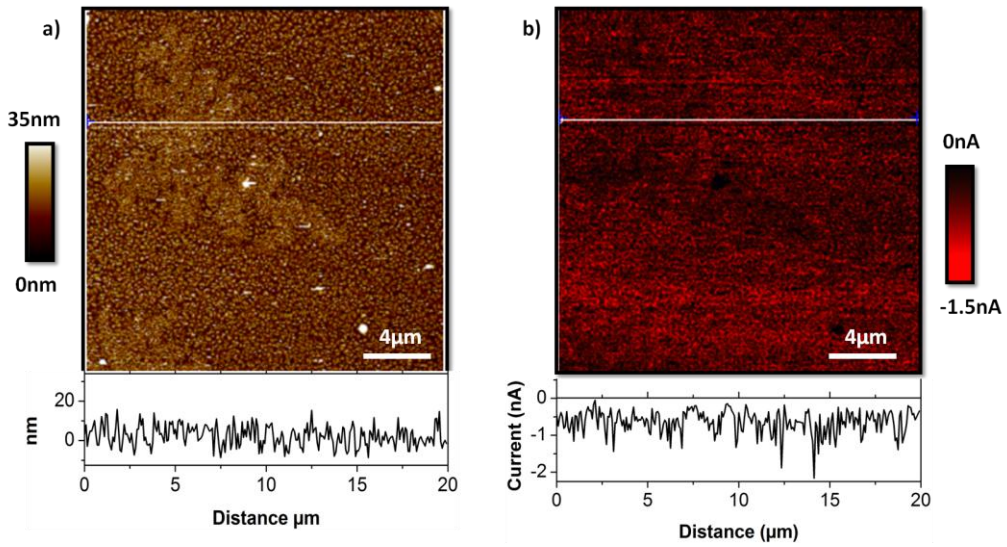

Figure 5-27 (a) C-AFM height image of a 20 × 20 µm^2 area of 15 nm 6T thin film on ITO substrate showing background grains and dendritic islands. (b) C-AFM current image of (a) at -0.5 V dc sample bias. Below the images are the cross sectional signal along the white line displayed on (a) and (b) respectively.

In vertical configuration at negative sample bias, the carriers are injected from the C-AFM tip into 6T towards the ITO electrode. Typical morphologies of 6T thin films over an area of 20 × 20 µm^2 and their electrical responses simultaneously acquired for dc sample bias of -0.5 V are shown in Figure 5-27 for a film deposited on ITO with 15 nm nominal thickness. The current image in Figure 5-27 (b) shows high contrast for both dendritic and back ground grain like organization. The average current at the background grains for -0.5 V sample bias is about 600 pA while that given by grains in dendritic islands is around 550 pA. The current obtained on vertical configuration for a 15 nm film is approximately 6 times higher than in the side configuration for a dc sample bias of -0.5V. In side configurations the current exhibited by dendritic grains is less than half of that given by the background grains (see Figure 5-13). However, in the case of 6T on ITO, grains in dendritic islands exhibit almost same current as the background grains for a given bias. This is because in this case, the dendritic islands are directly connected to the ITO and the holes travel vertically through the film thickness, while in side

configuration the holes injected has to cross additional grain boundaries while travelling longitudinally to reach the back contact. On has to keep in mind that, in vertical configuration, the holes have to travel perpendicular to the π-stacking direction, while in side configuration, charges hop through favorable π-stacking direction.

Magnified current images were taken to better understand the local conductivity of the grains. Figure 5-28 (a) C-AFM height image of a 1 × 1 μm^2 area of 15 nm film on ITO substrate is presented showing background grains, while (b) of same figure displays C-AFM current image of (a), at -1V dc sample bias. Overlying grains are marked in both height image (black color

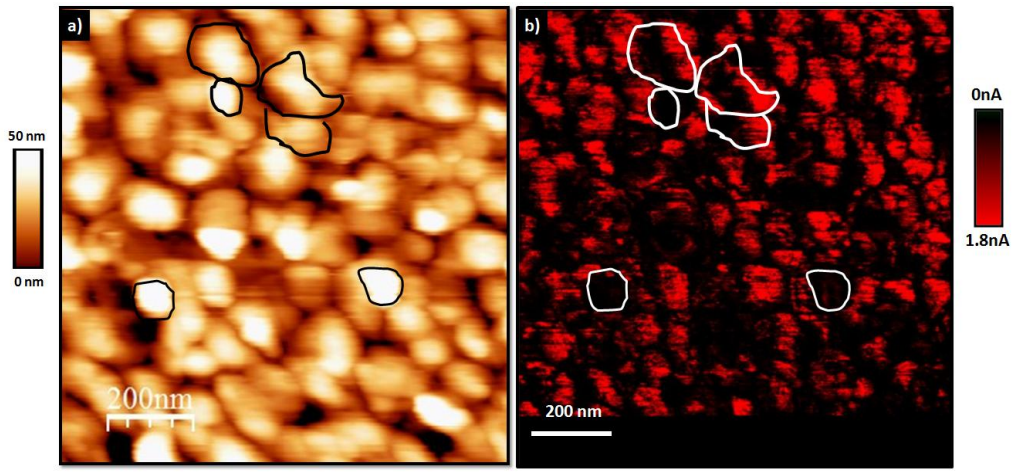

Figure 5-28 (a) C-AFM height image of a 1 × 1 μm^2 area of 15 nm 6T thin film on ITO substrate showing background grains. (b) C-AFM current image of (a) at -1V dc sample bias. Overlying grains are marked on (a) and (b). Black color at the bottom of (b) represents zero current signal at 0 dc sample bias, kept as a reference.

marking) and current image (white color marking). Figure 5-28 (b) shows highest current contrat on top of low lying grains as well as at the lower part of the higher grains. The current contrast exhibits a decreasing trend with respect to height of the grains. Furthermore, the highest grains might result from grains sitting on top of other with no direct contact to the ITO. Such grains exhibited very low conductivity. This is probably due to the added grain boundary resisitance along with height of the grains.

Figure 5-29 (a) presents the height image of 15 nm 6T film on ITO and Figure 5-29 (b) is the corresponding current image obtained by ranging the dc sample bias from 0 V to -3 V along the

slow scan axis, i.e. the vertical direction. The current-voltage characteristic constructed from the line-averaging of the current image is shown in Figure 5-29 (c). However the current did not followed the V^2 law and in log-log plot the I-V characteristics showed a slope of ~ 3. More point and shoot I-V profiles were taken on films with different thickness (15 nm, 25 nm and 40 nm),

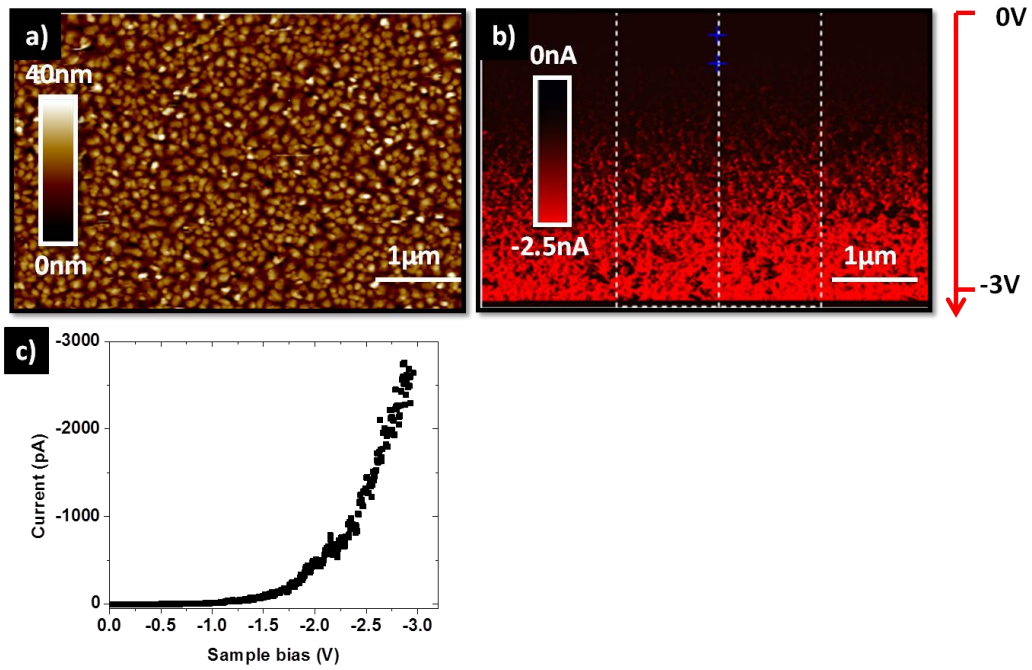

Figure 5-29 C-AFM height image of a 5 × 3 µm^2 area of 25 nm 6T thin film on ITO only showing background grains. (b) C-AFM current image of (a) obtained by varying the dc sample bias from 0V (top of the image) to -3 V (bottom of the image). (c) Current-voltage characteristic derived from line averaging over the dashed box displayed in the current image.

in order to understand the role of thickness in determining the current. It is to be noted that on side configuration in negative sample bias, the C-AFM gives local current which is independent of the distance between the electrodes (in contact resistance dominated regime); in addition, in side configuration the current varies quadratically with respect to voltage ($I \alpha V^2$). Figure 5-30 shows the I-V profiles taken as point and shoot for three different thickness. From the figure the behavior of I-V profiles for all the mentioned thickness were found not to be quadratic, unlike in the case of side configuration. For all thickness, the all I-V profiles give a slope of ~3.

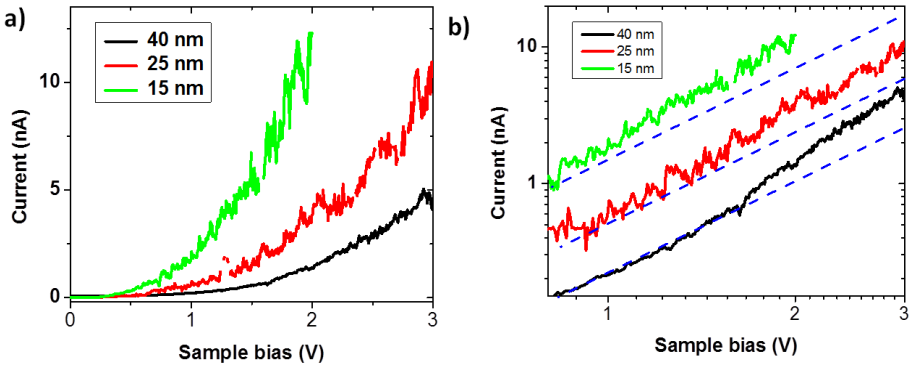

Figure 5-30 (a) I-V characteristics of 6T thin films on ITO with thickness 15 nm, 25 nm and 40 nm in negative sample bias. (b) The log-log plot of I-V characteristics shows deviation from quadratic behavior, i.e. $I \alpha V^2$ law. The blue dashed line corresponds to slope 2.

Also we do observe the current vary with the film thickness. For higher thickness lower is the current. This suggests that unlike side configuration where contact is limiting the current, the bulk properties of the film is limiting the current in vertical configuration. So we are no longer probing locally in vertical configuration. So in this scenario, either Mott- Gurney law or the modified Mott-Gurney for local contact (see equation 3.8) cannot be used to extract the mobility of charge carriers. Deviations from ideal space charge limited behavior have been reported on organic semiconductors before. Basically two interpretations were proposed to explain this deviation from the V^2 law. The first approach is based on the frame work of SCLC in which mobility is treated as a constant and the transport is mediated through the exponential distribution of traps in the band gap, where charge carriers are trapped and released. Here deviating from the Mott-Gurney law, current voltage characteristics display $J \alpha V^m$ with m >2 [23]. Many groups have reported a carrier density dependent mobility model that originates due to the hopping through the exponential tail of density of states (DOS) [24-26]. However, this explanation is does not seems to fit with our result. Because we do observe deviation from V^2 dependence of current in negative sample bias in side configuration as well as positive sample bias for vertical configuration (is explained in the later part of this section)

The second approach is the assumption of electric field dependent charge carrier mobility described by a Poole-Frenkel type behavior [27-29] where,

$$\mu = \mu_o \exp\sqrt{\frac{E}{E_0}} \quad (5.1)$$

Here, μ_o is the zero field mobility, $E = V/L$ is the electric field in planar device, and E_0 is the field coefficient. In these conditions also, the V^2 law changes to V^m where m > 2. Weber et al. [30] has used Poole-Frenkel equations in C-AFM configuration to explain the deviation from ideal space charge regime mobility. However macroscopic and empirical Poole-Frenkel equation is not suitable in C-AFM configuration even though many groups have used it to find out the mobility. This is because of the geometrical configuration of C-AFM which uses a hemispherical nano tip. In plane parallel configuration, the trap free space charge limited field distribution E varies with square root of the thickness of the film, while in standard point probe configuration [31], the trap free space charge limited field distribution E in spherical flow case is given by the following equation

$$E \alpha \frac{1}{\sqrt{L}} \quad (5.2)$$

$$V \alpha \sqrt{L} \quad (5.3)$$

where L is the thickness of the film. As the field distribution is different in two geometrical systems, macroscopic Poole-Frenkel law is no longer valid in C-AFM case. The equation for current in C-AFM geometry in vertical configuration for SCLC dominating transport is given by

$$I = \frac{3}{4}\pi\varepsilon_0\varepsilon_r\mu\frac{V^2}{L}\,[31]^1 \quad (5.4)$$

[1] The equation (5.3) is adapted from reference [31] which explains the space charge limited current in spherical flow. However to make it compatible with C-AFM geometry with a hemispherical tip, the original equation is multiplied by 1/2.

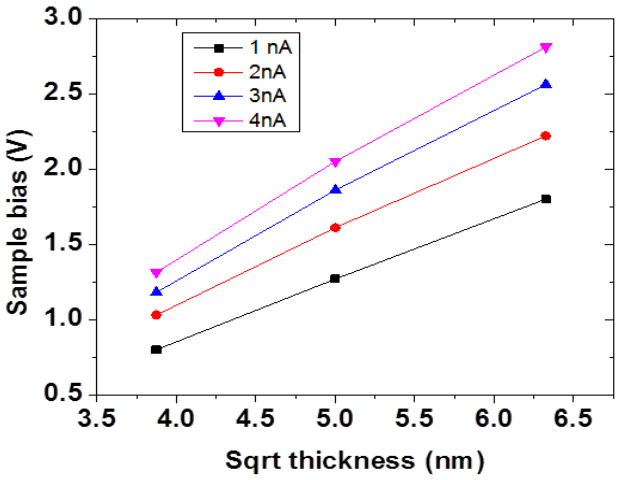

Figure 5-31 Square root film thickness versus sample voltage graphs for normalized current values 1 nA, 2 nA, 3 nA and 4 nA, constructed from Figure 5-30 (b).

In order to prove the validity of equation (5.3) and thereby (5.4), a graph (see Figure 5-31) with square root of film thickness versus sample voltage has been constructed from the I-V profiles in Figure 5-30 (b), for normalized current values of 1 nA, 2 nA, 3 nA and 4 nA. Figure 5-31 shows the results, with a clear linear dependence of voltage on square root of thickness of the film. This implies L^{-1} variation of SCL current in C-AFM configuration compared to L^{-3} dependence in planar devices.

Yet in Figure 5-30 I vary with V^3 instead of V^2. No modification of permittivity of 6T is expected with V or E. So from equation (5.4), only the modification of mobility with E is expected, to be expressed as

$$\mu = \mu_0 E \qquad (5.1)$$

where μ_0 is the zero field mobility and E the electric field in spherical flow case (sphere-plane configuration). However in the case of 40 nm film, the I-V profile displayed quadratic behavior for a very short voltage range (starting from 0.8 V to 1.7 V) and after that it deviates from the quadratic dependence to get a slope of ~ 3 in lo-log I-V profile(see Figure 5-30 (b)). In this voltage range, the mobility extracted using equation (5.4) is 1.43×10^{-3} cm^2 /Vs. This mobility value is one order less than the highest mobility value extracted for side configuration. However,

this decrease is expected as in side configuration, where in 6T π-stacking direction is same as that of the hole transport direction, while in vertical configuration π-stacking direction is perpendicular to the direction of hole transport. As quadratic variation in a small voltage range in the I-V profile is observed for 40 nm film, while not in the case of 25 nm and 15 nm and less thicker films, the value of the radius of the hemisphere just below the tip, beyond which the voltage drops drastically, *Z* (see section 3.2.3) is approximated to be less than 30 nm.

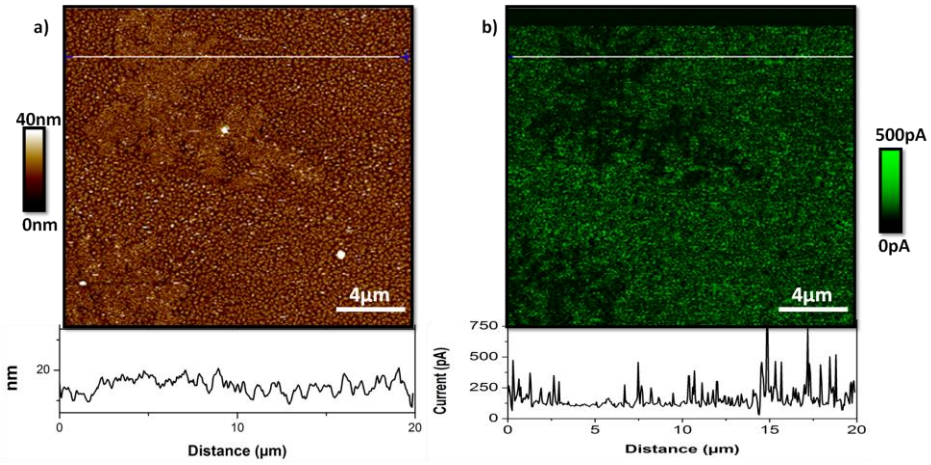

Figure 5-32 (a) C-AFM height image of a 20 × 20 µm^2 area of 15 nm 6T thin film on ITO substrate showing background grains and dendritic islands. (b) C-AFM current image of (a) at 2V dc sample bias. Below (a) and (b) is the cross sectional signal along the white line drawn on (a) and (b) respectively.

In vertical configuration at positive sample bias, the carriers are injected from the planar ITO to C-AFM tip. Typical morphologies of 6T thin films over an area of 20 × 20 µm^2 and their electrical response simultaneously acquired for dc sample bias of + 2V are shown in Figure 5-32 for the films deposited on ITO with 15 nm nominal thickness. As usual, dendritic and background grains were observed each of them leading to specific electrical signature. It is observed from the current image Figure 5-32(b) that the intensity of current is less than that in negative sample bias, for same bias amplitude. Unlike the case of negative sample bias, the dendritic islands conducts very less compared to background grains, except at some weak points (Figure 5-32(b)). This is probably due to the high injection barrier offered by the grains in dendritic islands at the ITO/6T interface. Higher conduction for negative sample bias is due to high density of SCL current just under the tip; this configuration compared to positive sample bias (where injection is from planar

electrode) makes conduction through the amorphous grains in dendritic islands. In Figure 5-33 height image of a 2 × 2 μm^2 area of a 25 nm 6T film on ITO is provided showing background grains along with the corresponding current image at a sample bias of 2V. A closer look at the background grains shows homogeneous conduction inside individual grains of similar height. However, with the increase of grain height, the current contrast decreases, indicating no local probing in this configuration. Also at the grain boundaries higher current is observed due to two reasons. First, a higher tip sample contact area at the grain boundary edges and, second, grain boundaries of 3D grains having a lower thickness and being closer to ITO than the top part of the grains. Cross-sectional height and current profile along white lines on (a) and (b) of Figure 5-33 shows that the current decreases with grain height.

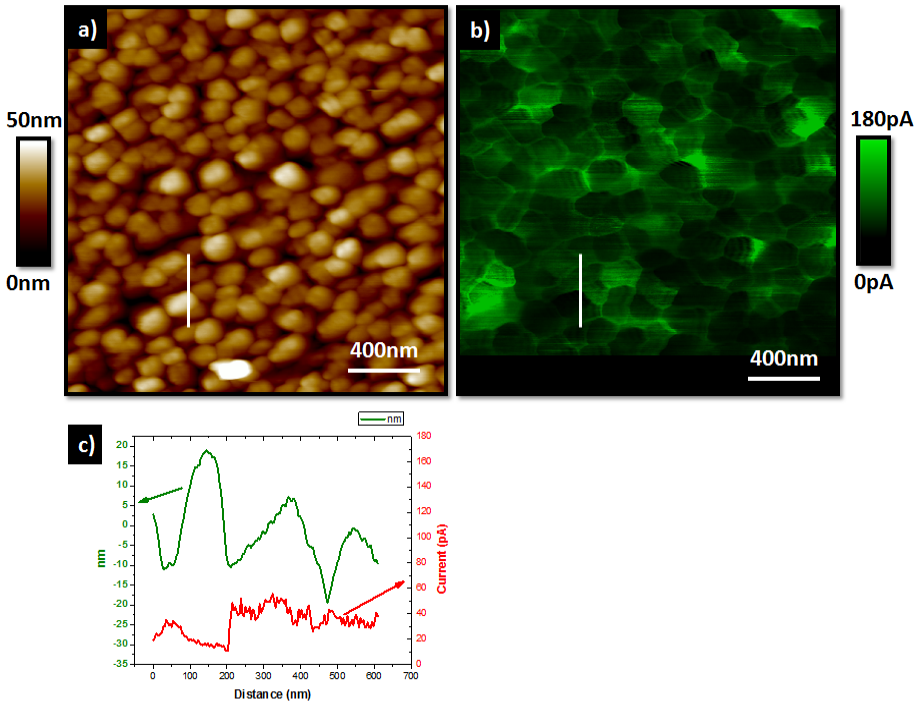

Figure 5-33 (a) Height image of a 2 × 2 μm^2 area of 25 nm 6T thin film on ITO substrate showing background grains. (b) C-AFM current image of (a) at 2V dc sample bias. (c) Cross sectional height and current profile along white lines on (a) and (b) shows that with height the current decreases.

In Figure 5-34 (a), the point and shoot I-V characteristics on films with nominal thickness of 10nm, 15nm, 25nm and 40nm are displayed. Figure 5-34 (b) shows current voltage characteristics

plotted in log-log scale. The current is here seen to decrease with the thickness of the film. Except the sample with extreme low thickness of 10 nm, all other samples display a current with square law dependence (see Figure 5-34) on the applied positive sample bias after a bias of 3 V (i.e. slope 2 in log-log scale), suggesting a dominating trap free space charge limited current, while films of 10 nm presents a slope of 3 in the logarithmic I-V profile, similar to that in the case of negative sample bias, where the mobility of holes are field dependent. Injection limited current was observed, before the emergence of the space charge limited region indicated by a linear behavior.

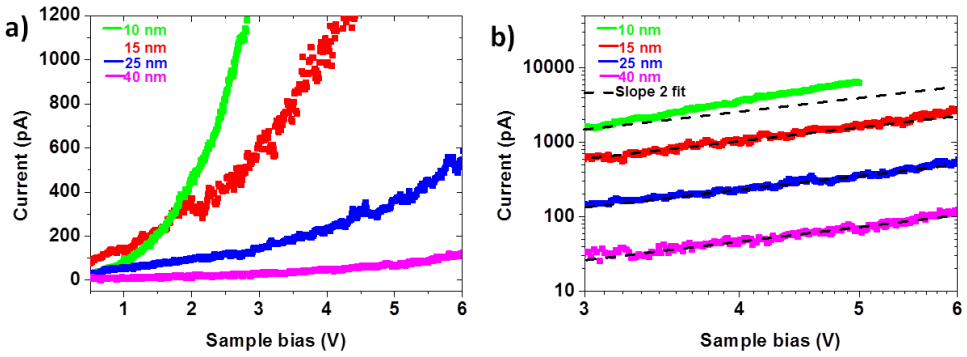

Figure 5-34 (a) C-AFM I-V characteristics of 10 nm, 15 nm, 25 nm and 40 nm film in vertical configuration at positive sample bias. Other than 10 nm film, in all other samples the current varies quadratically with voltage (b) (a) in log-log scale, other than 10 nm nominal thick sample, all others give a slope of 2 in log-log scale. 10 nm film shows a slope of 3.

In C-AFM configuration at negative sample bias, it was observed that the space charge limited current varies with respect to L^{-1}, contrary to L^{-3} variation in planar devices. Similarly, it is very important to monitor the dependence of the film thickness on C-AFM current at positive sample bias. As explained before in the case of negative sample bias, spherical flow of current is considered with voltage proportional to the square root of the thickness ($\sqrt{L}$) (see equation (5.2) and Figure 5 31). Similar graph was plotted to see if V is proportional to $\sqrt{L}$ at normalized current values. However, in the case of I-V profiles in positive sample bias (see Figure 5 34 (a), we did not find any linear dependence of V on square root of thickness, implies that the charge transport is entirely different from that in the case of negative sample bias. In order to check whether there

exists an L^{-3} dependence of current in positive sample bias, just like in the case of planar devices, average current values were taken from all three I-V curves that showed space charge limited regime, for four different voltage values, (3V, 4V, 5V and 6V). A graph is constructed with inverse of the thickness value versus I/V^2, as shown in Figure 5 35. In the inset a log- log plot of this curve is displayed with a slope nearly equal to three. This indicates that in positive dc sample bias in C-AFM configuration, for films with lower thickness as in present study, current has inverse dependence on L^3.This implies in this configuration and bias, the C-AFM current follows the V^2 and L^{-3} dependence of typical Mott Gurney law ($I \alpha V^2/L^3$) for macroscopic contacts. However the presence of asymmetric electrodes (point probe electrode at the charge extracting end) is likely to play a role in the magnitude of the current extracted at a given voltage i.e. tip-plane symmetry of C-AFM set up requires a modification in the typical Mott-Gurney law. As there is asymmetry in the geometry of electrodes there will be a difference in the quantity of charges extracted at the point contact when compared with planar electrode configuration. As a result the mobility extraction by Mott-Gurney law for planar devices is not valid in this configuration.

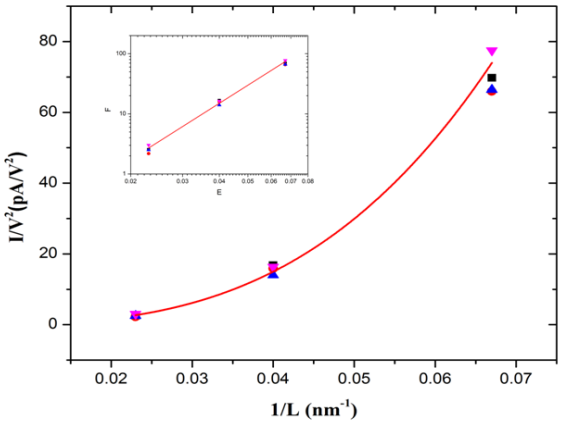

Figure 5-35 L^{-1} vs. I/V^2 profile across the 6T deposit extracted for C-AFM I-V profile in vertical configuration for positive sample bias. Inset shows the log-log scale of the graph with slope nearly equal to 3.

The I-V curve obtained for films of 10 nm thickness and lower shows a different behavior. The current no longer varies quadratically with voltage and in log-log scale it gives a slope of ~ 3 for this thickness. This implies that the nature of transport is limited by thickness of the film. i.e. for positive sample bias, when the thickness of the film L exceeds a critical thickness, say t_o, transport is dominated by space charge limited regime (15nm, 25nm and 40nm nominal thick deposits), while when the thickness of the film is less than the critical limit t_o, owing to the very high electric field acting over very low thickness, either electric field dependent mobility or charge density dependent mobility come in to play, in which current no longer varies with square of the voltage just like in the case of negative sample bias.

5.3 Local probing of electrical properties of P3HT using C-AFM

In this section, the charge transport properties of thin films of a small molecule, i.e. the 6T films discussed in section 5.2 are compared with that of a solution processed polymer, 100% regioregular poly (3-hexylthiophenes) (P3HT). The same substrate (ITO patterned glass) as the one for 6T deposition is used and C-AFM is employed in two different configurations, for negative and positive polarity. The HOMO of P3HT is of the same level as 6T, and $PtIr_5$ coated C-AFM tip is employed as in the case of 6T films. Figure 5-37 (e) presents the phase image of 100% regioregular P3HT thin films on glass. Unlike in the case of 6T thin films, on glass and on ITO P3HT shows a similar morphology, the fibrillar one. Figure 5-36 (a) presents the CAFM current image of the polymer with 100% regioregularity, obtained by ranging the dc sample bias from 0 V to -3 V along the slow scan axis in side configuration for a negative sample bias. Similar to every bias and geometrical C-AFM configuration, monotonic increase of the current with the bias is observed. The current-voltage characteristic constructed from the line-averaging of the current image (see Figure 5-36 (a)) is shown in (b) of same panel. A quadratic variation of the current is observed, attributed to a space charge limited current (SCLC) regime. This represents a contact resistance dominant regime ($\theta < 1$) and, in order to extract the hole mobility, the modified Mott-Gurney equation (equation (3.8)) is employed. The contact radius $r_{0,}$ calculated from equation (3.9) is ~ 2 nm. Z is ~ 30 nm, ε_r = 3.2, a typical value for polymers and the mobility calculated is 1.29×10^{-5} cm^2 /Vs. This mobility value is very close to the reported in the literature [32]. When compared to polycrystalline 6T thin films, the mobility is lower by an order of magnitude of two. This is expected, considering the better π-stacking in vacuum evaporated 6T

thin films. In Figure 5-36 (c) C-AFM in side configuration for positive sample bias is also presented. The I-V profile however shows a quadratic dependence of I on V. This result is contrary to the linear dependence exhibited by 6T thin films on similar configuration and polarity. It has to be noted that in P3HT, for a sample bias of +3 V, the current is just less than 15 pA, while for 6T for same bias current is of the order of 300pA. However, the I-V characteristics of 6T for positive sample bias (see Figure 5-26 (c)) for the same current range as observed on P3HT I-V profiles (i.e. less than 15pA) also showed a deviation from linear behavior. This implies that in the case of 6T thin films, owing to the better self organization of the molecules within the film, the traps will be filled by a very small increase in bias. Once the traps are filled, a transport resistance dominated regime is reached, where current varies linearly with voltage. However, in the case of P3HT, the traps are not filled for the given voltage range and therefore causing the slowdown of the charge transport. Here, charge transport is affected by the presence of traps and hence results in a deviation from linear I-V characteristics.

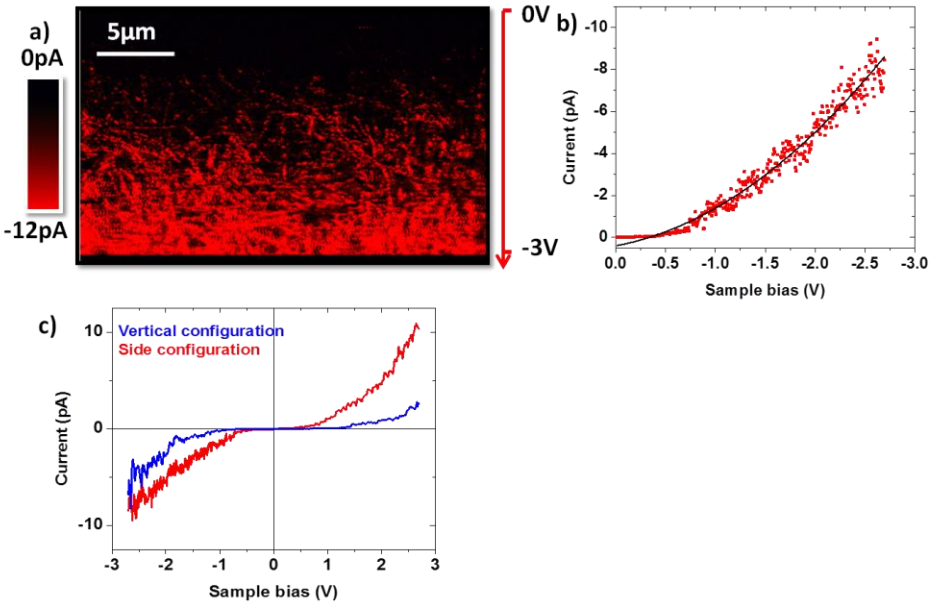

Figure 5-36 (a) C-AFM current image of a 5 × 2.5 µm^2 area of 100% regioregular P3HT thin film on glass substrate obtained by varying the dc sample bias from 0V (top of the image) to -3V(bottom of the image) in side configuration at negative sample bias. (b) Current-voltage characteristic derived from line averaging of the current image with a quadratic fit. (c) Current-voltage characteristic derived from line averaging of the current image of 100% regioregular P3HT in side and vertical scanning configuration on both polarities.

C-AFM I-V profiles of P3HT deposited on ITO (vertical configuration) for negative sample bias is given on Figure 5-36 (c). The I-V profile in log-log scale show an exponent of 3.8, deviating from the square law. However, the current intensity on 6T at vertical configuration for negative sample bias was higher when compared to C-AFM side configuration. But in the case of P3HT, the current intensity at a negative sample bias for side configuration is greater than vertical configuration. This is because on vertical configuration, the holes have to be transported in a direction perpendicular to the π-staking direction of P3HT. Along this direction, the presence of alkyl chains reduces the efficiency of charge hopping from polymer chain to polymer chain. Moreover, the fibrils are formed one over another further increases the presence of extra grain boundary resistances along with the presence of carrier trapping sites in P3HT fibrils, hampers the charge transport in vertical configuration. Here the presence of carrier trapping sites determines the nature of I-V profile. As a result, theI-V characteristics deviate from the expected behavior of space charge limited regime in ideal spherical flow case, in negative sample bias, when compared to 6T. Similarly in the case of positive sample bias on ITO, the slope of the I-V curve was ~3.8. The similarity in slope of logarithmic I-V profiles for two different polarities indicate that the presence of excess of charge trapping sites play a greater role in determining the nature of I-V curves in P3HT at vertical configuration, irrespective of the nature of injecting contact, while in the case of trap free 6T, geometrical configuration played greater role in determining the nature of transport.

5.3.1 Morphological and electrical properties of P3HT with varying regioregularity in side configuration at negative sample bias

Tapping mode AFM studies were employed to study the nanoscale morphology of the P3HT deposits with varying degree of regioregularity. Figure 5-37 presents typical phase images (2×2 μm^2 area) of P3HT deposits with 56%, 83%, 89%, 95% and 100% regioregularity. It is evident from the phase images that, besides the polymer with 56% regioregularity, the dominating feature of all the samples are its nanofibrillar morphology. Such fibrils have been reported often in thin films of P3HT [33, 34]. As explained in (section 3.5.3) the fibrillar morphology is the signature of the crystalline ordering in regioregular P3HT chains, while the absence of any such fibrils reveals the lack of self assembling of polymer chains.

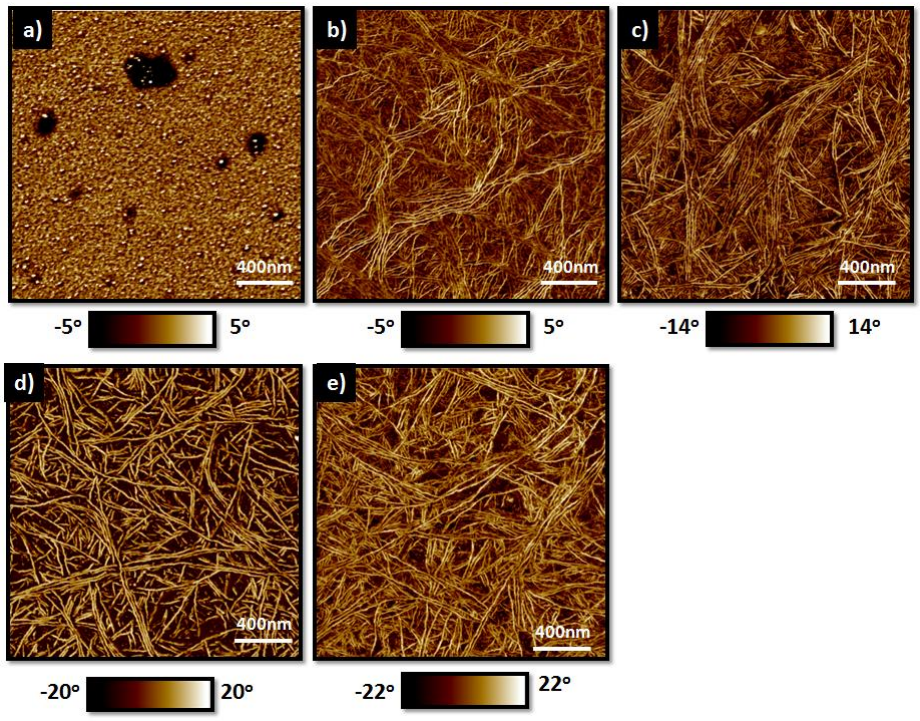

Figure 5-37 2 × 2μm^2 AFM phase images of thin deposits of P3HTs with varying regioregularity (a) 56% (b) 83% (c) 89% (d) 95% and (e) 100% regioregularity respectively.

Close examination of phase contrast AFM images revealed width, length and height of the fibrils. The majority of the fibrils in 100%, 95% and 89% regioregular polymers displays a length over 1μm up to 3μm with similar morphologies. This suggest that despite of the small amount of coupling defects in 95% and 89% regioregular polymers , the polymer chains were able to self assemble in the same way as in 100% regioregular deposit to form long fibrils. However the AFM images on 83% regioregular polymer predominantly showed branched fibrils, less than 1μm long probably owing to the excess presence of coupling defects in it. The length and width of the fibrils for different regioregular P3HT deposits is reported in the Table 5-1.

Table 5-1 Typical dimensions of the fibers for P3HTs with different degree of regioregularity measured using AFM and the hole mobility values extracted from C-AFM current voltage characteristics from Figure 1 3(c).

Degree of regioregularity of P3HT	Width(nm)	Length	Mobility μ ($cm^2V^{-1}s^{-1}$)
100%	14±1.5	>1μm	1.29×10^{-5}
95%	15±1.5	>1μm	1×10^{-5}
89%	14±1	>1μm	2.5×10^{-6}
83%	13±1.5	<1μm	0.74×10^{-6}
56%	No fibrils		

The width of the fibrils doesn't change significantly in the different polymers, within the experimental error range for tapping mode AFM and the width is consistent with the packing structure mentioned as it is roughly equal to the average chain length for a fully extended molecule. The observed constant same width on the fibers for P3HTs with different degree of regioregularity reflects similar molar mass of the polymers used for this study. The height of the fibrils is generally observed to be 13 ± 2 nm, i.e. few stacked lamellae. It has to be noted that the SCLC behavior is observed for all the samples investigated expect the polymer with 56% regioregularity. In this polymer, no current is detected because of its amorphous nature.

The current voltage characteristics of the polymers with varying regioregularity in negative sample bias at side configuration are presented in Figure 5-38. The hole mobility value extracted for all polymer deposits from Figure 5-38 using the modified Mott-Gurney equation (equation (3.8)) is reported in the Table 5-1. The mobility values extracted for polymers with 100% and 95 % regioregularity has values very close to each other, suggesting that the charge transport properties do not get hampered by the presence of a small amount of regio-irregularity [58]. However the mobility value for 89% regioregular polymer drops significantly even though this film displays the same fibrillar structure compared to 100% and 95% regioregular polymer films. This may suggests that even though the morphology is similar, the excess presence of packing defects inside the fibrils due to lower regioregularity hampers the transport through it. While polymer with 83% regioregularity showed a further decrease in mobility value of the order of one

when compared to the first two. This suggest that along with the increased packing defects due to lower regioregularity, the shorter length of fibrillar structures also limits the transport as the holes has to move through interchain hopping which is slower than intra chain transport

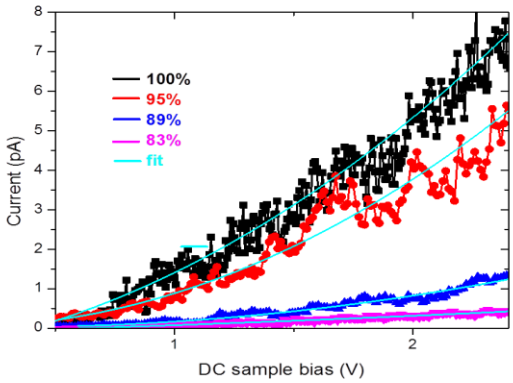

Figure 5-38 Current-voltage curves obtained by line averaging of the current images of P3HT with a degree of regioregularity of 100%, 95%, 89% and 85% respectively in negative sample bias at side scanning configuration.

.

5.4 Conclusions

In this chapter the local transport properties of 6T thin films deposited by OMBE on two different substrates, glass and ITO, have been studied. The nanoscale morphology and charge transport are explored with AFM and C-AFM respectively and compared. Morphological studies with 6T deposits of varying thickness were carried out on the two different substrates by tapping mode AFM. The growth of three dimensional structures of different types, with peculiar grain geometry and molecular orientation, were identified. On glass, well organized terraced grains along with needle like crystallites and dendritic islands with amorphous grains were identified. On ITO, well organized 3-D grains (without terraces) and amorphous grains in dendritic islands were identified, while no needle like crystallites were found. Yet, 6T molecules predominantly orient in a standing mode, i.e. nearly perpendicular with respect to substrate, forming self organized lamellar structures on the smooth glass substrate and granular structures on the relatively rough ITO

substrate. The standing mode self organization is further evidenced by means of XRD, and the molecular structure is similar to that of the low temperature polymorph of 6T crystal. In view of devices, identifying the nature of charge transport through 6T structures with different nanoscale self organization is necessary. The investigation of local charge carrier transport mechanisms have been carried out by conductive-AFM measurements applied in two different scanning configurations (side and vertical) to better discriminate between the planar and transversal transport mechanisms in the thin films. Positive and negative sample bias has also been applied to compare the charge injection from the ITO cathode or from the tip anode, respectively, to better understand the origin of current contrast in C-AFM measurement. The different transport regimes are illustrated in Figure 5-39. In side configuration (red curve), when the charge carriers are injected from the C-AFM tip into the film to reach the ITO back electrode, three transport regimes are evidenced. Here, the distance between the injecting tip contact and the back contact plays a major role in the determination of a specific transport regime. At small distance (few hundreds of microns), the contact resistance at the tip-sample contact dominates the transport regime (where $\theta < 1$). In this regime the transport is space charge limited. The current is probed over a nanoscale volume under the tip, indicates local probing. The distance between the electrodes does not affect the current in contact resistance dominated regime. Local carrier mobility can therefore be extracted using a modified Mott-Gurney law taking into account the size of the contact and the sphere plane geometry of the tip sample contact. The highest local planar mobility extracted for 6T is $(1.2 \pm 0.2) \times 10^{-2}$ cm^2/Vs. Further away from ITO, the transport is dominated by the resistance of the film and a linear dependence of the current with the voltage is observed (where $\theta > 1$). The resistance value extracted from this region is found to be $(4.7 \pm 1) \times 10^9$ Ω. Further away a third transport regime is evidenced. This electrical regime is observed on films that are partially covered on the substrate.

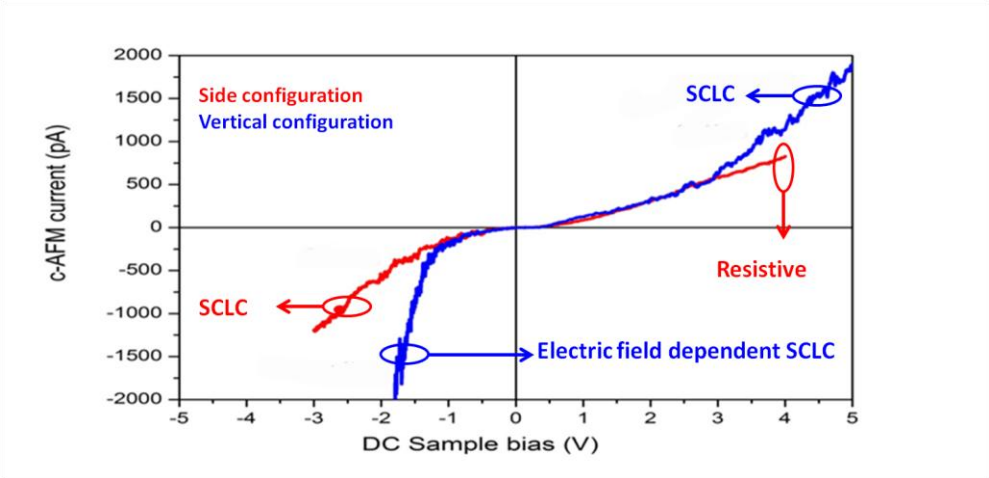

Figure 5-39 Typical C-AFM I-V characteristics observed for two different C-AFM scanning configurations. Blue curve represents the I-V characteristics in vertical configuration which give thickness dependent SCLC regime for positive sample bias and field dependent space charge current in spherical flow system for negative sample bias. Red curve represents the I-V characteristics in side configuration showing SCLC regime for negative sample bias and resistive behavior for positive sample bias.

In third regime the transport is limited by resistance of the grain boundary between the crystalline domains. When the charges are injected from ITO to the tip in side configuration, the transport is observed to be dominated by the resistance of the film irrespective of the tip-ITO distance and a linear dependence of the current with the voltage is found, owing to the large carrier pathways and the resistance of the film extracted in this configuration and bias is of the same order of magnitude as that extracted from negative sample bias in side configuration. In vertical configuration at negative sample bias (blue curve in Figure 5-39), C-AFM measures the current in transversal direction (through the film thickness) and the C-AFM current strongly depends upon the film thickness. That means that C-AFM in this configuration and bias probes the bulk properties of the organic film. Current variations are dominated by the geometry of the point contact between the probe and the sample. The dominant transport mechanism is space charge limited in radial flow case. Here the current is inversely proportional to the thickness of the film. Large field in the thin film induces field dependent mobility leading to divergence from the square dependence of the voltage for current. This effect obviously decreases with the film thickness. The field independent transversal mobility is calculated to be $(1.43 \pm 0.2)\times10^{-3}\,cm^2/Vs$.

For positive sample bias in vertical configuration current variations are dominated by the plane parallel geometry of the ITO back contact. The current is dominated by the space charge limited mechanism. As a result the current is proportional to the inverse cube of film thickness. However the current intensity depends on the spreading effect at the tip-sample contact and hence it is different from that obtained in plane parallel geometry; also compared to negative sample bias, the field is lower in this case. Hence the field dependent mobility occurs for the film with thickness lower than10 nm.

The charge transport mechanisms in different geometrical configurations for different bias on thin films of 6T are compared with that of the regioregular polymer P3HT. On vertical configuration at positive and negative sample bias, the holes in polymer film exhibited field dependent mobility owing to the low thickness, similar to that exhibited by 6T.In fact, on side configuration, at negative sample bias the transport is space charge limited. The local hole mobility extracted from this regime is found to be1.29×10^{-5} cm^2/Vs.

Morphological and electrical properties of thin deposits of polymer P3HT decreasing the degree of regioregularity were studied using AFM and C-AFM respectively. Fibrillar morphology with long range self assembly of molecules were formed on polymer deposits with 83% or more regioregularity. The results indicate that a fairly high amount of region irregularity cannot prevent the long range self-assembly of the molecules under thermodynamic conditions. Charge transport properties were studied with C-AFM and the hole mobility for polymers with different regioregularity were extracted. Charge transport properties enhanced with increasing regioregularity in general, however it was found that the presence of a small amount of region irregularity (~5%) under thermodynamic conditions do not influence the charge transport properties of the polymer in a significant manner.

5.5 References

1. Kalihari, V., et al., *Grain Orientation Mapping of Polycrystalline Organic Semiconductor Films by Transverse Shear Microscopy*. Advanced Materials, 2008. **20**(21): p. 4033-4039.
2. Kurdesau, F., et al., *Comparative study of ITO layers deposited by DC and RF magnetron sputtering at room temperature.* Journal of Non-Crystalline Solids, 2006. **352**(9–20): p. 1466-1470.
3. Horowitz, G., et al., *Growth and Characterization of Sexithiophene Single Crystals.* Chemistry of Materials, 1995. **7**(7): p. 1337-1341.
4. Servet, B., et al., *X-ray determination of the crystal structure and orientation of vacuum evaporated sexithiophene films.* Advanced Materials, 1993. **5**(6): p. 461-464.
5. Garnier, F., et al., *Molecular engineering of organic semiconductors: design of self-assembly properties in conjugated thiophene oligomers.* Journal of the American Chemical Society, 1993. **115**(19): p. 8716-8721.
6. Zhang, F., et al., *Studies on morphology and molecular arrangement of pentacene on different substrates.* Superlattices and Microstructures, 2009. **45**(6): p. 612-617.
7. Loi, M.A., et al., *Supramolecular organization in ultra-thin films of α-sexithiophene on silicon dioxide*. Nature Materials, 2004. **4**(1): p. 81-85.
8. Aruta, C., et al., *Improved structural ordering in sexithiophene thick films grown on single crystal oxide substrates.* Applied Physics A, 2009. **97**(2): p. 387-394.
9. Servet, B., et al., *Polymorphism and Charge Transport in Vacuum-Evaporated Sexithiophene Films.* Chemistry of Materials, 1994. **6**(10): p. 1809-1815.
10. Ivanco, J., et al., *Sexithiophene films on clean and oxidized Si(111) surfaces: Growth and electronic structure.* Journal of Applied Physics, 2004. **96**(5): p. 2716.
11. Ikeda, S., et al., *Epitaxial growth and domain coalescence of sexithiophene induced by the steps on cleaved KBr*. Journal of Crystal Growth, 2004. **265**(1–2): p. 296-301.
12. Campione, M., et al., *Homoepitaxial Growth of α-Hexathiophene.* The Journal of Physical Chemistry C, 2007. **111**(34): p. 12741-12746.
13. Bartelt, M.C. and J.W. Evans, *Dendritic islands in metal-on-metal epitaxy I. Shape transitions and diffusion at island edges.* Surface Science, 1994. **314**(1): p. L829-L834.

14. Albonetti, C., et al., *Height measurements on soft samples: applied force, molecules deformation and phase shift*, in *EMC 2008 14th European Microscopy Congress 1–5 September 2008, Aachen, Germany*, M. Luysberg, K. Tillmann, and T. Weirich, Editors. 2008, Springer Berlin Heidelberg. p. 719-720.
15. Straub, A., *Advanced SPM studies on the growth of ultrathin films of organic semiconductors at metal and dielectric interfaces*, 2011, University of Bologna. p. 116.
16. Zhou, S., et al., *Rectifying behaviors of Langmuir–Blodgett films of an asymmetrically substituted phthalocyanine.* Chemical Physics Letters, 1998. **297**(1–2): p. 77-82.
17. Hahm, S.-W., *Buckling-based measurements of mechanical moduli of thin films.* Electronic Materials Letters, 2009. **5**(4): p. 13.
18. Fichou, D., *Frontmatter*, in *Handbook of Oligo- and Polythiophenes*. 2007, Wiley-VCH Verlag GmbH. p. i-xxiv.
19. Dinelli, F., et al., *Spatially Correlated Charge Transport in Organic Thin Film Transistors.* Physical Review Letters, 2004. **92**(11): p. 116802.
20. Dinelli, F., et al., *Effects of Surface Chemical Composition on the Early Growth Stages of α-Sexithienyl Films on Silicon Oxide Substrates.* The Journal of Physical Chemistry B, 2005. **110**(1): p. 258-263.
21. Loiacono, M.J., E.L. Granstrom, and C.D. Frisbie, *Investigation of Charge Transport in Thin, Doped Sexithiophene Crystals by Conducting Probe Atomic Force Microscopy.* The Journal of Physical Chemistry B, 1998. **102**(10): p. 1679-1688.
22. Hunter, S. and T.D. Anthopoulos, *Observation of Unusual, Highly Conductive Grain Boundaries in High-Mobility Phase Separated Organic Semiconducting Blend Films Probed by Lateral-Transport Conductive-AFM.* Advanced Materials, 2013. **25**(31): p. 4320-4326.
23. Mark, P. and W. Helfrich, *Space-Charge-Limited Currents in Organic Crystals.* Journal of Applied Physics, 1962. **33**(1): p. 205-215.
24. Vissenberg, M.C.J.M. and M. Matters, *Theory of the field-effect mobility in amorphous organic transistors.* Physical Review B, 1998. **57**(20): p. 12964-12967.
25. Mandoc, M.M., et al., *Trap-limited electron transport in disordered semiconducting polymers.* Physical Review B, 2007. **75**(19): p. 193202.

26. Pasveer, W.F., et al., *Unified Description of Charge-Carrier Mobilities in Disordered Semiconducting Polymers.* Physical Review Letters, 2005. **94**(20): p. 206601.
27. Ionescu-Zanetti, C., et al., *Semiconductive Polymer Blends: Correlating Structure with Transport Properties at the Nanoscale.* Advanced Materials, 2004. **16**(5): p. 385-389.
28. Murgatroyd P, N., *Theory of space-charge-limited current enhanced by Frenkel effect* Journal of Physics D: Applied Physics, 1970. **3**(2): p. 6.
29. Kemerink, M., et al., *Three-Dimensional Inhomogeneities in PEDOT:PSS Films.* The Journal of Physical Chemistry B, 2004. **108**(49): p. 18820-18825.
30. Weber, S.A.L. and R. Berger, *Electrical tip-sample contact in scanning conductive torsion mode.* Applied Physics Letters, 2013. **102**(16): p. 163105.
31. Murray A. Lampert , P.M., *Current Injection in Solids (Electrical Science)*. 1970, New York: Academic Press. 354pp.
32. Willot, P., et al., *Poly(3-alkylthiophene) with tuneable regioregularity: synthesis and self-assembling properties.* Polymer Chemistry, 2013. **4**(9): p. 2662-2671.
33. Surin, M., et al., *Relationship between the microscopic morphology and the charge transport properties in poly(3-hexylthiophene) field-effect transistors.* Journal of Applied Physics, 2006. **100**(3):.
34. Derue, G., et al., *Nanorubbing of Polythiophene Surfaces.* Journal of the American Chemical Society, 2005. **127**(22): p. 8018-8019.
35. Surin, M., et al., *Regioregular poly(3-hexylthiophene)-poly(ε-caprolactone) block copolymers: Controlled synthesis, microscopic morphology, and charge transport properties.* Organic Electronics, 2010. **11**(5): p. 767-774.

Chapter 6

6 Conclusions and Perspectives

This work was devoted primarily to the study of thin films of small molecules such as 4T and 6T that can be used as active materials for device applications. In the first part of the thesis the relevance of organic epitaxy in growing high quality crystalline thin films was explained. Crystalline thin films of 4T were grown by OMBE and the optical, structural and morphological properties were studied. 4T thin films have been grown over of two different organic substrates, namely PET and KAP single crystals, where KAP substrate is used as a reference. In both cases highly ordered films, with the molecules packed in 4T monoclinic crystalline phase was obtained. The lattice registry between the substrate and the overlying 4T epitaxial thin film is satisfied by virtue of line-on-line epitaxy. However the selection of crystal structure in these epitaxial thin films of 4T was found to be driven by the substrate. 4T thin films on KAP (010) have shown the presence of the low temperature crystal phase of 4T, similar to that reported in the literature. The epitaxial relations between the lattice of the substrate and the overlayer were deduced, thanks to morphological, optical and structural characterizations. 4T thin films had a unique in-plane orientation on KAP, as determined by the epitaxial relationship: 4T [110] // KAP [101]. It is demonstrated that epitaxial 4T films can be grown also on single crystal PET, where a pseudomorphic phase very close to the high temperature crystal phase grows as the dominant film phase. The possible epitaxial relations between the lattice of substrate and overlayer are deduced, where 4T/HT[010] // PET[110]. This is the first time that a polymorph close to the high temperature phase of 4T is found in thin films grown at room temperature. The 4T/HT, due to its better conductivity, is considered as the most promising polymorph of 4T for applications in organic devices. The similarity in the microscopic properties of the pseudomorphic phase and the HT phase indicates that the newly formed pseudomorphic phase can also be exploited for making high quality organic devices like OFETs, which require molecules in a standing orientation. In

addition, the epitaxial relations between the PET lattice and thin needle like crystallites, which are made of the low temperature crystalline phase of 4T, were also deduced. Besides, the solubility of both substrates, KAP and PET enables the use of cost-effective wet-transfer methods, a useful method that can be employed for device processing. These results indicate that the mechanisms of organic epitaxy can be exploited in driving the orientation of the overlayer in its thermodynamically stable phase as well as in inducing the growth of new and different oriented phases with useful physical properties.

On a purely crystallographic standpoint, we consider noteworthy that, notwithstanding the high symmetry of the PET crystal, its basal surface presents local structural features having a strong impact on the molecular arrangement and the anisotropy of the overlayer. These features derive primarily from the segregation of alkyl groups and O-H groups of the PET molecules giving rise to a lamellar structure and a uniaxial alignment of protruding H-atoms. The choice of crystalline substrates for organic epitaxy can take advantage of these findings.

In the second part of the thesis, we have explored the nanoscale morphology and charge transport mechanisms in organic semiconductor films by utilizing AFM and C-AFM, respectively. At first, we studied the morphology of 6T thin films grown on two different substrates (glass and ITO) by performing tapping-mode AFM analyses on thin films of increasing thickness. On both substrates the molecules predominantly self organize in a standing mode with the low temperature crystal phase evidenced by XRD. We observed three types of morphology on 6T films on glass: predominantly well organized grains with monolayer terraces, non-terraced grains in dendritic shaped islands, and needle like crystallites. On ITO two kinds of morphologies were found: 3-D island-like structures and grains in dendritic islands while needle like crystallites are not present on 6T thin film on ITO.

Highly resolved technique like C-AFM was employed to study the local electrical properties at nanoscale. C- AFM was applied in two different scanning configurations (side and vertical) to better discriminate between the planar and transversal transport mechanisms in the thin films. Positive and negative sample bias has also been applied to compare the charge injection from the ITO cathode or from the tip anode, respectively to further understand the origin of current contrast in C-AFM measurement.

In side configuration, we evidenced three different current transport regimes at negative sample bias. Depending on the distance between the injecting anode tip and the back cathode ITO, a contact resistance dominated regime, transport dominated regime and a grain boundary resistance dominated regime were diversely observed. In contact resistance dominated regime (when $\theta < 1$) the current is probed locally and the current mechanism is space charge limited. In this regime, current does not vary with the distance between the electrodes. Local carrier mobility was extracted from the current voltage characteristics in this regime, using a modified Mott-Gurney law taking into account the size of the contact and the sphere plane geometry of the tip sample contact. The highest local planar mobility extracted for 6T is $(1.2 \pm 0.2) \times 10^{-2}$ cm^2/ V.s which was close to the reported FET mobility of the material. Resistance of the film extracted from the transport resistance dominated regime (when $\theta > 1$) is $(4.7 \pm 1) \times 10^9$ Ω. The grain boundary resistance regime is usually observed in those films that are partially covered on the substrate, where the transport is limited by the resistance of the grain boundary between the crystalline domains. In positive sample bias at side configuration, a transport dominated regime was evidenced and the resistance extracted from this regime was of the same order of magnitude as that evidenced for holes injected from the tip.

In vertical configuration at negative sample bias, C-AFM measures the current in transversal direction across the film. C-AFM in this configuration and bias, probes the bulk properties related to the organic film unlike local properties in the case of side configuration in same bias. The dominant current transport mechanism is space charge limited in radial flow case and the measured current is inversely proportional to the thickness of the film. In this configuration, large field in the thin film induces field dependent mobility leading to divergence from the square dependence of the voltage with current and hence the intensity of current measured in this case is very high when compared to all other configurations. The field independent transversal mobility is extracted by adapting the equation for space charge limited current in spherical and radial flow case. The transversal field independent mobility of 6T is calculated to be $(1.43 \pm 0.2) \times 10^{-3}$ cm^2 /Vs. In vertical configuration for a positive sample bias, the dominant current transport mechanism is identified to be space charge limited as current variations are dominated by the plane parallel geometry of the ITO back contact. The intensity of current is inversely proportional to the cube of the thickness of the film, which implies in this configuration bulk properties of the film are investigated. This clearly demonstrates that depending upon the configuration and bias

polarity, plenty of dominating effects play a role in determining the nature of charge transport. The C-AFM current contrast observed is therefore strongly dependent on the configurations and bias polarity applied. This also indicates the remarkable versatility and potentiality of C-AFM.

Finally, the results on 6T in different C-AFM configurations are compared with a polymer, regioregular P3HT. The local hole mobility extracted using modified Mott-Gurney law for regioregular P3HT in side C-AFM configuration, at negative sample bias is found to be 1.29×10^{-5} $cm^2/V.s$. Finally, different P3HT polymer deposits with varying degree of regioregularity are locally investigated in C-AFM side configuration at negative sample bias and the local hole mobility is extracted and compared.

In conclusion, the overall research work discussed in this thesis opens some interesting and promising perspectives concerning the use in organic semiconductors in device applications. The possibility to use 4T crystalline thin films or other organic molecular thin films for the fabrication of devices like organic field-effect transistors, bi-layer or cascade solar cells by exploiting the possibility to induce specific in-plane orientations of the film is demonstrated by selecting the suitable substrate, to exploit organic molecular beam epitaxy. As there are many open questions still remaining with the operations of C-AFM like finding the mobility in vertical configuration in positive sample bias, more work has to be done to formulate equations describing that particular configuration. Since C-AFM in a particular configuration measures the local electrical characteristics, this can be exploited to tailor the performances of various devices like OFETs, OPVs and OLEDs. As far as C-AFM future work is concerned, extending the local electrical characterization to various other promising organic semiconductors, bulk hetero-junctions of polymers and small molecules and polymer nano-particle matrix are of great interest in the context of devices. As a future work, it would be also interesting to study about the oxidation mechanisms of organic thin films using C-AFM. It would be also interesting to use an extension of C-AFM called photoconductive C-AFM, to monitor the photocurrent in bulk hetero-junction blends at nanoscale to explore the photovoltaic properties of the material and yield local external quantum efficiencies. Through this research work and the future activities, we hope to develop enhanced understanding of nanoscale interactions and processes which can be functional in a wide range of applications.

PhD activity

Publications

1) Sreejith Embekkat Kaviyil, Marcello Campione, Adele Sassella, Genbo Su, Youping He, Chenjia Chen, and Alessandro Borghesi, *Growth of pseudomorphic structures through organic epitaxy*, THE JOURNAL OF CHEMICAL PHYSICS **137**, 224703 (2012)

Presentations at congresses

1) **Oral Presentation**: *Electrical properties of sexithiophene thin films with conductive atomic force microscopy* at Forum des Microscopies à Sonde Locale, 25-29 march 2013, **Spa, Belgium.**
2) **Poster:** *Local current mapping on polycrystalline sexithiophene thin films by conductive atomic force microscopy* at Italian Crystal Growth conference 2013, November 14-15, **IMEM-CNR Parma, Italy.**
3) **Poster:** *Organic Epitaxy: the role of substrate in driving film structure* at N&N 12 conference**,** 30/6-7/7/2012 **Thessaloniki, Greece.**